EFFICIENT LARGE-SCALE REAL-SPACE ELECTRONIC STRUCTURE CALCULATIONS

A Thesis
Presented to
The Academic Faculty

by

Swarnava Ghosh

In Partial Fulfillment
of the Requirements for the Degree
Doctor of Philosophy in the
School of Civil and Environmental Engineering

Georgia Institute of Technology
August 2016

EFFICIENT LARGE-SCALE REAL-SPACE ELECTRONIC STRUCTURE CALCULATIONS

Approved by:

Dr. Phanish Suryanarayana, Advisor
School of Civil and Environmental Engineering
Georgia Institute of Technology

Dr. Glaucio H. Paulino
School of Civil and Environmental Engineering
Georgia Institute of Technology

Dr. Arash Yavari
School of Civil and Environmental Engineering
Georgia Institute of Technology

Dr. Ting Zhu
Woodruff School of Mechanical Engineering
Georgia Institute of Technology

Dr. John E. pask
Physics Division
Lawrence Livermore National Laboratory

Date Approved: 7 July 2016

Dedicated in the memory of

Jethudadu and Dadubhai.

ACKNOWLEDGEMENTS

First and foremost, I would like to express my deepest sincere gratitude to my advisor, Professor Phanish Suryanarayana. His support, encouragement and deep insights into the subject has been tremendously valuable for me. I am deeply in debt to him for the time and effort he has dedicated to mentoring my research and helped me develop advanced technical skills. I am also grateful to Professor Glaucio H. Paulino, Professor Arash Yavari and Professor Ting Zhu for serving on my committee and providing feedback on this thesis. I acknowledge the encouragement and support of Dr. John E. Pask. His comments on my research have been invaluable.

I gratefully acknowledge the financial support from National Science Foundation, Department of Energy, Office of Naval Research and the start-up funds provided by Georgia Institute of Technology over the course of my graduate studies.

I have been fortunate enough to be in an excellent company of friends. I would like to thank Pradeep, Sarvani, Qimen(Jim), Prasanth, Bala, Lakshmi, Sangeeta, Ajinkya, Oguzhan, Souhayl, Ashkan, Mostafa, Arkadeep, Anish, Dhwanil, Sourav, Monodeep, Suvadeep, Debasish, Arindam, Abhishek, Samantak, Abhinav, Anshuda, Ayanda and Piudi.

I will always be grateful to my family and friends in India. I would like to take this opportunity and thank my grandparents, pishidida, my maternal and paternal uncles, aunts and my cousins. I am extremely thankful to my parents for their trust in me and being very supportive and encouraging towards my pursuits. This would not have been possible without them. I have been greatly influenced by Jethudadu (Late Prof. Sudhansu Das) and Dadubhai (Late Himansu Das). I express my sincere gratitude to them. I would also like to thank Sreya for being very supportive and understanding.

TABLE OF CONTENTS

LIST OF TABLES

LIST OF FIGURES

SUMMARY

Calculations involving the electronic structure of matter provides valuable insight in understanding and predicting a wide range of materials properties. Over the course of the last few decades, Density Functional Theory (DFT) has been a reliable and popular ab-initio method. The plane-wave basis is commonly employed for solving the DFT problem. However, the need for periodicity limits the effectiveness of the plane-wave basis in studying localized or partially periodic systems. Furthermore, efficient utilization of modern large-scale computer architectures is particularly challenging due to the non-locality of the basis. Real-space methods for solving the DFT problem provide an attractive alternative.

In this work we present an accurate and efficient real-space formulation and parallel implementation of Density Functional Theory (DFT) for performing ab-initio simulations of isolated clusters (molecules and nanostructures), periodic (infinite crystals) and partially periodic systems (slabs and nanowires). Using the finite-difference representation, local reformulation of the electrostatics, the Chebyshev polynomial filtered self-consistent field iteration, and a reformulation of the non-local component of the force, we develop SPARC (Simulation Package for Ab-initio Real-space Calculations), a framework that enables the efficient evaluation of energies and atomic forces to within chemical accuracies in DFT. Through selected examples consisting of a variety of elements, we demonstrate that the developed framework obtains exponential convergence in energy and forces with domain size; systematic convergence in the energy and forces with mesh-size to reference plane-wave result at comparably high rates; forces that are consistent with the energy, both free from any noticeable 'egg-box' effect; and accurate ground-state properties including equilibrium geometries and vibrational spectra. We also demonstrate the weak and strong scaling behavior of SPARC and compare with well-established and optimized plane-wave and other

real-space implementations of DFT for systems consisting up to thousands of electrons. Overall, the developed framework is able to accurately and efficiently simulate the electronic structure of a wide range of material systems and represents an attractive alternative to existing codes for practical DFT simulations.

CHAPTER I

INTRODUCTION

Electronic structure calculations play an important part in modeling complex phenomena that are deemed too complicated to be accurately described by classical theories. Such problems typically arise when the underlying phenomena involves formation and/or breaking of chemical bonds, or when the desired property explicitly depends on the electronic ground state of the system. The key challenge for electronic structure theory is to be able to provide universal methods that accurately describe real systems in nature [70]. These theories and methods should make possible the analysis of general problems and accurately describe the fundamental underlying mechanisms that describe a system.

The past few decades has seen a tremendous rise in the popularity of Density Functional Theory (DFT), an electronic structure theory developed by Hohenberg, Kohn, and Sham [52, 62]. This has been extensively used for understanding and predicting a wide range of materials properties [57, 112, 63, 56]. This popularity of DFT is primarily due to the fact that it is free from any empirical parameters by virtue of its origins in the first principles of quantum mechanics and has high accuracy to cost ratio when compared to other such ab-initio theories [81, 58]. However, the efficient solution of the DFT problem still remains a formidable task. In particular, the orthogonality constraint on the Kohn-Sham orbitals in combination with the substantial number of basis functions required per atom results in a cubic scaling with respect to the number of atoms [108, 22] that is accompanied by a large prefactor. Furthermore, the need for orthogonality gives rise to substantial amount of global communication in parallel computations, which hinders parallel scalability. Consequently, the size of physical systems accessible to DFT has been severely restricted, particularly in the context of ab initio molecular dynamics [72, 65], wherein one complete simulation

regularly requires the solution of the Kohn-Sham equations tens to hundreds of thousands of times.

A large majority of the DFT codes commonly used today utilize the plane-wave basis for discretizing the Kohn-Sham equations [64, 93, 43, 39, 71, 55, 46]. This forms a complete and orthonormal set that is independent of the atomic positions, provides spectral convergence with respect to basis size, and enables the efficient evaluation of convolutions through the Fast Fourier Transform (FFT) [27, 67] and hence an attractive choice. Additionally, effective preconditioners are readily available due to the diagonal representation of the Laplacian operator in this setting [85, 54]. However, there are a few notable disadvantages of the plane-wave basis. Firstly, the need for periodic boundary conditions limits its effectiveness in the study of non-periodic and localized systems such as clusters and defects, requiring the introduction of artificial supercell periodicity [34, 92, 99] [1]. Furthermore, the non-locality of plane-waves make them unsuitable for the development of approaches that scale linearly with respect to the number of atoms [41, 16], and makes parallelization over modern large-scale, distributed-memory computer architectures particularly challenging [14, 105]. These characteristics of plane-wave methods are also inherited by the recently developed spectral scheme for isolated clusters [7], which is the analogue of plane-waves in the spherical setting.

Due to the aforementined limitations of the plane-wave basis, a number of recents efforts have been directed towards the development of real-space DFT implementations. These include discretizations based on finite-differences [25, 23, 18, 31, 95], finite-elements [82, 107, 104, 100, 78, 29, 20, 10], wavelets [4, 26, 35, 30], periodic sinc functions [96], basis splines (B-splines) [15], non-uniform rational B-splines (NURBS) [73], and mesh-free maximum entropy basis functions [98]. However, despite the success of real-space methods in overcoming many of the aforementioned limitations—particularly in the development of

[1] Plane-wave implementations of Density Functional Theory for studying isolated charged clusters using a formulation by Hockney [51] was developed for predicting C_{20}^{+} isomerizations[21].

techniques that scale linearly with respect to the number of atoms [96, 15, 61]—plane-wave approaches still remain the preferred choice for practical DFT computations. This is mainly because real-space implementations are unable to consistently outperform the well-optimized plane-wave codes on the modest computational resources commonly available to researchers, while simultaneously achieving the chemical accuracy desired in DFT calculations (Appendix D). Furthermore, the functionality provided by plane-wave codes is significantly larger than their real-space counterparts, having been under development for a longer period of time.

In this work, we present an accurate and efficient finite-difference formulation and parallel implementation of DFT for isolated clusters, periodic and partially periodic systems. We name the developed framework SPARC (Simulation Package for Ab-initio Real-space Calculations)[37, 38]. The main motivation of this work is to be able to simulate the several classes of interesting systems with different types of boundary conditions from an ab-initio perspective. The approach employed includes a local reformulation of the electrostatics, the Chebyshev polynomial filtered self-consistent field iteration, and a reformulation of the non-local component of the atomic force, which allows for the efficient evaluation of accurate energies and atomic forces within the finite-difference representation. The incorporation of local reformulation of electrostatics differentiates SPARC from existing real-space packages[109, 23]. Through a wide variety of examples, we demonstrate that SPARC obtains exponential convergence in energies and forces with domain size; high rates of convergence in the energy and forces to reference plane-wave results on refining the discretization; forces that are consistent with the energy, both being free from any noticeable 'egg-box' effect; and accurate ground-state properties (e.g. equilibrium geometries and vibrational spectra). Moreover, SPARC displays similar weak and strong scaling as well-established and optimized plane-wave codes, but with a significantly smaller prefactor.

1.1 Organization

The organization of this thesis is as follows:

In chapter 1, we give the motivation of this work and a brief overview of electronic structure theories. We briefly discuss the Schrödinger equation, Hartree Fock and post Hartree Fock theories and the key ideas of Density Functional Theory.

In chapter 2, we discuss an efficient real space formulation of Density Functional Theory for Isolated Clusters. We first present the mathematical background of density functional theory for isolated clusters followed by detailed discussion on a higher order finite difference formulation and parallel implementation of DFT. Next we verify the accuracy and efficiency of this formulation using selected examples and compare with existing plane-wave approaches.

In chapter 3, we discuss an efficient real space formulation of Density Functional Theory for periodic systems. We first present the mathematical background of density functional theory in a periodic setting followed by detailed discussion on higher order finite difference formulation using nonuniform mesh and parallel implementation of DFT. Next we verify the accuracy of this formulation using selected examples and compare with existing plane-wave approaches.

In chapter 4, we extend the formulations for isolated clusters and periodic systems to partially periodic system. We present a discussion regarding the implementation and verify the accuracy and efficiency of this formulation using a slab and a wire as examples.

in Chapter 5, we finally conclude and discuss a few future directions of research.

1.2 A brief overview of Ab-initio theories

The Schrödinger equation is fundamental in describing the quantum mechanical behavior of matter. For a system of N atoms and N_e electrons, under Born-Oppenheimer approximation [32], the time independent version is an eigenvalue problem given by

$$\begin{aligned} H\Psi &= E\Psi\,, \\ H &= -\frac{1}{2}\sum_{n=1}^{N_e}\nabla_n^2 + \frac{1}{2}\sum_{n=1}^{N_e}\sum_{\substack{i=1\\ i\neq n}}^{N_e}\frac{1}{|\mathbf{r}_n-\mathbf{r}_i|} + \sum_{n=1}^{N_e}\sum_{I=1}^{N}\frac{-Z_I}{|\mathbf{r}_n-\mathbf{R}_I|}\,, \\ \Psi &= \Psi(\mathbf{x}_1,\mathbf{x}_2,\ldots,\mathbf{x}_{Ne})\,, \end{aligned} \tag{1}$$

where H is the Hamiltonian of the system and the first term is due to the kinetic energy of electrons, the second term is due to the electrostatic interactions among the electrons and the third is due to the interactions among the electrons and the nuclei. The wavefunction Ψ is an eigenfunction of H corresponding to the eigenvalue E. Here we denote $\mathbf{x}_i = (\mathbf{r}_i, s_i)$, $\mathbf{r}_i \in \mathbb{R}^3$ are the spatial coordinates and s_i is the spin of the i^{th} electron of the system. The atomic positions are denoted by $\mathbf{R}_I \in \mathbb{R}^3$ and the corresponding nuclear charges are Z_I.

From Eqn. 1, we observe that the wavefunctions belong to a $3N_e$ dimensional space. This results in a tremendously complex problem that makes it's solution intractable for systems of more than a few atoms. Therefore one of the major focus of research has been to develop approximate methods for calculating the quantum mechanical state of a system. The most popular ab-initio methods include the Hartree-Fock, post Hartree-Fock methods and Density Functional Theory (DFT).

The Hartree-Fock theory (HFT) approximately solves the electronic Schrödinger equation by expressing the wavefunction as a single Slater determinant. This is mathematically equivalent to assuming that each electron interacts only with an average charge cloud of the other electrons. The Hartree-Fock method does not take into account the correlated motion of electrons and hence introduces an error in the total energy of the system, which is about the order of 1 eV per electron pair in a bond or lone pair [102]. Post Hartree-Fock methods systematically improve upon Hartree-Fock theory by expanding the wavefunction

using a linear combination of more than one Slater determinant or by adding perturbative corrections. However, these improvements come at huge additional costs which limit their solution to tens of atoms.

The seminal work of Hohenberg and Kohn provides a pathway for efficiently modeling the electronic structure of matter. The line of thought involving density functional theory is different from the Hartree-Fock and post Hartree-Fock methods. The first Hohenberg-Kohn theorem essentially proves that the ground state properties of a many electron system depend only on the ground state electronic density. The second Hohenberg-Kohn theorem states that the correct ground state density for a system is the one that minimizes the total energy of the system. This is essentially a reformulation of the problem of solving the Schrödinger equation for one $3N_e$ dimensional wavefunction to the problem of solving for the ground state electron density, ρ in three dimensional space. Thus Density Functional Theory reduces the dimensionality of the problem, thereby greatly decreasing the computational effort. DFT improves upon HFT by including an approximate treatment of the correlated motions of the electrons. This is computationally much less expensive than Hartree-Fock and post Hartree-Fock methods.

In DFT, the electronic kinetic energy is a functional of the electron density. However the explicit functional describing the kinetic energy of electrons is unknown. Orbital-Free Density Functional Theory (OF-DFT) represents a simplified version of DFT, wherein the electronic kinetic energy is modeled using a functional of the electron density, designed so as to match the linear-response of a homogeneous electron gas. This provides an accurate description of elements whose electronic structure resembles a free electron gas, e.g. Aluminum and Magnesium. However extending OF-DFT for covalently bonded materials and molecular systems still remain a formidable task. Kohn-Sham Density Functional Theory (refered to as DFT henceforth) on the otherhand expresses the electronic kinetic energy in terms of individual orbitals corresponding to each electron. This provides a more accurate description of material properties and finds a wider applicability in ab-initio modeling. In

this work we focus on Kohn-Sham Density Functional Theory.

CHAPTER II

ISOLATED CLUSTERS

2.1 Mathematical background

Consider an isolated system of N atoms comprising of nuclei with valence charges $\{Z_1, Z_2, \ldots, Z_N\}$ and a total of N_e valence electrons. Neglecting spin, the system's free energy in Density Functional Theory (DFT) [52, 62, 75] is of the form

$$\mathcal{F}(\Psi, \mathbf{g}, \mathbf{R}) = T_s(\Psi, \mathbf{g}) + E_{xc}(\rho) + K(\Psi, \mathbf{g}, \mathbf{R}) + E_{el}(\rho, \mathbf{R}) - TS(\mathbf{g})\,, \tag{2}$$

where $\Psi = \{\psi_1, \psi_2, \ldots, \psi_{N_s}\}$ is the collection of orbitals with occupations $\mathbf{g} = \{g_1, g_2, \ldots, g_{N_s}\}$, $\mathbf{R} = \{\mathbf{R}_1, \mathbf{R}_2, \ldots, \mathbf{R}_N\}$ is the position of the nuclei, ρ is the electron density, and T is the electronic temperature. The electron density itself depends on the orbitals and their occupations through the relation

$$\rho(\mathbf{x}) = 2\sum_{n=1}^{N_s} g_n \psi_n^2(\mathbf{x})\,. \tag{3}$$

The first term in Eqn. 2 denotes the kinetic energy of the non-interacting electrons, the second term corresponds to the exchange-correlation energy, the third term signifies the non-local pseudopotential energy, the fourth term represents the electrostatic energy, and the final term accounts for the contribution of the electronic entropy to the free energy.

Electronic kinetic energy In Kohn-Sham DFT, the electronic kinetic energy can be written in terms of the orbitals and their occupations as

$$T_s(\Psi, \mathbf{g}) = -\sum_{n=1}^{N_s} g_n \int_{\mathbb{R}^3} \psi_n(\mathbf{x}) \nabla^2 \psi_n(\mathbf{x})\, \mathrm{d}\mathbf{x}\,. \tag{4}$$

Exchange-correlation energy Since the exact form of the exchange-correlation energy is unknown, a number of approximations have been developed, the most popular ones being

the Local Density Approximation (LDA) [62] and the Generalized Gradient Approximation (GGA) [87]. In this work, we employ the LDA:

$$E_{xc}(\rho) = \int_{\mathbb{R}^3} \varepsilon_{xc}(\rho(\mathbf{x}))\rho(\mathbf{x})\,\mathrm{d}\mathbf{x}\,, \tag{5}$$

where $\varepsilon_{xc}(\rho) = \varepsilon_x(\rho) + \varepsilon_c(\rho)$ is the sum of the exchange and correlation per particle of a uniform electron gas.

Non-local pseudopotential energy The non-local pseudopotential energy can be written as

$$K(\Psi, \mathbf{g}, \mathbf{R}) = 2\sum_{n=1}^{N_s} g_n \sum_{J=1}^{N}\sum_{lm} \gamma_{Jl}\left(\int_{\mathbb{R}^3} \chi_{Jlm}(\mathbf{x}, \mathbf{R}_J)\psi_n(\mathbf{x})\mathrm{d}\mathbf{x}\right)^2, \tag{6}$$

where we have employed the Kleinman-Bylander [59] separable form for the pseudopotential. The coefficients γ_{Jl} and projection functions χ_{Jlm} are of the form

$$\begin{aligned}\gamma_{Jl} &= \left(\int_{\mathbb{R}^3} \chi_{Jlm}(\mathbf{x}, \mathbf{R}_J)u_{Jlm}(\mathbf{x}, \mathbf{R}_J)\,\mathrm{d}\mathbf{x}\right)^{-1}, \\ \chi_{Jlm}(\mathbf{x}, \mathbf{R}_J) &= u_{Jlm}(\mathbf{x}, \mathbf{R}_J)\left(V_{Jl}(\mathbf{x}, \mathbf{R}_J) - V_J(\mathbf{x}, \mathbf{R}_J)\right),\end{aligned} \tag{7}$$

where u_{Jlm} denote the isolated atom pseudowavefunctions and V_{Jl} represent the angular momentum dependent pseudopotentials, with l and m signifying the azimuthal and magnetic quantum numbers, respectively. In addition, V_J designate the local components of the pseudopotentials, and are typically set to be one of the angular momentum dependent components.

Electrostatic energy The electrostatic energy can be further decomposed as

$$E_{el}(\rho, \mathbf{R}) = \frac{1}{2}\int_{\mathbb{R}^3}\int_{\mathbb{R}^3} \frac{\rho(\mathbf{x})\rho(\mathbf{x}')}{|\mathbf{x}-\mathbf{x}'|}\,\mathrm{d}\mathbf{x}\,\mathrm{d}\mathbf{x}' + \sum_{J=1}^{N}\int_{\mathbb{R}^3}\rho(\mathbf{x})V_J(\mathbf{x}, \mathbf{R}_J)\,\mathrm{d}\mathbf{x} + \frac{1}{2}\sum_{I=1}^{N}\sum_{\substack{J=1\\J\neq I}}^{N}\frac{Z_I Z_J}{|\mathbf{R}_I - \mathbf{R}_J|}, \tag{8}$$

where the first term is the classical interaction energy of the electron density, also referred to as the Hartree energy. The second term is the interaction energy between the electron density and the nuclei, and the third term is the repulsion energy between the nuclei.

Electronic entropy The electronic entropy accounts for the partial orbital occupations, for which we choose the dependence that is appropriate for Fermions:

$$S(\mathbf{g}) = -2k_B \sum_{n=1}^{N_s} \left(g_n \log g_n + (1 - g_n) \log(1 - g_n) \right) , \tag{9}$$

where k_B is the Boltzmann constant.

Ground state The overall ground state in DFT is governed by the variational problem

$$\mathcal{F}_0 = \inf_{\mathbf{R}} \hat{\mathcal{F}}(\mathbf{R}) , \tag{10}$$

where

$$\hat{\mathcal{F}}(\mathbf{R}) = \inf_{\Psi, \mathbf{g}} \mathcal{F}(\Psi, \mathbf{g}, \mathbf{R}) \quad s.t. \quad \int_{\mathbb{R}^3} \psi_i(\mathbf{x}) \psi_j(\mathbf{x}) \, \mathrm{d}\mathbf{x} = \delta_{ij} , \quad 2 \sum_{n=1}^{N_s} g_n = N_e . \tag{11}$$

In this staggered scheme, the electronic ground-state as described by the above equation needs to be computed for every configuration of the nuclei encountered during the geometry optimization represented by Eqn. 10.

2.2 Real-space formulation

In this section, we describe the real-space formulation and parallel finite-difference implementation of Density Functional Theory (DFT) for isolated clusters. This represents the first component of the first principles code referred to as SPARC, an acronym representing Simulation Package for Ab-initio Real-space Calculations.

Electrostatic reformulation The electrostatic energy as presented in Eqn. 8 is inherently non-local, whereby a direct real-space implementation scales as $\mathcal{O}(N^2)$ with respect to the number of atoms. Moreover, it is inefficient in the context of parallel computing since a large amount of interprocessor communication is required. We overcome this by adopting a local formulation of the electrostatics [83, 101]:

$$\begin{aligned} E_{el}(\rho, \mathbf{R}) \quad &= \sup_{\phi} \left\{ -\frac{1}{8\pi} \int_{\mathbb{R}^3} |\nabla \phi(\mathbf{x}, \mathbf{R})|^2 \, \mathrm{d}\mathbf{x} + \int_{\mathbb{R}^3} (\rho(\mathbf{x}) + b(\mathbf{x}, \mathbf{R})) \phi(\mathbf{x}, \mathbf{R}) \, \mathrm{d}\mathbf{x} \right\} \\ &\quad - E_{self}(\mathbf{R}) + E_c(\mathbf{R}) , \end{aligned} \tag{12}$$

where ϕ is referred to as the electrostatic potential, and b is the total pseudocharge density of the nuclei. Specifically,

$$b(\mathbf{x},\mathbf{R}) = \sum_{J=1}^{N} b_J(\mathbf{x},\mathbf{R}_J)\,, \quad b_J(\mathbf{x},\mathbf{R}_J) = -\frac{1}{4\pi}\nabla^2 V_J(\mathbf{x},\mathbf{R}_J)\,, \quad \int_{\mathbb{R}^3} b_J(\mathbf{x},\mathbf{R}_J)\,\mathrm{d}\mathbf{x} = Z_J\,, \tag{13}$$

where b_J denotes the pseudocharge density of the J^{th} nucleus that generates the potential V_J. The second to last term in Eqn. 12 represents the self energy associated with the pseudocharge densities:

$$E_{self}(\mathbf{R}) = \frac{1}{2}\sum_{J=1}^{N}\int_{\mathbb{R}^3} b_J(\mathbf{x},\mathbf{R}_J)V_J(\mathbf{x},\mathbf{R}_J)\,\mathrm{d}\mathbf{x}\,. \tag{14}$$

The last term—identically zero for non-overlapping pseudocharge densities—corrects for the error in the repulsive energy when the pseudocharge densities overlap. The explicit expression for E_c can be found in Appendix A.

Electronic ground-state The electronic ground-state for a given position of nuclei is determined by the variational problem in Eqn. 11. The corresponding Euler-Lagrange equations are of the form

$$\begin{aligned}
&\left(\mathcal{H} \equiv -\frac{1}{2}\nabla^2 + V_{xc} + \phi + V_{nl}\right)\psi_n = \lambda_n\psi_n\,, \quad n = 1,2,\ldots,N_s\,,\\
&g_n = \left(1+\exp\left(\frac{\lambda_n-\lambda_f}{k_BT}\right)\right)^{-1}\,, \quad \text{where } \lambda_f \text{ is } s.t.\ 2\sum_{n=1}^{N_s} g_n = N_e\,,\\
&\rho(\mathbf{x}) = 2\sum_{n=1}^{N_s} g_n\psi_n^2(\mathbf{x})\,, \quad -\frac{1}{4\pi}\nabla^2\phi(\mathbf{x},\mathbf{R}) = \rho(\mathbf{x}) + b(\mathbf{x},\mathbf{R})\,,
\end{aligned} \tag{15}$$

where $\mathcal{H}$ is the Hamiltonian operator, $V_{xc} = \delta E_{xc}/\delta\rho$ is the exchange-correlation potential,

$$V_{nl}f = \sum_{J=1}^{N} V_{nl,J}f = \sum_{J=1}^{N}\sum_{lm}\gamma_{Jl}\chi_{Jlm}\int_{\mathbb{R}^3}\chi_{Jlm}(\mathbf{x},\mathbf{R}_J)f(\mathbf{x})\,\mathrm{d}\mathbf{x} \tag{16}$$

is the non-local pseudopotential operator, and λ_f is the Fermi energy.

The electronic ground-state is determined using the Self-Consistent Field (SCF) method [97]. Specifically, the non-linear eigenvalue problem described in Eqn. 15 is solved using

a fixed-point iteration—accelerated using mixing/extrapolation schemes [28, 69, 89, 9]—with respect to the potential $V_{eff} = V_{xc} + \phi$. In each iteration of the SCF method, the electron density is calculated by solving for the eigenfunctions of the linearized Hamiltonian, and the effective potential is evaluated by solving the Poisson equation for the electrostatic potential. Indeed, the calculation of the orthonormal Kohn-Sham orbitals scales asymptotically as $\mathcal{O}(N^3)$ with respect to the number of atoms. In order to overcome this restrictive scaling, $\mathcal{O}(N)$ approaches [41, 16] will be subsequently developed and implemented into SPARC.

Free energy In SPARC, the free energy is evaluated using the Harris-Foulkes [48, 33] type functional :

$$\begin{aligned}
\hat{\mathcal{F}}(\mathbf{R}) &= 2\sum_{n=1}^{N_s} g_n\lambda_n + \int_{\mathbb{R}^3} \varepsilon_{xc}(\rho(\mathbf{x}))\rho(\mathbf{x})\,\mathrm{d}\mathbf{x} - \int_{\mathbb{R}^3} V_{xc}(\rho(\mathbf{x}))\rho(\mathbf{x})\,\mathrm{d}\mathbf{x} \\
&+ \frac{1}{2}\int_{\mathbb{R}^3} (b(\mathbf{x},\mathbf{R}) - \rho(\mathbf{x}))\phi(\mathbf{x},\mathbf{R})\,\mathrm{d}\mathbf{x} - E_{self}(\mathbf{R}) + E_c(\mathbf{R}) \\
&+ 2k_BT\sum_{n=1}^{N_s} \left(g_n \log g_n + (1-g_n)\log(1-g_n)\right)\,, \qquad (17)
\end{aligned}$$

where E_{self} and E_c are as defined in Eqns. 14 and 92, respectively.

Atomic forces Once the electronic ground-state has been determined, the atomic forces are calculated using the following expression:

$$\begin{aligned}
\mathbf{f}_J &= -\frac{\partial\hat{\mathcal{F}}(\mathbf{R})}{\partial\mathbf{R}_J} \\
&= \int_{\mathbb{R}^3} \nabla b_J(\mathbf{x},\mathbf{R}_J)\left(\phi(\mathbf{x},\mathbf{R}) - V_J(\mathbf{x},\mathbf{R}_J)\right)\,\mathrm{d}\mathbf{x} + \mathbf{f}_{J,c}(\mathbf{R}) \qquad (18) \\
&\quad -4\sum_{n=1}^{N_s} g_n \sum_{lm} \gamma_{Jl}\left(\int_{\mathbb{R}^3} \psi_n(\mathbf{x})\chi_{Jlm}(\mathbf{x},\mathbf{R}_J)\,\mathrm{d}\mathbf{x}\right)\left(\int_{\mathbb{R}^3} \nabla\psi_n(\mathbf{x})\chi_{Jlm}(\mathbf{x},\mathbf{R}_J)\,\mathrm{d}\mathbf{x}\right)\,.
\end{aligned}$$

The first term is the local component of the force [99], and the second term—expression presented in Appendix A—represents the electrostatic correction in the forces when the pseudocharge densities overlap [101]. The final term, which represents the non-local component of the atomic force, has been obtained by transferring the derivative on the non-local

projectors (with respect to the atomic position) to the orbitals (with respect to space) [50]. This strategy has been adopted since the orbitals are typically much smoother than the projectors, which enables more accurate atomic forces to be obtained [90].

Overview of SPARC SPARC has been implemented in the framework of the Portable, Extensible Toolkit for scientific computations (PETSc) [5, 6] suite of data structures and routines. The electronic and structural ground-states for isolated clusters are determined using the methodology outlined in Fig. 1, whose key components are discussed in detail in the sections below.

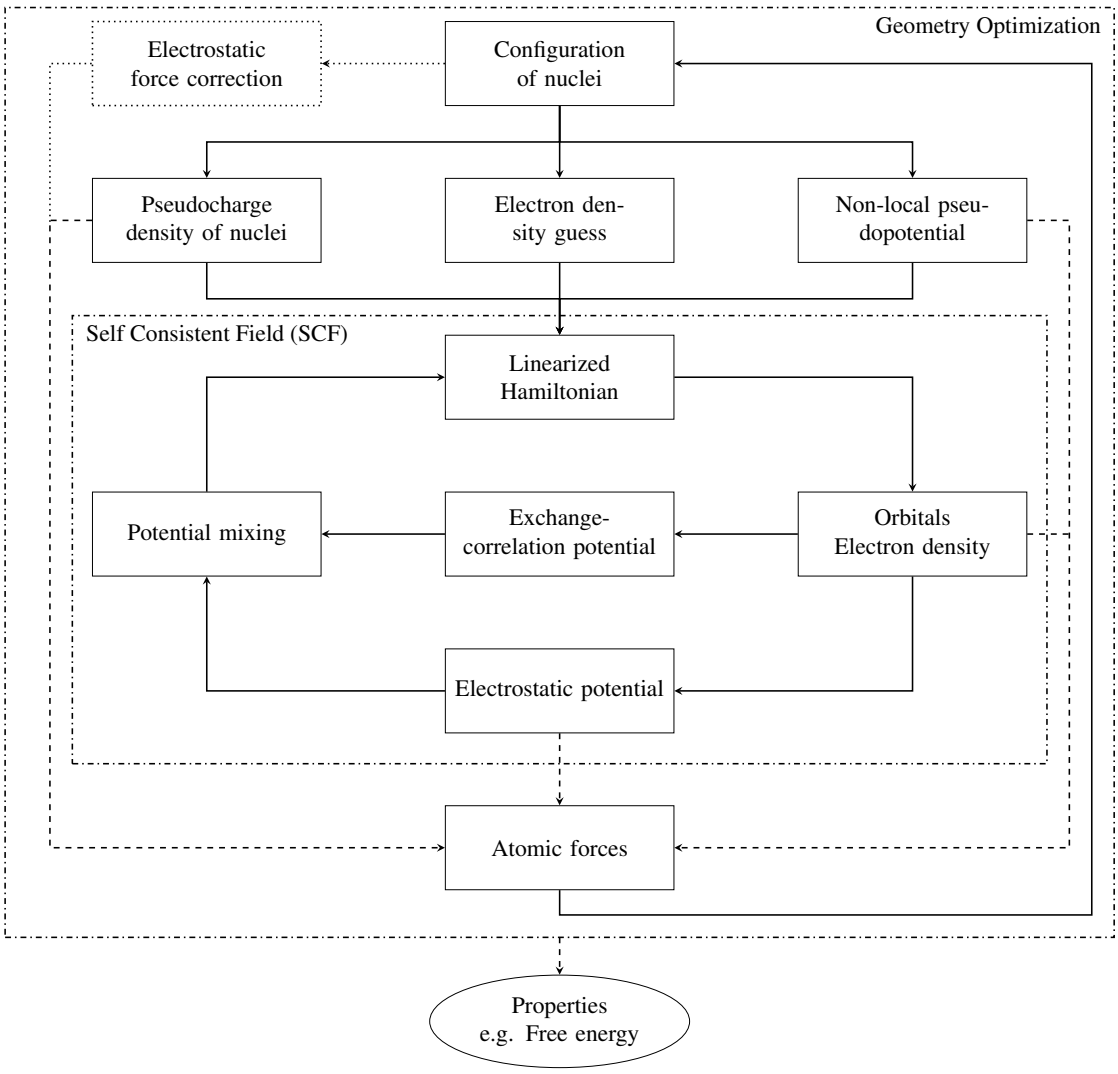

Figure 1: Outline of ground-state DFT simulations in SPARC for isolated clusters.

2.3 Finite-difference implementation

The simulations are performed on a cuboidal domain Ω with boundary $\partial\Omega$ and sides of length L_1, L_2 and L_3. The domain Ω is discretized using a uniform finite-difference grid with spacing h such that $L_1 = n_1 h$, $L_2 = n_2 h$ and $L_3 = n_3 h$, where $n_1, n_2, n_3 \in \mathbb{N}$, $\mathbb{N}$ being the set of all natural numbers. Each node in the finite-difference grid is indexed by (i, j, k), where $i = 1, 2, \ldots, n_1$, $j = 1, 2, \ldots, n_2$ and $k = 1, 2, \ldots, n_3$. We approximate the

Laplacian of any function f at the grid point (i,j,k) using finite-differences:

$$\begin{aligned}&\nabla_h^2 f\Big|^{(i,j,k)}\\&\approx \sum_{p=0}^{n_o} w_p \Big(f^{(i+p,j,k)} + f^{(i-p,j,k)} + f^{(i,j+p,k)} + f^{(i,j-p,k)} + f^{(i,j,k+p)} + f^{(i,j,k-p)} \Big),\end{aligned} \tag{19}$$

where $f^{(i,j,k)}$ represents the value of the function f at the node (i,j,k). The weights w_p are given by [74, 36]

$$\begin{aligned} w_0 &= -\frac{1}{h^2}\sum_{q=1}^{n_o}\frac{1}{q^2}, \\ w_p &= \frac{2(-1)^{p+1}}{h^2 p^2}\frac{(n_o!)^2}{(n_o-p)!(n_o+p)!}, \ p = 1,2,\ldots,n_o. \end{aligned} \tag{20}$$

Similarly, we approximate the gradient using the finite-difference approximation:

$$\begin{aligned}\nabla_h f\Big|^{(i,j,k)} \approx \sum_{p=1}^{n_o} \tilde{w}_p \Big(&(f^{(i+p,j,k)} - f^{(i-p,j,k)})\hat{\mathbf{e}}_1 + \\ &(f^{(i,j+p,k)} - f^{(i,j-p,k)})\hat{\mathbf{e}}_2 + (f^{(i,j,k+p)} - f^{(i,j,k-p)})\hat{\mathbf{e}}_3 \Big),\end{aligned} \tag{21}$$

where $\hat{\mathbf{e}}_1$, $\hat{\mathbf{e}}_2$ and $\hat{\mathbf{e}}_3$ signify unit vectors along the edges of Ω, and the weights [74, 36]

$$\tilde{w}_p = \frac{(-1)^{p+1}}{hp}\frac{(n_o!)^2}{(n_o-p)!(n_o+p)!}, \ p = 1,2,\ldots,n_o. \tag{22}$$

These finite-difference expressions for the Laplacian and gradient represent $\mathcal{O}(h^{2n_o})$ accurate approximations. We enforce zero Dirichlet boundary conditions by setting $f^{(i,j,k)} = 0$ for any index that does not correspond to a node in the finite-difference grid. While performing spatial integrations, we assume that the function f is constant in a cube of side h around each grid point, i.e.,

$$\int_\Omega f(\mathbf{x})\,\mathrm{d}\mathbf{x} \approx h^3 \sum_{i=1}^{n_1}\sum_{j=1}^{n_2}\sum_{k=1}^{n_3} f^{(i,j,k)}. \tag{23}$$

The Euler-Lagrange equation discretized in the finite-difference framework is obtained by taking variations of the discrete free energy with the integrals represented using the integration rule presented in Eqn. 23. Using this integration rule, we approximate the non-local

pseudopotential operator as

$$V_{nl}f\big|^{(i,j,k)} = \sum_{J=1}^{N} V_{nl,J}f\big|^{(i,j,k)} \approx h^3 \sum_{J=1}^{N} \sum_{lm} \sum_{p=1}^{n_1} \sum_{q=1}^{n_2} \sum_{r=1}^{n_3} \gamma_{Jl} \chi_{Jlm}^{(i,j,k)} \chi_{Jlm}^{(p,q,r)} f^{(p,q,r)} \,. \quad (24)$$

Henceforth, we denote the Hamiltonian matrix resulting from the above discretization by $\mathbf{H} \in \mathbb{R}^{N_d \times N_d}$, where $N_d = n_1 \times n_2 \times n_3$ is the total number of finite-difference nodes used to discretize Ω. In addition, we represent the eigenvalues of $\mathbf{H}$ arranged in ascending order by $\lambda_1, \lambda_2, \ldots, \lambda_{N_d}$. We store the discrete Laplacian in compressed row format, and store the discrete orbitals as the columns of the dense matrix $\mathbf{\Psi} \in \mathbb{R}^{N_d \times N_s}$. During parallel computations, we partition the domain as $\Omega = \bigcup_{p=1}^{n_p} \Omega_p$, where Ω_p denotes the domain local to the p^{th} processor, and n_p is the total number of processors. The specific choice of Ω_p corresponds to the PETSc default for structured grids.

2.3.1 Pseudocharge density generation and self energy calculation

In each step of geometry optimization, the pseudocharge densities are assigned to the grid using the finite-difference approximated Laplacian [99, 101]:

$$b^{(i,j,k)} = \sum_{J=1}^{N} b_J^{(i,j,k)} \,, \quad b_J^{(i,j,k)} = -\frac{1}{4\pi} \nabla_h^2 V_J\big|^{(i,j,k)} \,. \quad (25)$$

The associated discrete self energy is of the form

$$E_{self}^h = \frac{1}{2} h^3 \sum_{J=1}^{N} \sum_{i=1}^{n_1} \sum_{j=1}^{n_2} \sum_{k=1}^{n_3} b_J^{(i,j,k)} V_J^{(i,j,k)} \,. \quad (26)$$

Since each radially symmetric pseudopotential V_J matches the Coulomb potential outside some prespecified cutoff radius r_J^c, the continuous pseudocharge density b_J has compact support in a sphere of radius r_J^c centered at $\mathbf{R}_J$. This is not the case for the corresponding discrete pseudocharge density $b_J^{(i,j,k)}$, which actually has infinite extent due to the use of the finite-difference Laplacian (Eqn. 25). However, $b_J^{(i,j,k)}$ has exponential decay away from $\mathbf{R}_J$ (Appendix C), which allows for truncation at some suitably chosen radius r_J^b. It is worth noting that even though the discrete pseudocharge densities may overlap, as long as there is no overlap between the continuous pseudocharge densities, the electrostatic

correction to the energy and forces (i.e., E_c and $\mathbf{f}_{J,c}$) both rapidly converge to zero as the mesh is refined. This is a consequence of the finite-difference Laplacian being used to assign the pseudocharge densities on to the mesh, with the corresponding inverse operation being performed during the solution of the Poisson equation in Eqn. 15.

We calculate the total pseudocharge density $b^{(i,j,k)}$ and the corresponding self energy E^h_{self} using the approach outlined in Algorithm 1. Specifically, we first determine the overlap of $\Omega_{r^b_J}$ with the processor domains Ω_p, where $\Omega_{r^b_J}$ denotes the cube with side of length $2r^b_J$ centered on the J^{th} atom. We have chosen a cube rather than a sphere due to its simplicity and efficiency within the Euclidean finite-difference discretization. The value of r^b_J for every type of atom—determined at the start of the complete DFT simulation—is chosen such that the charge constraint in Eqn. 13 is satisfied to within a prespecified tolerance ε_b, i.e.,

$$\left| h^3 \sum_{i=1}^{n_1} \sum_{j=1}^{n_2} \sum_{k=1}^{n_3} b_J^{(i,j,k)} - Z_J \right| < \varepsilon_b \, . \tag{27}$$

While describing Algorithm 1, we use the subscripts s and e to denote the starting and ending indices of $\Omega_{r^b_J} \cap \Omega_p \neq \emptyset$, respectively. In this overlap region (and an additional $2n_0$ points in each direction), we interpolate $V_J^{(i,j,k)}$ on to the finite-difference grid using cubic-splines [1]. Next, we utilize Eqns. 25 and 26 to compute $b^{(i,j,k)}$ and $E^{h,p}_{self}$, where $E^{h,p}_{self}$ is the contribution of the p^{th} processor to the self energy. Finally, we sum the contributions from all the processors to obtain the total self energy E^h_{self}.

The local and independent nature of the aforedescribed computations ensure that they possess good weak and strong parallel scalability. However, the approach as presented here is formally slightly worse than $\mathcal{O}(N)$ with respect to the number of atoms. In order to achieve perfect $\mathcal{O}(N)$ scaling, the atoms need to be suitably distributed amongst the processors (in $\mathcal{O}(N)$ time), whereby each processor is only required to go over the local subset of atoms. However, for the modest system sizes studied in ab-initio calculations, the adopted approach is both simple and efficient. Moreover, this part of the calculation constitutes a very minor fraction of the total computational effort.

Algorithm 1: Pseudocharge density generation and self energy calculation

Input: $\mathbf{R}$, V_J, and r_J^b

$b^{(i,j,k)} = 0$, $E_{self}^{h,p} = 0$

for $J = 1 \ldots N$ **do**

  if $\Omega_{r_J^b} \cap \Omega_p \neq \emptyset$ **then**

    Determine starting and ending indices i_s, i_e, j_s, j_e, k_s, k_e for $\Omega_{r_J^b} \cap \Omega_p$

    Determine $V_J^{(i,j,k)}$ $\forall\, i \in [i_s - n_o, i_e + n_o]$, $j \in [j_s - n_o, j_e + n_o]$,

    $k \in [k_s - n_o, k_e + n_o]$

    $b_J^{(i,j,k)} = -\frac{1}{4\pi}\nabla_h^2 V_J\big|^{(i,j,k)}$, $\quad b^{(i,j,k)} = b^{(i,j,k)} + b_J^{(i,j,k)}$ $\forall\, i \in [i_s, i_e]$, $j \in [j_s, j_e]$,

    $k \in [k_s, k_e]$

    $E_{self}^{h,p} = E_{self}^{h,p} + \frac{1}{2}h^3 b_J^{(i,j,k)} V_J^{(i,j,k)}$ $\forall\, i \in [i_s, i_e]$, $j \in [j_s, j_e]$, $k \in [k_s, k_e]$

$E_{self}^{h} = \sum_{p=1}^{n_p} E_{self}^{h,p}$

Output: $b^{(i,j,k)}$ and E_{self}^{h}

2.3.2 Electrostatic potential calculation

The electrostatic potential ϕ—solution to the Poisson problem in Eqn. 15 on all of space $\mathbb{R}^3$—needs to be computed in each iteration of the SCF method as part of the linearized Hamiltonian $\mathbf{H}$. However, since all calculations are restricted to Ω, appropriate boundary conditions need to be prescribed on $\partial\Omega$ in order to minimize the finite-domain effect. Indeed, the simplest choice of zero Dirichlet boundary conditions can result in very slow convergence with domain size, as is evident from the discussion that follows. The electrostatic potential can be written in integral form using the Green's function of the Laplacian:

$$\phi(\mathbf{x}) = \int_{\mathbb{R}^3} \frac{\rho(\mathbf{x}') + b(\mathbf{x}', \mathbf{R})}{|\mathbf{x} - \mathbf{x}'|}\, \mathrm{d}\mathbf{x}' \approx \int_{\Omega} \frac{\rho(\mathbf{x}') + b(\mathbf{x}', \mathbf{R})}{|\mathbf{x} - \mathbf{x}'|}\, \mathrm{d}\mathbf{x}' \,, \tag{28}$$

where the exponential decay of the electron density ρ and total pseudocharge b has been used to restrict the integral to Ω. On performing a multipole expansion of the kernel $1/|\mathbf{x} - \mathbf{x}'|$, we arrive at

$$\phi(\mathbf{x}) = \sum_{l=0}^{\infty} \sum_{m=-l}^{l} \frac{4\pi}{(2l+1)|\mathbf{x}|^{l+1}} Y_{lm}\left(\frac{\mathbf{x}}{|\mathbf{x}|}\right) \int_{\Omega} |\mathbf{x}'|^l Y_{lm}\left(\frac{\mathbf{x}'}{|\mathbf{x}'|}\right) (\rho(\mathbf{x}') + b(\mathbf{x}'))\mathrm{d}\mathbf{x}' \,, \tag{29}$$

where Y_{lm} are the real spherical harmonics. It can therefore be deduced that unlike ρ and b, in general ϕ only has algebraic decay away from the cluster. Therefore, significant errors can result when zero Dirichlet boundary conditions are employed, particularly for systems with net charge and/or dipole moment. In order to mitigate this, we adopt the procedure described below.

We write the discrete form of the Poisson problem in Eqn. 15 as

$$-\frac{1}{4\pi}\nabla_h^2\phi\Big|^{(i,j,k)} = \rho^{(i,j,k)} + b^{(i,j,k)} - d^{(i,j,k)}\,, \tag{30}$$

where zero Dirichlet boundary conditions are prescribed on $\partial\Omega$, and the 'charge correction' [19]

$$\begin{aligned} d^{(i,j,k)} &= \frac{-1}{4\pi}\sum_{p=0}^{n_o} w_p\Big(\chi^{(i+p,j,k)}\phi^{(i+p,j,k)} + \chi^{(i-p,j,k)}\phi^{(i-p,j,k)} + \chi^{(i,j+p,k)}\phi^{(i,j+p,k)} \\ &+ \chi^{(i,j-p,k)}\phi^{(i,j-p,k)} + \chi^{(i,j,k+p)}\phi^{(i,j,k+p)} + \chi^{(i,j,k-p)}\phi^{(i,j,k-p)}\Big)\,. \end{aligned} \tag{31}$$

In the above expression, w_p are the finite-difference weights given by Eqn. 20, and χ is the indicator function that takes values of 0 and 1 when the index does and does not belong to the finite-difference grid, respectively. The values of $\phi^{(i,j,k)}$ corresponding to $\chi^{(i,j,k)} = 1$ are calculated using the discrete truncated version of the multipole expansion in Eqn. 29:

$$\phi^{(i,j,k)} = \sum_{l=0}^{l_{max}}\sum_{m=-l}^{l}\frac{4\pi}{(2l+1)|\mathbf{x}^{(i,j,k)}|^{l+1}}Y_{lm}^{(i,j,k)}Q_{lm}^h\,, \tag{32}$$

where l_{max} is the maximum angular momentum component, and the discrete multipole moments

$$Q_{lm}^h = h^3\sum_{r=1}^{n_1}\sum_{s=1}^{n_2}\sum_{t=1}^{n_3}|\mathbf{x}^{(r,s,t)}|^l Y_{lm}^{(r,s,t)}(\rho^{(r,s,t)} + b^{(r,s,t)})\,. \tag{33}$$

It is worth noting that the evaluation of Q_{lm} is independent of the position at which the electrostatic potential needs to be evaluated. Therefore, the cost of calculating the compensating charge is $\mathcal{O}(N_d) + \mathcal{O}(N_d^{2/3})$, which makes its scaling $\mathcal{O}(N)$ with respect to the number of atoms. The associated prefactors are insignificant since l_{max} is typically very small, and $d^{(i,j,k)}$ only needs to be computed for grid points which lie within a distance of

$(n_o - 1)h$ from the boundary $\partial\Omega$. Therefore, the electrostatic potential ϕ can be determined in $\mathcal{O}(N)$ time when sophisticated preconditioners like multigrid [47] are employed for solving the linear system in Eqn. 30. The above strategy is expected to minimize the finite-domain effect resulting from the slow decay of the electrostatic potential, which is indeed verified by the results presented in Section 3.4.

2.3.3 Electron density calculation

In each iteration of the SCF method, the electron density corresponding to the linearized Hamiltonian $\mathbf{H}$ needs to be evaluated. This is typically the most computationally expensive step in DFT calculations. In this work, we utilize the Chebyshev filtered subspace iteration (CheFSI) [110, 109] to compute approximations to the lowest N_s eigenvalues and corresponding eigenvectors of $\mathbf{H}$. This choice of eigensolver is motivated by the minimal orthogonalization and computer memory costs compared to other eigensolvers commonly employed in electronic structure calculations, e.g. Locally Optimal Block Preconditioned Conjugate Gradient (LOBPCG) [60]. Moreover, the lack of efficient real-space preconditioners limits the effectiveness of diagonalization approaches like LOBPCG in the current setting. In fact, CheFSI has been found to outperform LOBPCG for large scale computations even in the context of plane-waves [68].

The CheFSI algorithm as implemented in SPARC consists of three main steps. First, we filter the guess orbitals $\mathbf{\Psi}$ using Chebyshev polynomials:

$$\mathbf{\Psi_f} = p_m(\mathbf{H})\mathbf{\Psi}\,, \quad p_m(t) = C_m\left(\frac{t-c}{e}\right)\,, \tag{34}$$

where $\mathbf{\Psi_f}$ represents the collection of filtered orbitals, and C_m denotes the Chebyshev polynomial of degree m. In addition, $e = (\lambda_{N_d} - \lambda_c)/2$ and $c = (\lambda_{N_d} + \lambda_c)/2$, where λ_c signifies the cutoff chosen for the Chebyshev polynomial filter. The central idea of this technique is to use the rapid growth of Chebyshev polynomials outside the interval $[-1, 1]$ to dampen all the eigencomponents corresponding to eigenvalues larger than λ_c. The matrix $p_m(\mathbf{H})$ is not explicitly determined, rather its product with $\mathbf{\Psi}$ is computed using the three

term recurrence relation of Chebyshev polynomials, as outlined in Algorithm 2.

Algorithm 2: Chebyshev filtering

Input: $\mathbf{H}$, $\mathbf{\Psi}$, m, λ_1, λ_{N_d}, λ_c

$e = \frac{\lambda_{N_d} - \lambda_c}{2}$; $c = \frac{\lambda_{N_d} + \lambda_c}{2}$; $\sigma = \frac{e}{\lambda_1 - c}$

$\mathbf{\Psi_f} = \frac{\sigma}{e}\left(\mathbf{H} - c\mathbf{I}\right)\mathbf{\Psi}$

for $j = 2 : m$ **do**

  $\tilde{\mathbf{\Psi}}_\mathbf{f} = \frac{2\sigma}{e}\left(\mathbf{H} - c\mathbf{I}\right)\mathbf{\Psi_f} - \left(\frac{\sigma^2}{2-\sigma^2}\right)\mathbf{\Psi}$

  $\mathbf{\Psi} = \mathbf{\Psi_f}$; $\mathbf{\Psi_f} = \tilde{\mathbf{\Psi}}_\mathbf{f}$; $\sigma = \frac{\sigma}{2-\sigma^2}$

Output: $\mathbf{\Psi_f}$

Next, we project onto the filtered basis $\mathbf{\Psi_f}$ to arrive at the generalized eigenproblem:

$$\mathbf{H_s y_n} = \lambda_n \mathbf{M_s y_n}\,, \quad n = 1, 2, \ldots N_s\,, \tag{35}$$

whose eigenvalues represent approximations to those of the Hamiltonian $\mathbf{H}$. The dense matrices $\mathbf{H_s}, \mathbf{M_s} \in \mathbb{R}^{N_s \times N_s}$ are obtained using the relations

$$\mathbf{H_s} = \mathbf{\Psi_f^T H \Psi_f}\,, \quad \mathbf{M_s} = \mathbf{\Psi_f^T \Psi_f}\,. \tag{36}$$

After solving the eigenproblem in Eqn. 35, we calculate the Fermi energy λ_f by enforcing the constraint on the total number of electrons:

$$2\sum_{n=1}^{N_s} g_n = N_e\,, \quad \text{where} \quad g_n = \left(1 + \exp\left(\frac{\lambda_n - \lambda_f}{k_B T}\right)\right)^{-1}\,. \tag{37}$$

Finally, we perform the subspace rotation

$$\mathbf{\Psi} = \mathbf{\Psi_f Y}\,, \tag{38}$$

where the columns of the matrix $\mathbf{Y} \in \mathbb{R}^{N_s \times N_s}$ contain the eigenvectors $\mathbf{y_n}$. The columns of $\mathbf{\Psi}$ so obtained represent approximations to the eigenvectors of $\mathbf{H}$, which are then used to calculate the electron density at the finite-difference grid points:

$$\rho^{(i,j,k)} = \frac{2}{h^3}\sum_{n=1}^{N_s} g_n\, \psi_n^{2(i,j,k)}\,, \tag{39}$$

where $\psi_n^{(i,j,k)}$ are extracted from the n^{th} column of $\mathbf{\Psi}$.

In the very first SCF iteration of the complete DFT simulation, we start with a randomly generated $\mathbf{\Psi}$, and repeat the steps in CheFSI—without calculating/updating the electron density—multiple times (~ 3) [111]. This allows us to obtain a good approximation of the electron density for the second SCF iteration. In principle, this can be achieved by performing the CheFSI steps only once but with a higher degree Chebyshev polynomial m. However, in practice this causes the orbitals to become linearly dependent, which is prevented in the current procedure by the orthogonalization step within CheFSI. In every subsequent SCF iteration, we perform the CheFSI steps only once with the subspace rotated $\mathbf{\Psi}$ from the previous step as the initial guess. Overall, the calculation of the electron density scales as $\mathcal{O}(N_s N_d)+\mathcal{O}(N_s^2 N_d)+\mathcal{O}(N_s^3)$, which makes it $\mathcal{O}(N^3)$ with respect to the number of atoms.

2.3.4 Free energy calculation

We approximate the integrals in Eqn. 17 using the integration rule in Eqn. 23 to arrive at the following expression for the discrete free energy:

$$\begin{aligned}\hat{\mathcal{F}}^h &= 2\sum_{n=1}^{N_s} g_n\lambda_n \\ &+h^3\sum_{i=1}^{n_1}\sum_{j=1}^{n_2}\sum_{k=1}^{n_3}\left(\varepsilon_{xc}^{(i,j,k)}\rho^{(i,j,k)} - V_{xc}^{(i,j,k)}\rho^{(i,j,k)} + \frac{1}{2}(b^{(i,j,k)}-\rho^{(i,j,k)})\phi^{(i,j,k)}\right) \\ &-E_{self}^h + E_c^h + 2k_BT\sum_{n=1}^{N_s}\left(g_n\log g_n + (1-g_n)\log(1-g_n)\right)\,, \end{aligned} \tag{40}$$

where E_{self}^h is the discrete self energy of the pseudocharges (Eqn. 26), and E_c^h is the discrete repulsive energy correction due to overlapping pseudocharges (Eqn. 95). The evaluation of $\hat{\mathcal{F}}^h$ scales as $\mathcal{O}(N_d)$, and therefore $\mathcal{O}(N)$ with respect to the number of atoms. Even though the free energy needs to be calculated only after the electronic/structural ground-state is determined, it is computed during each step of the SCF method, as is common practice in electronic structure calculations. We remark that for GGA approximation of the exchange-correlation energy, the derivative of the electron density at the finite-difference

grid points can be calculated by directly applying the gradient on the electron density using Eqn. 21.

2.3.5 Atomic forces calculation

The discrete form of the atomic force presented in Eqn. 18 is the sum of three components:

$$\mathbf{f}_J^h = \mathbf{f}_{J,loc}^h + \mathbf{f}_{J,c}^h + \mathbf{f}_{J,nloc}^h \,, \tag{41}$$

where $\mathbf{f}_{J,loc}^h$ is the discrete local component of the force, $\mathbf{f}_{J,c}^h$ is the discrete electrostatic correction for overlapping pseudocharges, and $\mathbf{f}_{J,nloc}^h$ is the discrete non-local component of the force. Below, we present expressions for $\mathbf{f}_{J,loc}^h$ and $\mathbf{f}_{J,nloc}^h$, and discuss their evaluation in SPARC. The expression for $\mathbf{f}_{J,c}^h$ can be found in Eqn. 96, and its evaluation progresses along similar lines as $\mathbf{f}_{J,loc}^h$.

Local component The local component of the atomic force in discrete form can be written as

$$\mathbf{f}_{J,loc}^h = h^3 \sum_{i=1}^{n_1} \sum_{j=1}^{n_2} \sum_{k=1}^{n_3} \nabla_h b_J \big|^{(i,j,k)} (\phi^{(i,j,k)} - V_J^{(i,j,k)}) \,, \tag{42}$$

where the integral in Eqn. 18 has been approximated using the integration rule in Eqn. 23. The calculation of $\mathbf{f}_{J,loc}^h$ proceeds as outlined in Algorithm 3. Specifically, $V_J^{(i,j,k)}$ is interpolated on to the finite-difference grid in the overlap region $\Omega_{r_J^b} \cap \Omega_p \neq \emptyset$ (and an additional $4n_0$ points in each direction) using cubic-splines, from which $b_J^{(i,j,k)}$ is calculated using Eqn. 25. Subsequently, $\mathbf{f}_{J,loc}^{h,p}$—contribution of the p^{th} processor to the local component of the force—is calculated using Eqn. 42. Finally, the contributions from all processors are summed to simultaneously obtain $\mathbf{f}_{J,loc}^h$ for all the atoms.

Algorithm 3: Calculation of the local component of the atomic force.

Input: $\mathbf{R}$, $\phi^{(i,j,k)}$, V_J, and r_J^b

for $J = 1 \ldots N$ **do**

  if $\Omega_{r_J^b} \cap \Omega_p \neq \emptyset$ **then**

    Determine starting and ending indices i_s, i_e, j_s, j_e, k_s, k_e for $\Omega_{r_J^b} \cap \Omega_p$

    Determine $V_J^{(i,j,k)}$ $\forall\, i \in [i_s - 2n_o, i_e + 2n_o]$, $j \in [j_s - 2n_o, j_e + 2n_o]$,

    $k \in [k_s - 2n_o, k_e + 2n_o]$

    $b_J^{(i,j,k)} = -\frac{1}{4\pi}\nabla_h^2 V_J\big|^{(i,j,k)}$ $\forall\, i \in [i_s - n_o, i_e + n_o]$, $j \in [j_s - n_o, j_e + n_o]$,

    $k \in [k_s - n_o, k_e + n_o]$

    $\mathbf{f}_{J,loc}^{h,p} = h^3 \sum_{i=i_s}^{i_e} \sum_{j=j_s}^{j_e} \sum_{k=k_s}^{k_e} \nabla_h b_J\big|^{(i,j,k)} (\phi^{(i,j,k)} - V_J^{(i,j,k)})$

  $\mathbf{f}_{J,loc}^{h} = \sum_{p=1}^{n_p} \mathbf{f}_{J,loc}^{h,p}$

Output: $\mathbf{f}_{J,loc}^{h}$

Non-local component The non-local component of the force in discrete form can be written as

$$\mathbf{f}_{J,nloc}^{h} = -4 \sum_{n=1}^{N_s} g_n \sum_{lm} \gamma_{Jl} Y_{Jnlm} \mathbf{W}_{Jnlm}\,. \tag{43}$$

where

$$Y_{Jnlm} = h^3 \sum_{i=1}^{n_1} \sum_{j=1}^{n_2} \sum_{k=1}^{n_3} \psi_n^{(i,j,k)} \chi_{Jlm}^{(i,j,k)}\,, \quad \mathbf{W}_{Jnlm} = h^3 \sum_{i=1}^{n_1} \sum_{j=1}^{n_2} \sum_{k=1}^{n_3} \nabla_h \psi_n\big|^{(i,j,k)} \chi_{Jlm}^{(i,j,k)}\,. \tag{44}$$

Again, the integral in Eqn. 18 has been approximated using the integration rule in Eqn. 23. The calculation of $\mathbf{f}_{J,nloc}^{h}$ in SPARC proceeds as summarized in Algorithm 4. We first determine the overlap of $\Omega_{r_J^c}$ with the processor domains Ω_p, where $\Omega_{r_J^c}$ denotes the cube with side of length $2r_J^c$ centered on the J^{th} atom. The value of r_J^c corresponds to the maximum cutoff radius amongst the non-local components of the pseudopotential for the J^{th} atom. We have chosen a cube rather than a sphere due to its simplicity and efficiency within the Euclidean finite-difference discretization. While describing Algorithm 4, we use the subscripts s and e to denote the starting and ending indices of $\Omega_{r_J^c} \cap \Omega_p \neq \emptyset$, respectively. In this overlap region, we interpolate the radial components of the projectors $\chi_{Jlm}^{(i,j,k)}$ on to

the finite-difference grid using cubic-splines. Next, we utilize Eqn. 44 to determine Y^p_{Jnlm} and $\mathbf{W}^p_{Jnlm}$, which represent the contributions of the p^{th} processor to Y_{Jnlm} and $\mathbf{W}_{Jnlm}$, respectively. Finally, we sum the contributions from all the processors to obtain Y_{Jnlm} and $\mathbf{W}_{Jnlm}$, which are then used to calculate $\mathbf{f}^h_{J,nloc}$ using Eqn. 43 .

Algorithm 4: Calculation of the non-local component of the atomic force

Input: $\mathbf{R}$, $\psi_n^{(i,j,k)}$, γ_{Jl}, χ_{Jlm}, and r_J^c

$Y^p_{Jnlm} = 0$, $\mathbf{W}^p_{Jnlm} = 0$

for $J = 1 \ldots N$ **do**

  if $\Omega_{r_J^c} \cap \Omega_p \neq \emptyset$ **then**

    Determine starting and ending indices i_s, i_e, j_s, j_e, k_s, k_e for $\Omega_{r_J^c} \cap \Omega_p$

    Determine $\chi_{Jlm}^{(i,j,k)}$ $\forall\, i \in [i_s, i_e]$, $j \in [j_s, j_e]$, $k \in [k_s, k_e]$

    $Y^p_{Jnlm} = Y^p_{Jnlm} + h^3 \psi_n^{(i,j,k)} \chi_{Jlm}^{(i,j,k)}$ $\forall\, i \in [i_s, i_e]$, $j \in [j_s, j_e]$, $k \in [k_s, k_e]$

    $\mathbf{W}^p_{Jnlm} = \mathbf{W}^p_{Jnlm} + h^3 \nabla_h \psi_n \big|^{(i,j,k)} \chi_{Jlm}^{(i,j,k)}$ $\forall\, i \in [i_s, i_e]$, $j \in [j_s, j_e]$, $k \in [k_s, k_e]$

$Y_{Jnlm} = \sum_{p=1}^{n_p} Y^p_{Jnlm}$, $\mathbf{W}_{Jnlm} = \sum_{p=1}^{n_p} \mathbf{W}^p_{Jnlm}$

$\mathbf{f}^h_{J,nloc} = -4 \sum_{n=1}^{N_s} g_n \sum_{lm} \gamma_{Jl} Y_{Jnlm} \mathbf{W}_{Jnlm}$

Output: $\mathbf{f}^h_{J,nloc}$

2.4 Examples and Results

In this section, we verify the proposed finite-difference formulation and parallel implementation of DFT for isolated clusters—first component of SPARC (Simulation Package for Ab-initio Real-space Calculations)—through selected examples. In all the simulations, we utilize a twelfth-order accurate finite-difference discretization ($n_o = 6$), the Perdew-Wang parametrization [86] of the correlation energy calculated by Ceperley-Alder [24], a smearing of $k_B T = 1 \times 10^{-3}$ Ha, and norm-conserving Troullier-Martins pseudopotentials [103]. The values of cutoff radii for the non-local projectors and the choice of local component of the pseudopotentials are specified in Appendix B.

We truncate the discrete multipole expansion presented in Eqn. 32 at $l_{max} = 6$. We

solve the linear system in Eqn. 30—discrete form of the Poisson problem in Eqn. 15—using the Conjugate Gradient method (CG) [49] with the block-Jacobi preconditioner [42]. In the CheFSI method, we determine the extremal eigenvalues of the Hamiltonian $\mathbf{H}$ using a few iterations of the Lanczos method [66], set the number of states to be $N_s = N_e/2 + 30$, utilize a polynomial of degree $m = 20$ for Chebyshev filtering, and choose the filter cutoff λ_c to be the previous iteration's Fermi energy plus 0.1 Ha. Further, we solve the generalized eigenproblem in Eqn. 35 using the QR algorithm [106] as implemented in LAPACK [3]. We calculate the Fermi energy—root of the constraint in Eqn. 37—using Brent's method [91]. We use Anderson mixing [2] with relaxation parameter of 0.3 and mixing history of 7 for accelerating the convergence of the Self-Consistent Field (SCF) method. Finally, we employ the Polak-Ribiere variant of non-linear conjugate gradients with a secant line search [94] for performing geometry optimization.

In this work, we define chemical accuracy as the error of 0.001 Ha/atom in energy and 0.001 Ha/Bohr in forces, defined with respect to the converged ABINIT results. In all the calculations, the energy and forces are converged to within the chemical accuracy. Wherever applicable, the results obtained by SPARC are compared to the well established plane-wave code ABINIT [43, 45, 44]. The error in energy is defined as the difference in the magnitude, and the error in forces is defined to be the maximum difference in any component on any atom. The simulations are performed on a computer cluster consisting of 16 nodes with the following configuration: Altus 1804i Server - 4P Interlagos Node, Quad AMD Opteron 6276, 16C, 2.3 GHz, 128GB, DDR3-1333 ECC, 80GB SSD, MLC, 2.5" HCA, Mellanox ConnectX 2, 1-port QSFP, QDR, memfree, CentOS, Version 5, and connected through InfiniBand cable.

2.4.1 Convergence with domain size

We first verify the convergence of the computed energy and atomic forces with respect to the size of the domain Ω. We choose the carbon monoxide (CO) and water (H_2O)

molecules as representative examples, with the C-O and O-H bond lengths reduced and increased by 8% from their equilibrium values as determined by ABINIT, respectively. The polar nature of the molecules and their deliberate asymmetric positioning within Ω ensure that any finite-domain effects are exaggerated. In Fig. 2, we present convergence of the energy and atomic forces for $h = 0.2$ Bohr as $\{L_1, L_2, L_3\}$ is increased from $\{12, 12, 12\}$ Bohr to $\{18, 18, 18\}$ Bohr, with the results obtained for $\{L_1, L_2, L_3\} = \{40, 40, 40\}$ Bohr used as reference. We observe exponential convergence of both the energy and the forces to well below accuracies desired in DFT calculations. In fact, even a domain size of $\{L_1, L_2, L_3\} = \{12, 12, 12\}$ is sufficient to obtain chemical accuracy in both energy and forces. The corresponding electron density contours for H_2O are plotted in Fig. 3. Overall, these results demonstrate the efficacy of SPARC's electrostatic formulation in minimizing the finite-domain effect for isolated clusters.

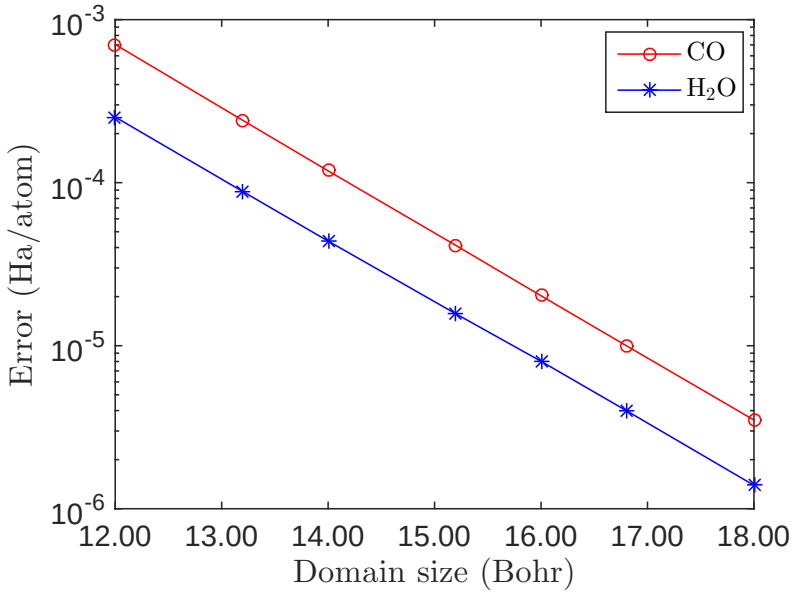

(a) Energy

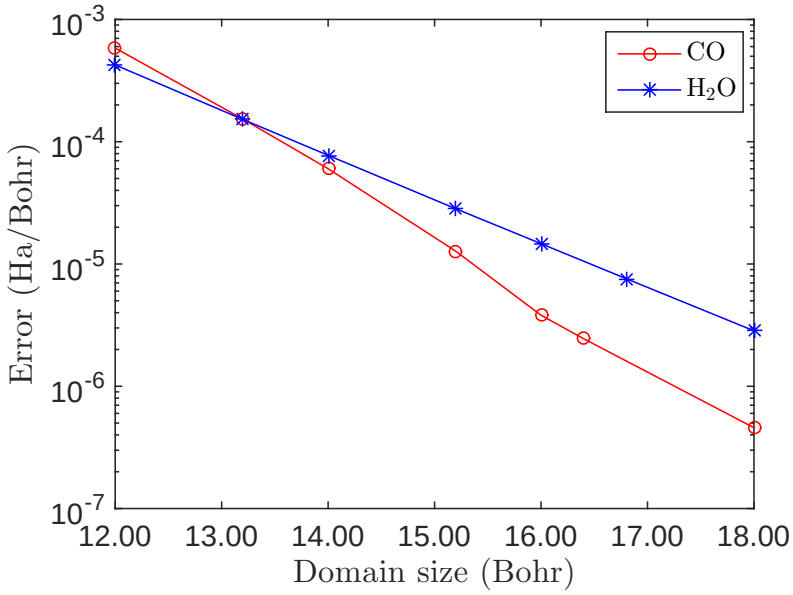

(b) Forces

Figure 2: Convergence of energy and atomic forces with respect to domain size for the CO and H_2O molecules.

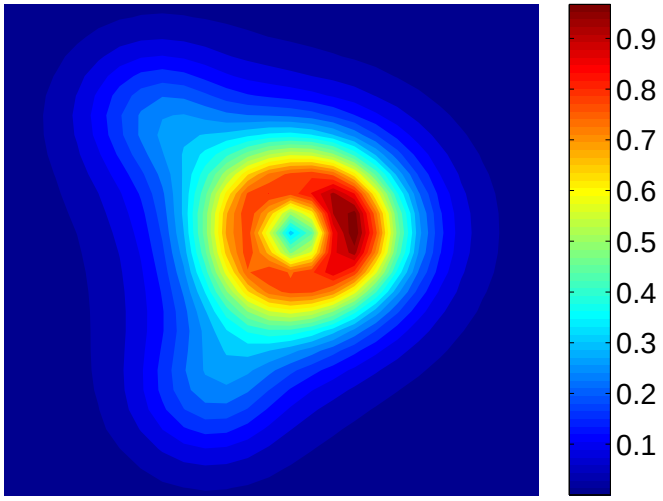

Figure 3: In-plane electron density contours for the H_2O molecule.

2.4.2 Convergence with spatial discretization

We next verify the convergence of the computed energy and atomic forces with respect to the finite-difference mesh-size. As representative examples, we choose the icosahedral Platinum (Pt_{13}), icosahedral Gold (Au_{13}), and β-Aminoisobutyric acid tri-TMS II ($C_{13}H_{33}NO_2Si_3$) clusters with domain sizes of $\{L_1, L_2, L_3\} = \{36, 36, 36\}$, $\{40, 40, 40\}$ and $\{42, 38, 34\}$ Bohr, respectively. All errors are defined with respect to ABINIT, wherein we employ plane-wave cutoffs of 42, 42, and 68 Ha along with domain sizes of $\{L_1, L_2, L_3\} = \{42, 42, 42\}$, $\{42, 42, 42\}$, and $\{50, 46, 42\}$ Bohr for Pt_{13}, Au_{13}, and $C_{13}H_{33}NO_2Si_3$, respectively. The resulting reference energies and forces are converged to within 5.0×10^{-6} Ha/atom and 5.0×10^{-6} Ha/Bohr, respectively. In Fig. 4, we plot error in the SPARC energy and forces with respect to the mesh size, from which it is clear that there is systematic convergence of both energies and forces. On performing a fit to the data, we obtain average convergence rates of approximately $\mathcal{O}(h^9)$ in the energy and $\mathcal{O}(h^8)$ in the forces. In doing so, the chemical accuracy desired in density functional theory calculations is readily attained. In Fig. 5, we present the computed isosurfaces for Au_{13} and $C_{13}H_{33}NO_2Si_3$.

Overall, we conclude that SPARC is able to obtain high convergence rates in both the DFT energy and atomic forces, which contributes to its accuracy and efficiency. Moreover, the energy and forces converge at comparable rates, without need of additional measures such as double-grid [79] or high-order integration [13] techniques.

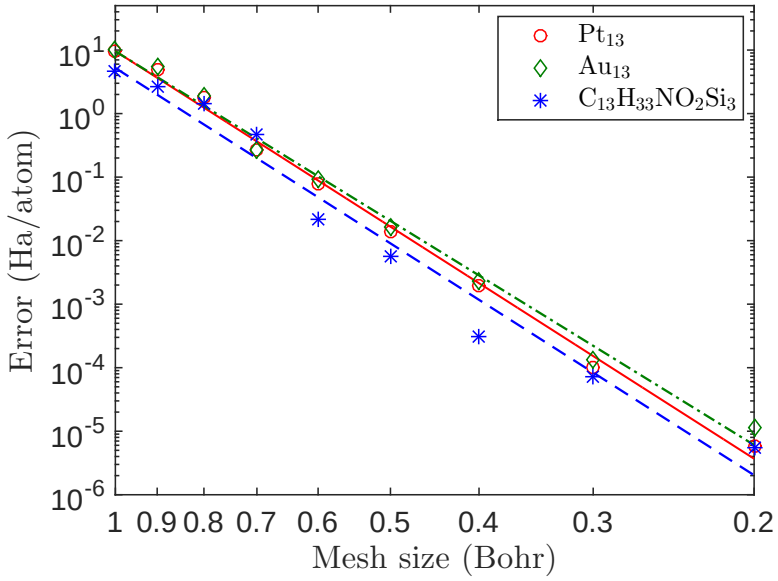

(a) Energy

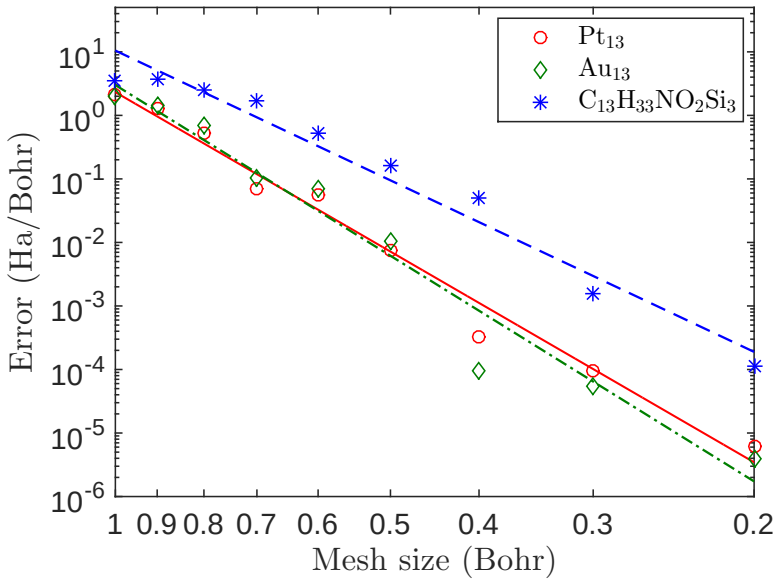

(b) Forces

Figure 4: Convergence of the energy and atomic forces with respect to mesh size to reference planewave result for the Pt_{13}, Au_{13}, and $C_{13}H_{33}NO_2Si_3$ clusters.

(a) Au_{13}

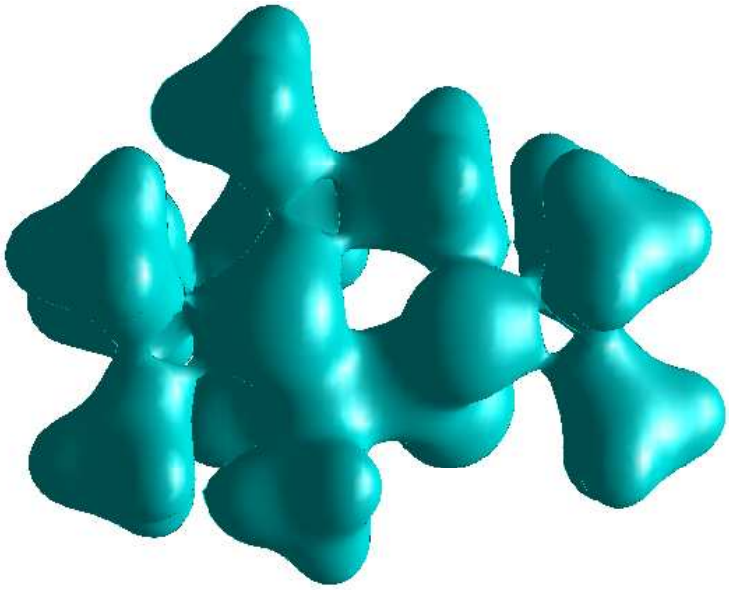

(b) $C_{13}H_{33}NO_2Si_3$

Figure 5: Electron density isosurface for $\rho = 0.05$ Bohr^{-3}

2.4.3 Ground state properties

We now verify that the ground-state properties of isolated clusters can be accurately determined using SPARC. For this purpose, we select the Hydrogen (H_2), Nitrogen (N_2), and Oxygen (O_2) molecules, a domain size of $\{L_1, L_2, L_3\} = \{24, 24, 24\}$ Bohr, and mesh-size of $h = 0.2$ Bohr. We begin by evaluating the energy and force as a function of interatomic distance, the results of which are presented in Fig. 6. Specifically, we plot the energy as a

function of bond length along with its cubic spline fit in Fig. 6a, and the computed interatomic force and the derivative of the cubic spline fit to the energy in Fig. 6b. The evident agreement demonstrates that the computed energy and atomic forces are indeed consistent. Moreover, there is no noticeable ‘egg-box’ effect [17]—a phenomenon arising due to the breaking of the translational symmetry—at meshes required for obtaining chemical accuracies.

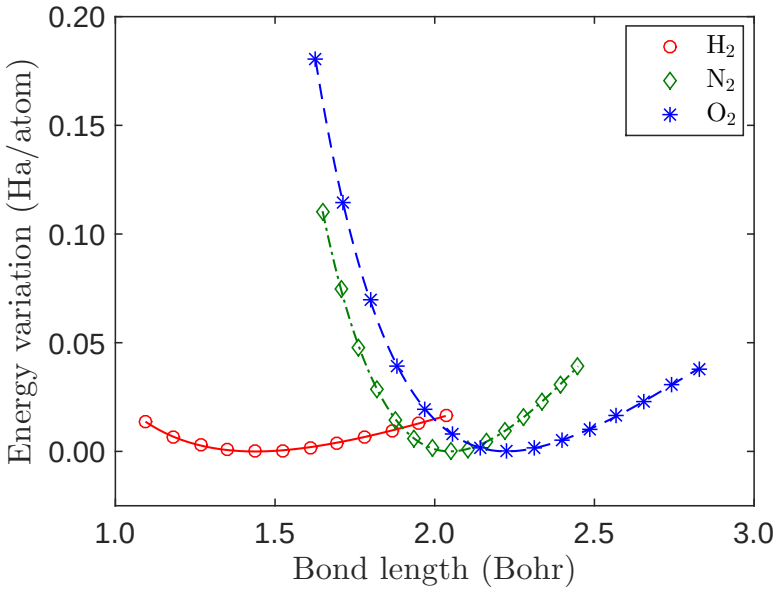

(a) Computed energy and its cubic spline fit

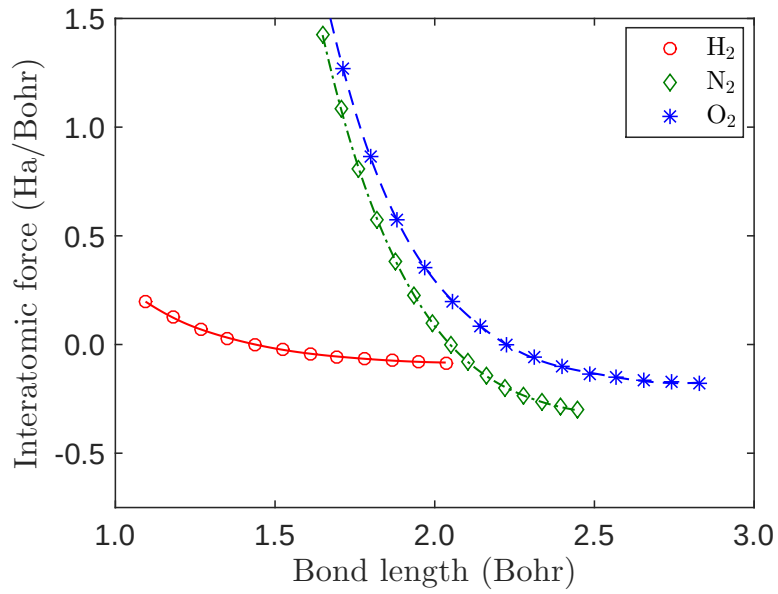

(b) Computed force and the derivative of the cubic spline fit to the energy

Figure 6: Variation in the computed energy and atomic force as a function of interatomic distance for the H_2, N_2, and O_2 molecules.

Next, we use the above results to calculate the vibrational frequency for the H_2, N_2, and

O_2 molecules using the relation [76]:

$$\nu = \frac{1}{2\pi c}\left(\frac{k}{\mu}\right)^{\frac{1}{2}}, \tag{45}$$

where c is the speed of light, k is the derivative of the cubic spline fit to the force at the equilibrium bond length, and μ is the reduced mass of the system. In ABINIT, we choose a domain size of $\{L_1, L_2, L_3\} = \{30, 30, 30\}$ Bohr for all three systems and planewave cutoffs of 32 Ha, 40 Ha, and 38 Ha for H_2, N_2, and O_2, respectively. From the results presented in Table 1, we observe that there is excellent agreement between SPARC and ABINIT, with the maximum difference in the vibrational frequency being $8\ cm^{-1}$. There is also good agreement between DFT and experiment, highlighting the accuracy of DFT as an ab-initio theory. These results further verify that SPARC is able to obtain accurate atomic forces, a critical feature for both structural relaxations and ab-initio molecular dynamics.

Table 1: Vibrational frequency in cm^{-1} for the H_2, N_2, and O_2 molecules.

Molecule	SPARC	ABINIT	Experiment [53, 11]
H_2	4007	4014	4401
N_2	2448	2456	2358
O_2	1649	1642	1580

Finally, we randomly perturb the atomic positions in the three molecules such that the interatomic distance differs by up to 15 percent from the equilibrium bond length. We maximize generality by ensuring that the resulting systems are not aligned with any of the coordinate axes. In Table 2, we present the results of the geometry optimization by SPARC, and compare them with ABINIT for the aforementioned choice of parameters. We observe that there is very good agreement between SPARC and ABINIT, with the maximum difference in the energy being 0.0007 Ha/atom, and the maximum difference in the equilibrium bond length being 0.001 Bohr. These results are also in excellent agreement with the data plotted in Fig. 6. Overall the results indicate that SPARC is able to accurately determine ground state properties for isolated clusters.

Table 2: Ground state energy and equilibrium configuration for the H_2, N_2, and O_2 molecules.

Molecule	Energy (Ha/atom)		Bond length (Bohr)	
	SPARC	ABINIT	SPARC	ABINIT
H_2	-0.5682	-0.5681	1.437	1.437
N_2	-9.9463	-9.9460	2.049	2.049
O_2	-15.8717	-15.8710	2.226	2.227

2.4.4 Scaling and performance

In previous subsections, we have verified the accuracy of SPARC by comparing with the well-established plane-wave code ABINIT. We now investigate the efficiency of SPARC relative to ABINIT, for which we choose bulk-terminated Silicon nanoclusters passivated by Hydrogen as representative examples. In all the calculations, we utilize a mesh-size of $h = 0.5$ Bohr in SPARC, and a planewave energy cutoff of 16 Ha in ABINIT. Further, we employ a vacuum of 5 Bohr in both SPARC and ABINIT. We choose all the other parameters so as to obtain the chemical accuracy of 0.001 Ha/atom in the energy and 0.001 Ha/Bohr in the atomic force. All the times reported here include the calculation of the electronic ground-state as well as the atomic force.

First, we compare the strong scaling of SPARC with ABINIT for the $Si_{275}H_{172}$ cluster. We utilize 2, 8, 64, 128, 512, and 640 cores for performing the simulation using SPARC. We use 6, 9, 37, 296, 592, and 666 cores for ABINIT, which it suggests are optimal in the range of cores considered here. In Fig. 7a, we present the wall time for an electronic ground-state calculation (19 SCF iterations), taken by SPARC and ABINIT as the number of processors is increased. We observe that both SPARC and ABINIT display similar trends with respect to strong scaling. Specifically, the SPARC and ABINIT curves are close to being parallel, with no further reduction in wall time observed after approximately 700 cores for SPARC and 600 cores for ABINIT. However, the prefactors are significantly different, with SPARC being able to outperform ABINIT by up to factors of 6.8.

Next, we compare the weak scaling of SPARC with ABINIT for the $Si_{29}H_{36}$, $Si_{71}H_{84}$,

$Si_{275}H_{172}$, $Si_{525}H_{276}$, and $Si_{849}H_{372}$ nanoclusters. The number of electrons in these systems range from 152 ($Si_{29}H_{36}$) to 3768 ($Si_{849}H_{372}$). For both SPARC and ABINIT, we fix the number of electrons per core to be approximately 160, and select at most 4 cores from every compute node. In Figure 7b, we present the results so obtained for the variation in total CPU time versus the number of electrons. We observe similar scaling for both codes, with $\mathcal{O}(N_e^{2.51})$ for SPARC and $\mathcal{O}(N_e^{2.75})$ for ABINIT. However, the prefactor for SPARC is again noticeably lower, with speedups over ABINIT ranging from factors of 3 to 7.

We observe that for our calculations, Chebyshev filtering is the predominant part, consuming 70 to 80 percent of the total wall time. The subspace projection step takes 6 to 19 percent and the subspace rotation step takes 1.16 to 9.5 percent of the total wall time. The fraction of total wall time increases with system size for these two methods. The percentage of total wall time taken by Poisson solution decreases from 6.6 percent for $Si_{29}H_{36}$ cluster to 0.5 percent for $Si_{849}H_{372}$ cluster. The fraction of time taken by atomic force calculation step decreases from 1.3 percent to 0.16 percent as the system size increases from $Si_{29}H_{36}$ to $Si_{849}H_{372}$ cluster. The parts of the calculation not involving the application of the Hamiltonian operator (initialization, pseudocharge calculation, eigenproblem solution, subspace rotation and atomic force calculation) takes less than 10 percent of the total wall time.

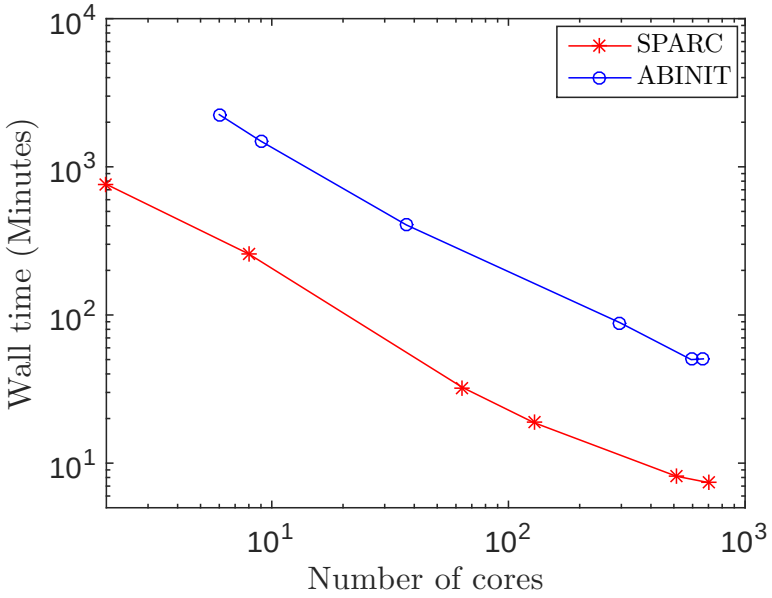

(a) Strong scaling

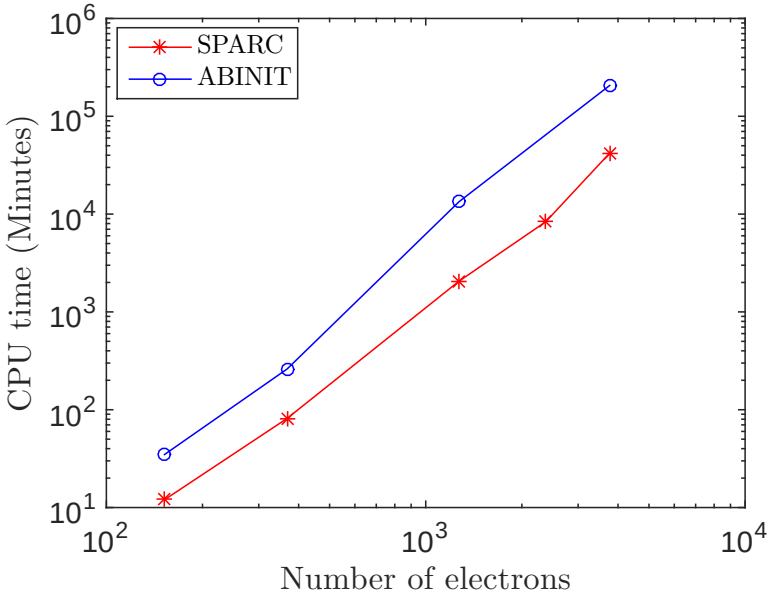

(b) Weak scaling

Figure 7: Strong and weak scaling behavior for hydrogen passivated silicon nanoclusters. The system utilized for strong scaling is $Si_{275}H_{172}$. The systems employed for weak scaling are $Si_{29}H_{36}$, $Si_{71}H_{84}$, $Si_{275}H_{172}$, $Si_{525}H_{276}$ and $Si_{849}H_{372}$.

Finally, we compare the minimum wall time achievable by SPARC and ABINIT for the aforementioned nanoclusters with the exception of $Si_{849}H_{372}$, for which the resources currently available to us are insufficient. While performing this study, we restrict the maximum number of electrons per computational core to 160. In SPARC, we choose the number of cores as multiples of 64, whereas we select the number of cores and parallelization scheme in ABINIT as suggested by it. We present the results so obtained in Table 4. We observe that SPARC is able to achieve smaller wall times by factors larger than 6.8 compared to ABINIT for all the systems considered. In particular, SPARC requires a factor of approximately 7.0 less wall time than ABINIT for the $Si_{525}H_{276}$ nanocluster. Overall, these results indicate that SPARC is a highly efficient DFT formulation and implementation that is highly competitive with well-optimized plane-wave codes.

Table 3: Minimum wall time in minutes for hydrogen passivated silicon nanoclusters. The number in brackets represents the number of cores on which the minimum wall time is achieved.

System	SPARC	ABINIT
$Si_{29}H_{36}$	0.69 (128)	7.3 (106)
$Si_{71}H_{84}$	1.15 (320)	8.10 (321)
$Si_{275}H_{172}$	7.39 (704)	50.6 (666)
$Si_{525}H_{276}$	32.45 (960)	227.56 (1008)

CHAPTER III

PERIODIC SYSTEMS

3.1 Mathematical background

Consider a unit cell Ω with N atoms and a total of N_e valence electrons. Let the nuclei be positioned at $\mathbf{R} = \{\mathbf{R}_1, \mathbf{R}_2, \ldots, \mathbf{R}_N\}$ and possess valence charges $\{Z_1, Z_2, \ldots, Z_N\}$, respectively. Neglecting spin, the system's free energy in Density Functional Theory (DFT) [52, 62] can be written as

$$\mathcal{F}(\Psi, \mathbf{g}, \mathbf{R}) = T_s(\Psi, \mathbf{g}) + E_{xc}(\rho) + K(\Psi, \mathbf{g}, \mathbf{R}) + E_{el}(\rho, \mathbf{R}) - TS(\mathbf{g})\,, \tag{46}$$

where $\Psi = \{\psi_1, \psi_2, \ldots, \psi_{N_s}\}$ is the collection of orbitals with occupations $\mathbf{g} = \{g_1, g_2, \ldots, g_{N_s}\}$, ρ is the electron density, and T is the electronic temperature. The electron density itself can be expressed in terms of the orbitals and their occupations as

$$\rho(\mathbf{x}) = 2\sum_{n=1}^{N_s} \fint_{BZ} g_n(\mathbf{k}) |\psi_n(\mathbf{x}, \mathbf{k})|^2 \, \mathrm{d}\mathbf{k}\,, \tag{47}$$

where $\mathbf{k}$ denotes the Bloch wavevector, and $\fint_{BZ}$ signifies the volume average over the Brillouin zone. In Eqn. 46, the first term is the electronic kinetic energy, the second term is the exchange-correlation energy, the third term is the non-local pseudopotential energy, the fourth term is the total electrostatic energy, and the final term is the entropic contribution arising from the partial occupations of the orbitals.

Electronic kinetic energy In Kohn-Sham DFT, the kinetic energy of the non-interacting electrons takes the form

$$T_s(\Psi, \mathbf{g}) = -\sum_{n=1}^{N_s} \fint_{BZ} \int_{\Omega} g_n(\mathbf{k}) \psi_n^*(\mathbf{x}, \mathbf{k}) \nabla^2 \psi_n(\mathbf{x}, \mathbf{k}) \, \mathrm{d}\mathbf{x} \, \mathrm{d}\mathbf{k}\,. \tag{48}$$

where the superscript $*$ denotes the complex conjugate.

Exchange-correlation energy The exact form of the exchange-correlation energy is currently unknown. Therefore, a number of approximations have been developed, including the widely used Local Density Approximation (LDA) [62]:

$$E_{xc}(\rho) = \int_{\Omega} \varepsilon_{xc}(\rho(\mathbf{x}))\rho(\mathbf{x})\,\mathrm{d}\mathbf{x}\,, \tag{49}$$

where $\varepsilon_{xc}(\rho) = \varepsilon_x(\rho) + \varepsilon_c(\rho)$ is the sum of the exchange and correlation per particle of a uniform electron gas.

Non-local pseudopotential energy The non-local pseudopotential energy within the Kleinman-Bylander [59] representation takes the form

$$K(\Psi, \mathbf{g}, \mathbf{R}) = \\ 2\sum_{n=1}^{N_s} \fint_{BZ} g_n(\mathbf{k}) \sum_{J} \sum_{lm} \gamma_{Jl} \left| \sum_{J'} \int_{\Omega} \chi^*_{J'lm}(\mathbf{x}, \mathbf{R}_{J'}) e^{i\mathbf{k}.(\mathbf{R}_J - \mathbf{R}_{J'})} \psi_n(\mathbf{x}, \mathbf{k})\,\mathrm{d}\mathbf{x} \right|^2 \mathrm{d}\mathbf{k}\,, \tag{50}$$

where the summation index J runs over all atoms in Ω, and the summation index J' runs over the J^{th} atom and its periodic images. In addition, the coefficients γ_{Jl} and projection functions χ_{Jlm} can be expressed as

$$\gamma_{Jl} = \left(\int_{\mathbb{R}^3} \chi^*_{Jlm}(\mathbf{x}, \mathbf{R}_J) u_{Jlm}(\mathbf{x}, \mathbf{R}_J)\,\mathrm{d}\mathbf{x} \right)^{-1}, \tag{51}$$

$$\chi_{J'lm}(\mathbf{x}, \mathbf{R}_{J'}) = u_{J'lm}(\mathbf{x}, \mathbf{R}_{J'}) \left(V_{J'l}(\mathbf{x}, \mathbf{R}_{J'}) - V_{J'}(\mathbf{x}, \mathbf{R}_{J'}) \right). \tag{52}$$

Above, $u_{J'lm}$ are the isolated atom pseudowavefunctions, $V_{J'l}$ are the angular momentum dependent pseudopotentials, and $V_{J'}$ are the local components of the pseudopotentials, with l and m signifying the azimuthal and magnetic quantum numbers, respectively.

Electrostatic energy The total electrostatic energy is the sum of three components:

$$E_{el}(\rho, \mathbf{R}) = \frac{1}{2} \int_{\mathbb{R}^3} \int_{\Omega} \frac{\rho(\mathbf{x})\rho(\mathbf{x}')}{|\mathbf{x} - \mathbf{x}'|}\,\mathrm{d}\mathbf{x}\,\mathrm{d}\mathbf{x}' + \sum_{I} \int_{\Omega} \rho(\mathbf{x}) V_I(\mathbf{x}, \mathbf{R}_I)\,\mathrm{d}\mathbf{x} + \frac{1}{2} \sum_{I} \sum_{J \neq I} \frac{Z_I Z_J}{|\mathbf{R}_I - \mathbf{R}_J|}\,, \tag{53}$$

where the first term—referred to as the Hartree energy—is the classical interaction energy of the electron density, the second term is the interaction energy between the electron density and the nuclei, and the third term is the repulsion energy between the nuclei. The summation index I runs over all atoms in $\mathbb{R}^3$, i.e., all the atoms in Ω and their periodic images.

Electronic entropy The electronic entropy originating from the partial orbital occupations:

$$S(\mathbf{g}) = -2k_B \sum_{n=1}^{N_s} \fint_{BZ} \left(g_n(\mathbf{k}) \log g_n(\mathbf{k}) + (1 - g_n(\mathbf{k})) \log(1 - g_n(\mathbf{k}))\right) \, \mathrm{d}\mathbf{k} \,, \tag{54}$$

where k_B is the Boltzmann constant.

Ground state The overall ground state in DFT is governed by the variational problem

$$\mathcal{F}_0 = \inf_{\mathbf{R}} \hat{\mathcal{F}}(\mathbf{R}) \,, \tag{55}$$

where

$$\hat{\mathcal{F}}(\mathbf{R}) = \inf_{\Psi, \mathbf{g}} \mathcal{F}(\Psi, \mathbf{g}, \mathbf{R}) \quad s.t. \quad \int_\Omega \psi_i^*(\mathbf{x}, \mathbf{k}) \psi_j(\mathbf{x}, \mathbf{k}) \, \mathrm{d}\mathbf{x} = \delta_{ij} \,, \quad 2 \sum_{n=1}^{N_s} \fint_{BZ} g_n(\mathbf{k}) \, \mathrm{d}\mathbf{k} = N_e \,. \tag{56}$$

In this staggered approach, the electronic ground-state as described by the above equation needs to be computed for every configuration of the nuclei encountered during the geometry optimization represented by Eqn. 55.

3.2 Real-space formulation

In this section, we describe the real-space formulation and parallel finite-difference implementation of Density Functional Theory (DFT) for periodic systems.

Electrostatic reformulation The non-locality of the electrostatic energy in Eqn. 53 makes its direct real-space evaluation scale as $\mathcal{O}(N^2)$ with respect to the number of atoms.

Furthermore, the individual components diverge in periodic systems. To overcome this, we adopt a local formulation of the electrostatics [83, 36]:

$$E_{el}(\rho,\mathbf{R}) = \sup_{\phi}\left\{ -\frac{1}{8\pi}\int_{\Omega}|\nabla\phi(\mathbf{x},\mathbf{R})|^2\,\mathrm{d}\mathbf{x} + \int_{\Omega}(\rho(\mathbf{x})+b(\mathbf{x},\mathbf{R}))\phi(\mathbf{x},\mathbf{R})\,\mathrm{d}\mathbf{x}\right\} \\ -E_{self}(\mathbf{R}) + E_c(\mathbf{R})\,, \tag{57}$$

where ϕ denotes the electrostatic potential. In addition, b represents the total pseudocharge density of the nuclei:

$$b(\mathbf{x},\mathbf{R}) = \sum_I b_I(\mathbf{x},\mathbf{R}_I)\,, \qquad b_I(\mathbf{x},\mathbf{R}_I) = -\frac{1}{4\pi}\nabla^2 V_I(\mathbf{x},\mathbf{R}_I)\,, \tag{58}$$

$$\int_{\Omega} b(\mathbf{x},\mathbf{R})\,\mathrm{d}\mathbf{x} = -N_e\,, \qquad \int_{\mathbb{R}^3} b_I(\mathbf{x},\mathbf{R}_I)\,\mathrm{d}\mathbf{x} = Z_I\,, \tag{59}$$

where the summation index I runs over all atoms in $\mathbb{R}^3$, and b_I is the pseudocharge density of the I^{th} nucleus that generates the potential V_I. The second to last term in Eqn. 57 represents the self energy associated with the pseudocharge densities:

$$E_{self}(\mathbf{R}) = \frac{1}{2}\sum_I \int_{\Omega} b_I(\mathbf{x},\mathbf{R}_I)V_I(\mathbf{x},\mathbf{R}_I)\,\mathrm{d}\mathbf{x}\,. \tag{60}$$

The last term E_c, whose explicit expression can be found in Appendix A, corrects for the error in the repulsive energy when the pseudocharge densities overlap.

Electronic ground-state The electronic ground-state for a given position of nuclei is governed by the constrained minimization problem in Eqn. 56. On taking the first variation and utilizing Bloch's theorem [12]:

$$\psi_n(\mathbf{x},\mathbf{k}) = e^{i\mathbf{k}.\mathbf{x}}u_n(\mathbf{x},\mathbf{k})\,, \tag{61}$$

we arrive at

$$\left(\mathcal{H} \equiv -\frac{1}{2}\nabla^2 - i\mathbf{k}.\nabla + \frac{1}{2}|\mathbf{k}|^2 + V_{xc} + \phi + e^{-i\mathbf{k}.\mathbf{x}}V_{nl}e^{i\mathbf{k}.\mathbf{x}}\right)u_n = \lambda_n u_n\,, \quad n = 1,2,\ldots,N_s\,, \\ g_n(\mathbf{k}) = \left(1+\exp\left(\frac{\lambda_n(\mathbf{k})-\lambda_f}{k_BT}\right)\right)^{-1}\,, \quad \text{where } \lambda_f \text{ is } s.t.\ 2\sum_{n=1}^{N_s}\fint_{BZ} g_n(\mathbf{k})\,\mathrm{d}\mathbf{k} = N_e\,, \\ \rho(\mathbf{x}) = 2\sum_{n=1}^{N_s}\fint_{BZ} g_n(\mathbf{k})|u_n(\mathbf{x},\mathbf{k})|^2\,\mathrm{d}\mathbf{k}\,, \quad -\frac{1}{4\pi}\nabla^2\phi(\mathbf{x},\mathbf{R}) = \rho(\mathbf{x}) + b(\mathbf{x},\mathbf{R})\,, \tag{62}$$

where $i = \sqrt{-1}$, u is a function that is periodic on the unit cell, $\mathcal{H}$ is the Hamiltonian operator, $V_{xc} = \delta E_{xc}/\delta\rho$ is the exchange-correlation potential, λ_f is the Fermi energy, and V_{nl} is the non-local pseudopotential operator:

$$\begin{aligned} V_{nl}f &= \sum_J V_{nl,J}f = \sum_J \sum_{lm} \gamma_{Jl} \left(\sum_{J'} e^{-i\mathbf{k}.(\mathbf{R}_J - \mathbf{R}_{J'})} \chi_{J'lm} \right) \\ &\quad \times \left(\sum_{J'} \int_\Omega \chi^*_{J'lm}(\mathbf{x}, \mathbf{R}_{J'}) e^{i\mathbf{k}.(\mathbf{R}_J - \mathbf{R}_{J'})} f(\mathbf{x})\, \mathrm{d}\mathbf{x} \right) . \end{aligned} \tag{63}$$

Above, the summation index J runs over all atoms in Ω, and the summation index J' runs over the J^{th} atom and its periodic images.

The electronic ground-state is determined by solving the non-linear eigenvalue problem in Eqn. 62 using the Self-Consistent Field (SCF) method [97]. Specifically, a fixed-point iteration is performed with respect to the potential $V_{eff} = V_{xc} + \phi$, which is further accelerated using mixing/extrapolation schemes [28, 69, 89, 9]. In each iteration of the SCF method, the electrostatic potential is calculated by solving the Poisson equation, and the electron density is determined by computing the eigenfunctions of the linearized Hamiltonian. The orthogonality requirement amongst the Kohn-Sham orbitals makes such a procedure scale asymptotically as $\mathcal{O}(N^3)$ with respect to the number of atoms, which severely limits the size of systems that can be studied. To overcome this restrictive scaling, $\mathcal{O}(N)$ approaches [41, 16] will be subsequently developed and implemented into SPARC.

Free energy The free energy is evaluated using the Harris-Foulkes [48, 33] type functional:

$$\begin{aligned} \hat{\mathcal{F}}(\mathbf{R}) &= 2\sum_{n=1}^{N_s} \fint_{BZ} g_n(\mathbf{k})\lambda_n(\mathbf{k})\, \mathrm{d}\mathbf{k} + \int_\Omega \varepsilon_{xc}(\rho(\mathbf{x}))\rho(\mathbf{x})\, \mathrm{d}\mathbf{x} - \int_\Omega V_{xc}(\rho(\mathbf{x}))\rho(\mathbf{x})\, \mathrm{d}\mathbf{x} \\ &+ \frac{1}{2}\int_\Omega (b(\mathbf{x}, \mathbf{R}) - \rho(\mathbf{x}))\phi(\mathbf{x}, \mathbf{R})\, \mathrm{d}\mathbf{x} - E_{self}(\mathbf{R}) + E_c(\mathbf{R}) \\ &+ 2k_B T \sum_{n=1}^{N_s} \fint_{BZ} (g_n(\mathbf{k}) \log g_n(\mathbf{k}) + (1 - g_n(\mathbf{k})) \log(1 - g_n(\mathbf{k})))\, \mathrm{d}\mathbf{k}\,, \end{aligned} \tag{64}$$

where E_{self} and E_c are as defined in Eqns. 60 and 97, respectively.

Atomic forces Once the electronic ground-state has been determined, the atomic forces are calculated using the relation:

$$\begin{aligned}
\mathbf{f}_J &= -\frac{\partial \hat{\mathcal{F}}(\mathbf{R})}{\partial \mathbf{R}_J} \\
&= \sum_{J'} \int_{\Omega} \nabla b_{J'}(\mathbf{x}, \mathbf{R}_{J'}) \left(\phi(\mathbf{x}, \mathbf{R}) - V_{J'}(\mathbf{x}, \mathbf{R}_{J'})\right) \, \mathrm{d}\mathbf{x} + \mathbf{f}_{J,c}(\mathbf{R}) \qquad (65) \\
&- 4 \sum_{n=1}^{N_s} \fint_{BZ} g_n(\mathbf{k}) \sum_{lm} \gamma_{Jl} \Re \left[\left(\sum_{J'} \int_{\Omega} \psi_n^*(\mathbf{x}, \mathbf{k}) e^{-i\mathbf{k}.(\mathbf{R}_J - \mathbf{R}_{J'})} \chi_{J'lm}(\mathbf{x}, \mathbf{R}_{J'}) \, \mathrm{d}\mathbf{x} \right) \right. \\
&\left. \times \left(\sum_{J'} \int_{\Omega} \nabla \psi_n(\mathbf{x}, \mathbf{k}) e^{i\mathbf{k}.(\mathbf{R}_J - \mathbf{R}_{J'})} \chi^*_{J'lm}(\mathbf{x}, \mathbf{R}_{J'}) \, \mathrm{d}\mathbf{x} \right) \right] \, \mathrm{d}\mathbf{k} \, ,
\end{aligned}$$

where the summation index J' runs over the J^{th} atom and its periodic images, and $\Re[.]$ denotes the real part of the bracketed expression. The first term is the local component of the force [99], the second term corrects for overlapping pseudocharge densities [101] (Appendix A), and the final term is the non-local component obtained by transferring the derivative on the projectors (with respect to the atomic position) to the orbitals (with respect to space) [50]. This strategy is employed since the orbitals are generally much smoother than the projectors, and therefore more accurate forces can be obtained for a given discretization [90].

Overview of SPARC The approach adopted for determining the ground-state is outlined in Fig. 8, whose key components are discussed in detail in the subsections below.

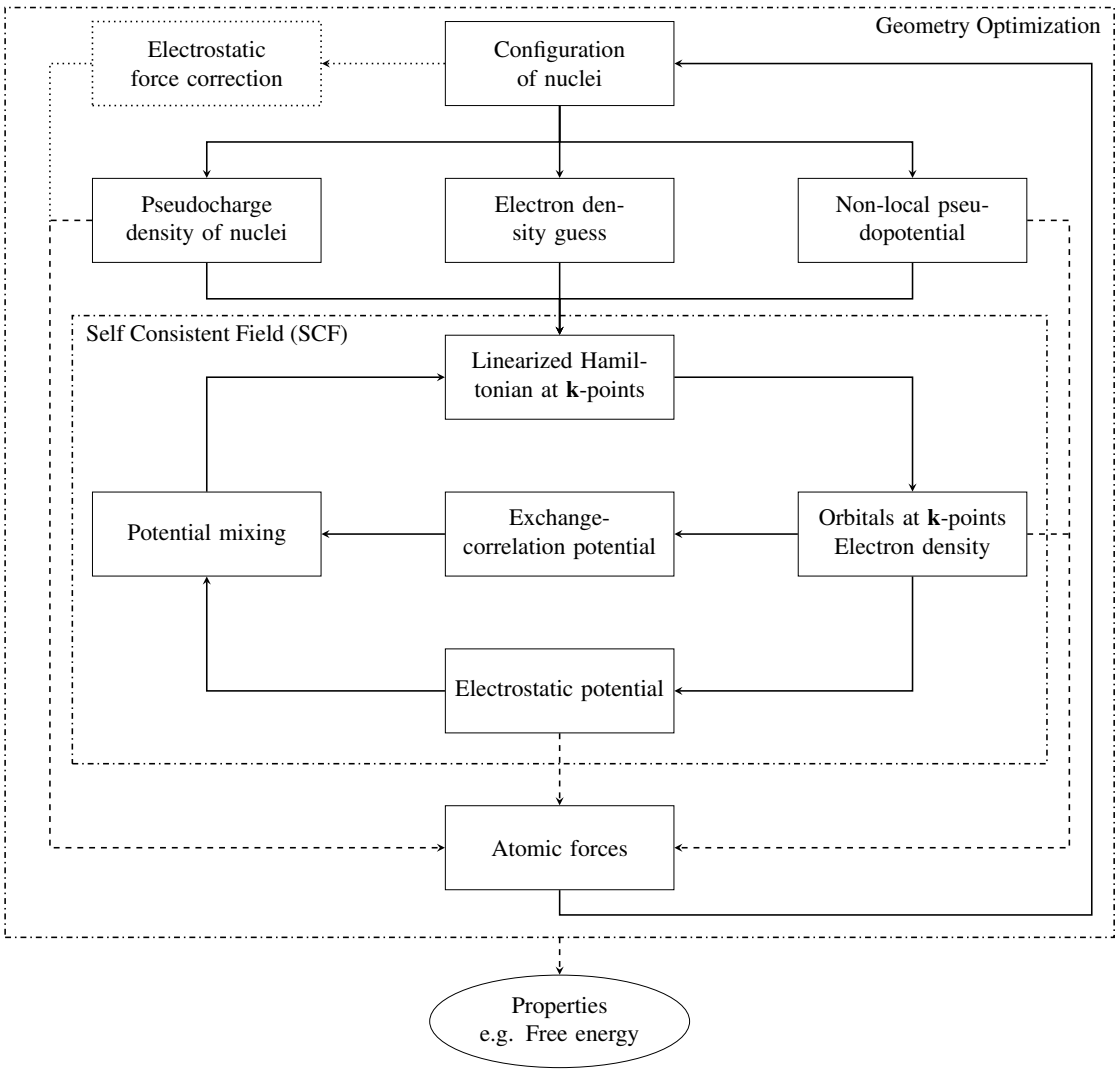

Figure 8: Outline of ground-state DFT simulations in SPARC for periodic systems.

3.3 Finite-difference implementation

We discretize the unit cell Ω—cuboidal in shape with sides of length L_1, L_2 and L_3—using a non uniform finite-difference grid with spacings h_1, h_2, h_3 such that $L_1 = n_1 h_1$, $L_2 = n_2 h_2$ and $L_3 = n_3 h_3$ ($n_1, n_2, n_3 \in \mathbb{N}$, $\mathbb{N}$: set of all natural numbers). We designate each finite-difference node using an index of the form (i, j, k), where $i = 1, 2, \ldots, n_1$, $j = 1, 2, \ldots, n_2$ and $k = 1, 2, \ldots, n_3$. We approximate the Laplacian using the central

finite-difference approximation:

$$\begin{aligned}\nabla_h^2 f\Big|^{(i,j,k)} &\approx \sum_{p=0}^{n_o}\Big(w_{p,1}(f^{(i+p,j,k)}+f^{(i-p,j,k)})+w_{p,2}(f^{(i,j+p,k)}+f^{(i,j-p,k)})\\ &+ w_{p,3}(f^{(i,j,k+p)}+f^{(i,j,k-p)})\Big), \end{aligned} \tag{66}$$

where $f^{(i,j,k)}$ represents the value of the function f at (i,j,k), and the weights [74, 36]

$$\begin{aligned} w_{0,s} &= -\frac{1}{h_s^2}\sum_{q=1}^{n_o}\frac{1}{q^2}\,,\ s=1,2,3,\\ w_{p,s} &= \frac{2(-1)^{p+1}}{h_s^2 p^2}\frac{(n_o!)^2}{(n_o-p)!(n_o+p)!}\,,\ p=1,2,\ldots,n_o\,,\ s=1,2,3. \end{aligned} \tag{67}$$

Similarly, we approximate the gradient operator using central finite-differences:

$$\begin{aligned}\nabla_h f\Big|^{(i,j,k)} &\approx \sum_{p=1}^{n_o}\Big(\tilde{w}_{p,1}(f^{(i+p,j,k)}-f^{(i-p,j,k)})\hat{\mathbf{e}}_1+\tilde{w}_{p,2}(f^{(i,j+p,k)}-f^{(i,j-p,k)})\hat{\mathbf{e}}_2\\ &+ \tilde{w}_{p,3}(f^{(i,j,k+p)}-f^{(i,j,k-p)})\hat{\mathbf{e}}_3\Big), \end{aligned} \tag{68}$$

where $\hat{\mathbf{e}}_1$, $\hat{\mathbf{e}}_2$ and $\hat{\mathbf{e}}_3$ represent unit vectors along the edges of Ω, and the weights [74, 36]

$$\tilde{w}_{p,s} = \frac{(-1)^{p+1}}{h_s p}\frac{(n_o!)^2}{(n_o-p)!(n_o+p)!}\,,\ p=1,2,\ldots,n_o\,,\ s=1,2,3. \tag{69}$$

We employ the trapezoidal rule for performing spatial integrations, i.e.,

$$\int_\Omega f(\mathbf{x})\,\mathrm{d}\mathbf{x} \approx h_1h_2h_3\sum_{i=1}^{n_1}\sum_{j=1}^{n_2}\sum_{k=1}^{n_3} f^{(i,j,k)}\,, \tag{70}$$

using which we approximate the nonlocal pseudopotential operator as

$$\begin{aligned} V_{nl}f\Big|^{(i,j,k)} &= \sum_J V_{nl,J}f\Big|^{(i,j,k)}\\ &\approx h_1h_2h_3\sum_J\sum_{lm}\sum_{p=1}^{n_1}\sum_{q=1}^{n_2}\sum_{r=1}^{n_3}\gamma_{Jl}\left(\sum_{J'}e^{-i\mathbf{k}.(\mathbf{R}_J-\mathbf{R}_{J'})}\chi_{J'lm}^{(i,j,k)}\right)\\ &\quad\times\left(\sum_{J'}e^{i\mathbf{k}.(\mathbf{R}_J-\mathbf{R}_{J'})}\chi_{J'lm}^{*(p,q,r)}f^{(p,q,r)}\right), \end{aligned} \tag{71}$$

where the summation index J runs over all atoms in Ω, and the summation index J' runs over the J^{th} atom and its periodic images. We enforce periodic boundary conditions on Ω

by mapping any index that does not correspond to a node in the finite-difference grid to its periodic image within Ω.

Henceforth, we denote the discrete Hamiltonian matrix as a function of the Bloch wavevector $\mathbf{k}$ by $\mathbf{H}(\mathbf{k}) \in \mathbb{C}^{N_d \times N_d}$, where $N_d = n_1 \times n_2 \times n_3$ is the total number of finite-difference nodes. In addition, we represent the eigenvalues of $\mathbf{H}(\mathbf{k})$ arranged in ascending order by $\lambda_1(\mathbf{k}), \lambda_2(\mathbf{k}), \ldots, \lambda_{N_d}(\mathbf{k})$. We store $\mathbf{H}(\mathbf{k})$ and other sparse matrices in compressed row format, and store the discrete cell periodic part of the orbitals as columns of the dense matrix $\mathbf{U}(\mathbf{k}) \in \mathbb{C}^{N_d \times N_s}$. In parallel computations, we partition the domain as $\Omega = \bigcup_{p=1}^{n_p} \Omega_p$, where Ω_p denotes the domain local to the p^{th} processor, and n_p is the total number of processors. The specific choice of Ω_p corresponds to the PETSc default for structured grids.

3.3.1 Pseudocharge density generation and self energy calculation

In each structural relaxation step, the finite-difference Laplacian is used to assign the pseudocharge densities to the grid [99]:

$$b^{(i,j,k)} = \sum_I b_I^{(i,j,k)}, \quad b_I^{(i,j,k)} = -\frac{1}{4\pi} \nabla_h^2 V_I \big|^{(i,j,k)}, \tag{72}$$

where the summation index I runs over all atoms in $\mathbb{R}^3$. The discrete form of the pseudocharge density b_I has exponential decay away from $\mathbf{R}_I$, as demonstrated in Appendix B. This allows for its truncation at some suitably chosen radius r_I^b, without appreciable loss of accuracy. The corresponding discrete self energy takes the form

$$E_{self}^h = \frac{1}{2} h_1 h_2 h_3 \sum_I \sum_{i=1}^{n_1} \sum_{j=1}^{n_2} \sum_{k=1}^{n_3} b_I^{(i,j,k)} V_I^{(i,j,k)}. \tag{73}$$

In Algorithm 5, we outline the calculation of $b^{(i,j,k)}$ and E_{self}^h, as implemented in SPARC. For the J^{th} atom in Ω, we determine $\Omega_{r_{J'}^b} \cap \Omega_p$ (with s and e denoting the starting and ending indices) for atoms which have $\Omega_{r_{J'}^b} \cap \Omega \neq \emptyset$. Here, the index J' signifies the J^{th} atom and its periodic images. Further, $\Omega_{r_{J'}^b}$ denotes the cuboid with side of lengths

$2r^b_{1,J}$, $2r^b_{2,J}$ and $2r^b_{3,J}$ centered on the J'^{th} atom and Ω_p represents the domain local to the p^{th} processor. We have chosen $\Omega_{r^b_{J'}}$ to be a cuboid rather than a sphere due to its simplicity and efficiency within the Euclidean finite-difference discretization. The values of $r^b_{1,J}$, $r^b_{2,J}$ and $r^b_{3,J}$ are chosen such that the charge constraint in Eqn. 59 is satisfied to within a prespecified tolerance ε_b, i.e.

$$\left| h_1 h_2 h_3 \sum_{J'} \sum_{i=1}^{n_1} \sum_{j=1}^{n_2} \sum_{k=1}^{n_3} b^{(i,j,k)}_{J'} - Z_J \right| < \varepsilon_b \,, \tag{74}$$

where the summation index J' runs over the J^{th} atom and its periodic images. In the overlap region so established, we interpolate the values of $V^{(i,j,k)}_{J'}$ on to the finite-difference grid using cubic-splines [1]. Next, we determine $b^{(i,j,k)}$ and $E^{h,p}_{self}$—contribution of the p^{th} processor to the self energy—using Eqns. 72 and 73, respectively. Finally, we calculate the total self energy E^h_{self} by summing the contributions from all the processors.

Algorithm 5: Pseudocharge density generation and self energy calculation

Input: $\mathbf{R}$, V_J, and r^b_J

$b^{(i,j,k)} = 0$, $E^{h,p}_{self} = 0$

for $J = 1 \ldots N$ **do**

  for $J' = J^{th}$ *atom and its periodic images for which* $\Omega_{r^b_{J'}} \cap \Omega \neq \emptyset$ **do**

    Determine i_s, i_e, j_s, j_e, k_s, k_e of $\Omega_{r^b_{J'}} \cap \Omega_p$

    Determine $V^{(i,j,k)}_{J'}$ $\forall\, i \in [i_s - n_o, i_e + n_o]$, $j \in [j_s - n_o, j_e + n_o]$,

    $k \in [k_s - n_o, k_e + n_o]$

    $b^{(i,j,k)}_{J'} = -\frac{1}{4\pi} \nabla^2_h V_{J'}\big|^{(i,j,k)}$, $\quad b^{(i,j,k)} = b^{(i,j,k)} + b^{(i,j,k)}_{J'}$ $\forall\, i \in [i_s, i_e]$,

    $j \in [j_s, j_e]$, $k \in [k_s, k_e]$

    $E^{h,p}_{self} = E^{h,p}_{self} + \frac{1}{2} h_1 h_2 h_3 b^{(i,j,k)}_{J'} V^{(i,j,k)}_{J'}$ $\forall\, i \in [i_s, i_e]$, $j \in [j_s, j_e]$, $k \in [k_s, k_e]$

$E^h_{self} = \sum_{p=1}^{n_p} E^{h,p}_{self}$

Output: $b^{(i,j,k)}$ and E^h_{self}

3.3.2 Brillouin zone integration

The volume averaged integral of any function over the Brillouin zone is approximated as

$$⨍_{BZ} f(\mathbf{k})\,\mathrm{d}\mathbf{k} \approx \sum_{b=1}^{N_k} w_b f_b\,, \tag{75}$$

where $f_b \equiv f(\mathbf{k_b})$. Here, $\mathbf{k_b}$ and w_b ($b = 1, 2, \ldots N_k$) denote the nodes and weights for integration, respectively. The specific choice of $\mathbf{k_b}$ is commonly referred to as Brillouin zone sampling.

3.3.3 Electron density calculation

On employing the Brillouin zone integration scheme described by Eqn. 75, the electron density takes the form

$$\rho(\mathbf{x}) = 2\sum_{n=1}^{N_s}\sum_{b=1}^{N_k} w_b g_{nb}|u_{nb}(\mathbf{x})|^2\,. \tag{76}$$

In each SCF iteration, we calculate the electron density using the Chebyshev-filtered subspace iteration (CheFSI) method [110, 109], wherein we compute approximations to the eigenvectors corresponding to the lowest N_s eigenvalues of $\mathbf{H_b}$, $b = 1, 2, \ldots N_k$. This choice of eigensolver is motivated by the minimal orthogonalization and computer memory costs compared to other alternatives commonly employed in electronic structure calculations, e.g. Locally Optimal Block Preconditioned Conjugate Gradient (LOBPCG) [60].

The implementation of the CheFSI algorithm in SPARC consists of three main components. First, we use the rapid growth of Chebyshev polynomials outside the interval $[-1, 1]$ to filter out the unwanted eigencomponents from $\mathbf{U_b}$:

$$\mathbf{U_{bf}} = p_{mb}(\mathbf{H_b})\mathbf{U_b}\,, \quad p_{mb}(t) = C_m\left(\frac{t - c_b}{e_b}\right)\,, \quad b = 1, 2, \ldots, N_k\,, \tag{77}$$

where the columns of $\mathbf{U_{bf}}$ represent the filtered cell periodic part of the orbitals, and C_m denotes the Chebyshev polynomial of degree m. Additionally, $e_b = (\lambda_{N_d b} - \lambda_c)/2$ and $c_b = (\lambda_{N_d b} + \lambda_c)/2$, where λ_c is the filter cutoff. Rather than explicitly compute the matrix $p_{mb}(\mathbf{H_b})$, its product with $\mathbf{U_b}$ is determined using the three term recurrence relation for Chebyshev polynomials.

Next, projecting onto the filtered basis $\mathbf{U_{bf}}$, we arrive at the generalized eigenproblem:

$$\tilde{\mathbf{H}}_\mathbf{b}\mathbf{y_{nb}} = \lambda_{nb}\tilde{\mathbf{M}}_\mathbf{b}\mathbf{y_{nb}}\,, \quad n = 1, 2, \ldots N_s\,, \quad b = 1, 2, \ldots, N_k\,, \tag{78}$$

where λ_{nb} represent approximations to the eigenvalues of $\mathbf{H_b}$, and the dense matrices $\tilde{\mathbf{H}}_\mathbf{b}, \tilde{\mathbf{M}}_\mathbf{b} \in \mathbb{C}^{N_s \times N_s}$ are determined as

$$\tilde{\mathbf{H}}_\mathbf{b} = \mathbf{U}_\mathbf{bf}^{*\mathbf{T}}\mathbf{H}_\mathbf{b}\mathbf{U_{bf}}\,, \quad \tilde{\mathbf{M}}_\mathbf{b} = \mathbf{U}_\mathbf{bf}^{*\mathbf{T}}\mathbf{U_{bf}}\,. \tag{79}$$

After eigendecomposing Eqn. 78 at all the **k**-points, the Fermi energy λ_f is calculated by enforcing the constraint on the total number of electrons:

$$2\sum_{n=1}^{N_s}\sum_{b=1}^{N_k} w_b g_{nb} = N_e\,, \quad \text{where} \quad g_{nb} = \left(1 + \exp\left(\frac{\lambda_{nb} - \lambda_f}{k_B T}\right)\right)^{-1}\,. \tag{80}$$

Finally, we perform the subspace rotation

$$\mathbf{U_b} = \mathbf{U_{bf}}\mathbf{Y_b}\,, \quad b = 1, 2, \ldots, N_k\,, \tag{81}$$

where the columns of the matrix $\mathbf{Y_b} \in \mathbb{C}^{N_s \times N_s}$ contain the eigenvectors $\mathbf{y_{nb}}$. The columns of $\mathbf{U_b}$ so obtained represent approximations to the eigenvectors of $\mathbf{H_b}$. The electron density at the finite-difference grid points is then calculated using the relation

$$\rho^{(i,j,k)} = 2\sum_{n=1}^{N_s}\sum_{b=1}^{N_k} w_b g_{nb} |u_{nb}^{(i,j,k)}|^2\,, \tag{82}$$

where the values of $u_{nb}^{(i,j,k)}$ are extracted from the n^{th} column of $\mathbf{U_b}$.

We start the very first SCF iteration of the complete DFT simulation with a randomly generated guess for $\mathbf{U_b}$ ($b = 1, 2, \ldots, N_k$), and perform the CheFSI steps multiple times [111] without calculating/updating the electron density. This allows us to obtain a good approximation of the electron density for the second SCF iteration. For every subsequent SCF iteration, we perform the CheFSI steps only once, and use the rotated $\mathbf{U_b}$ from the previous step as the initial guess. Overall, the calculation of the electron density scales as $\mathcal{O}(N_k N_s N_d) + \mathcal{O}(N_k N_s^2 N_d) + \mathcal{O}(N_k N_s^3)$, which makes it $\mathcal{O}(N^3)$ with respect to the number of atoms.

3.3.4 Free energy calculation

On approximating the spatial and Brillouin zone integrals using Eqns. 70 and 75, respectively, we arrive at the discrete form for the free energy at the electronic ground-state:

$$\begin{aligned}\hat{\mathcal{F}}^h &= 2\sum_{n=1}^{N_s}\sum_{b=1}^{N_k} w_b g_{nb}\lambda_{nb} + h_1h_2h_3\sum_{i=1}^{n_1}\sum_{j=1}^{n_2}\sum_{k=1}^{n_3}\Bigg(\varepsilon_{xc}^{(i,j,k)}\rho^{(i,j,k)} - V_{xc}^{(i,j,k)}\rho^{(i,j,k)} \\ &+ \frac{1}{2}(b^{(i,j,k)} - \rho^{(i,j,k)})\phi^{(i,j,k)}\Bigg) - E_{self}^h + E_c^h \\ &+ 2k_BT\sum_{n=1}^{N_s}\sum_{b=1}^{N_k} w_b\left(g_{nb}\log g_{nb} + (1-g_{nb})\log(1-g_{nb})\right), \end{aligned} \tag{83}$$

where E_{self}^h is the discrete self energy (Eqn. 73), and E_c^h is the discrete repulsive energy correction for overlapping pseudocharges (Eqn. 101). The evaluation of $\hat{\mathcal{F}}^h$ scales as $\mathcal{O}(N_d)$, and therefore $\mathcal{O}(N)$ with respect to the number of atoms.

3.3.5 Atomic forces calculation

The discrete form of the atomic force presented in Eqn. 65 can be split into three parts:

$$\mathbf{f}_J^h = \mathbf{f}_{J,loc}^h + \mathbf{f}_{J,c}^h + \mathbf{f}_{J,nloc}^h\,, \tag{84}$$

where $\mathbf{f}_{J,loc}^h$ is the discrete local component, $\mathbf{f}_{J,c}^h$ is the discrete correction corresponding to overlapping pseudocharges, and $\mathbf{f}_{J,nloc}^h$ is the discrete non-local component of the force. Below, we discuss the evaluation of $\mathbf{f}_{J,loc}^h$ and $\mathbf{f}_{J,nloc}^h$ in SPARC, with the computation of $\mathbf{f}_{J,c}^h$ proceeding similarly to $\mathbf{f}_{J,loc}^h$.

Local component On approximating the spatial integral using Eqn. 70, the discrete local component of the force takes the form

$$\mathbf{f}_{J,loc}^h = h_1h_2h_3\sum_{J'}\sum_{i=1}^{n_1}\sum_{j=1}^{n_2}\sum_{k=1}^{n_3}\nabla_h b_{J'}\Big|^{(i,j,k)}(\phi^{(i,j,k)} - V_{J'}^{(i,j,k)})\,, \tag{85}$$

where the summation index J' runs over the J^{th} atom and its periodic images. The calculation of $\mathbf{f}_{J,loc}^h$ in SPARC is outlined in Algorithm 6, which proceeds as follows. For

the J^{th} atom in Ω, we determine $\Omega_{r^b_{J'}} \cap \Omega_p$ (with s and e denoting the starting and ending indices) for atoms which have $\Omega_{r^b_{J'}} \cap \Omega \neq \emptyset$. Here, the index J' signifies the J^{th} atom and its periodic images. In this overlap region, the values of $V_{J'}^{(i,j,k)}$ are interpolated on to the finite-difference grid using cubic-splines, from which $b_{J'}^{(i,j,k)}$ is calculated using Eqn. 72. Subsequently, $\mathbf{f}^{h,p}_{J,loc}$—contribution of the p^{th} processor to the local component of the force—is calculated using Eqn. 85. Finally, the contributions from all processors are summed to simultaneously obtain $\mathbf{f}^{h}_{J,loc}$ for all the atoms.

Algorithm 6: Calculation of the local component of the atomic force.

Input: $\mathbf{R}$, $\phi^{(i,j,k)}$, V_J, and r^b_J

for $J = 1 \ldots N$ **do**

$\mathbf{f}^{h,p}_{J,loc} = 0$

for $J' = J^{th}$ *atom and its periodic images for which* $\Omega_{r^b_{J'}} \cap \Omega \neq \emptyset$ **do**

Determine i_s, i_e, j_s, j_e, k_s, k_e of $\Omega_{r^b_{J'}} \cap \Omega_p$

Determine $V_{J'}^{(i,j,k)}$ $\forall\ i \in [i_s - n_o, i_e + n_o]$, $j \in [j_s - n_o, j_e + n_o]$, and

$k \in [k_s - n_o, k_e + n_o]$

$b_{J'}^{(i,j,k)} = -\frac{1}{4\pi}\nabla_h^2 V_{J'}\Big|^{(i,j,k)}$ $\forall\ i \in [i_s, i_e]$, $j \in [j_s, j_e]$, $k \in [k_s, k_e]$

$\mathbf{f}^{h,p}_{J,loc} =$

$\mathbf{f}^{h,p}_{J,loc} + h_1 h_2 h_3 \sum_{i=i_s+n_o}^{i_e-n_o} \sum_{j=j_s+n_o}^{j_e-n_o} \sum_{k=k_s+n_o}^{k_e-n_o} \nabla_h b_{J'}\Big|^{(i,j,k)} (\phi^{(i,j,k)} - V_{J'}^{(i,j,k)})$

$\mathbf{f}^{h}_{J,loc} = \sum_{p=1}^{n_p} \mathbf{f}^{h,p}_{J,loc}$

Output: $\mathbf{f}^{h}_{J,loc}$

Non-local component On approximating the spatial integral using Eqn. 70, the discrete non-local component of the force takes the form

$$\mathbf{f}^{h}_{J,nloc} = -4 \sum_{n=1}^{N_s} \sum_{b=1}^{N_k} w_b g_{nb} \sum_{lm} \gamma_{Jl} \Re \left[Y_{Jnblm} \mathbf{W}_{Jnblm} \right] , \tag{86}$$

where

$$Y_{Jnblm} = h_1 h_2 h_3 \sum_{J'} \sum_{i=1}^{n_1} \sum_{j=1}^{n_2} \sum_{k=1}^{n_3} \psi_n^{*(i,j,k)} e^{-i\mathbf{k_b}\cdot(\mathbf{R}_J - \mathbf{R}_{J'})} \chi_{J'lm}^{(i,j,k)}, \tag{87}$$

$$\mathbf{W}_{Jnblm} = h_1 h_2 h_3 \sum_{J'} \sum_{i=1}^{n_1} \sum_{j=1}^{n_2} \sum_{k=1}^{n_3} \nabla_h \psi_n \Big|^{(i,j,k)} e^{i\mathbf{k_b}\cdot(\mathbf{R}_J - \mathbf{R}_{J'})} \chi_{J'lm}^{*(i,j,k)}. \tag{88}$$

The calculation of $\mathbf{f}_{J,nloc}^h$ in SPARC is outlined in Algorithm 7, which proceeds as follows. For the J^{th} atom in Ω, we determine $\Omega_{r_{J'}^c} \cap \Omega_p$ (with s and e denoting the starting and ending indices) for atoms which have $\Omega_{r_{J'}^c} \cap \Omega \neq \emptyset$. Here, the index J' represents the J^{th} atom and its periodic images. In addition, $\Omega_{r_{J'}^c}$ denotes the cube with side of length $2r_J^c$ centered on the J'^{th} atom. We have chosen $\Omega_{r_{J'}^c}$ to be a cube rather than a sphere due to its simplicity and efficiency within the Euclidean finite-difference discretization. In the overlap region so determined, we interpolate the radial components of the projectors $\chi_{J'lm}^{(i,j,k)}$ on to the finite-difference grid using cubic-splines. Next, we utilize Eqns. 87 and 88 to determine Y_{Jnlm}^p and $\mathbf{W}_{Jnlm}^p$, respectively, which represent the contributions of the p^{th} processor to Y_{Jnlm} and $\mathbf{W}_{Jnlm}$, respectively. Finally, we sum the contributions from all the processors to obtain Y_{Jnlm} and $\mathbf{W}_{Jnlm}$, which are then used to calculate $\mathbf{f}_{J,nloc}^h$ using Eqn. 86 .

Algorithm 7: Calculation of the non-local component of the atomic force

Input: $\mathbf{R}$, $\psi_n^{(i,j,k)}$, γ_{Jl}, χ_{Jlm}, and r_J^c

$Y^p_{Jnblm} = 0$, $\mathbf{W}^p_{Jnblm} = 0$

for $J = 1 \ldots N$ **do**

  for $J' = J^{th}$ *atom and its periodic images for which* $\Omega_{r^c_{J'}} \cap \Omega \neq \emptyset$ **do**

    Determine starting and ending indices i_s, i_e, j_s, j_e, k_s, k_e for $\Omega_{r^c_{J'}} \cap \Omega_p$

    Determine $\chi^{(i,j,k)}_{J'lm}$ $\forall\, i \in [i_s, i_e]$, $j \in [j_s, j_e]$, $k \in [k_s, k_e]$

    $Y^p_{Jnblm} = Y^p_{Jnblm} + h_1 h_2 h_3 \psi^{*(i,j,k)}_n e^{-i\mathbf{k_b}\cdot(\mathbf{R}_J - \mathbf{R}_{J'})} \chi^{(i,j,k)}_{J'lm}$ $\forall\, i \in [i_s, i_e]$,

    $j \in [j_s, j_e]$, $k \in [k_s, k_e]$

    $\mathbf{W}^p_{Jnblm} = \mathbf{W}^p_{Jnblm} + h_1 h_2 h_3 \nabla_h \psi_n\big|^{(i,j,k)} e^{i\mathbf{k_b}\cdot(\mathbf{R}_J - \mathbf{R}_{J'})} \chi^{*(i,j,k)}_{J'lm}$ $\forall\, i \in [i_s, i_e]$,

    $j \in [j_s, j_e]$, $k \in [k_s, k_e]$

$Y_{Jnblm} = \sum_{p=1}^{n_p} Y^p_{Jnblm}$, $\mathbf{W}_{Jnblm} = \sum_{p=1}^{n_p} \mathbf{W}^p_{Jnblm}$

$\mathbf{f}^h_{J,nloc} = -4 \sum_{n=1}^{N_s} \sum_{b=1}^{N_k} w_b g_{nb} \sum_{lm} \gamma_{Jl} \Re\left[Y_{Jnblm} \mathbf{W}_{Jnblm}\right]$

Output: $\mathbf{f}^h_{J,nloc}$

3.4 Examples and Results

In this section, we verify the accuracy and efficiency of SPARC (Simulation Package for Ab-initio Real-space Calculations) for periodic Density Functional Theory (DFT) calculations. In all examples, we utilize a twelfth-order accurate finite-difference discretization, the Perdew-Wang parametrization [86] of the correlation energy calculated by Ceperley-Alder [24], norm-conserving Troullier-Martins pseudopotentials [103], and a smearing of $k_B T = 0.01$ Ha. The cutoff radii for the non-local projectors and the local component of the pseudopotentials are listed in Appendix B. The Monkhorst-Pack [77] grid is used for performing integrations over the Brillouin zone. Unless specified otherwise, the simulations correspond to $\mathbf{k}$ =[0.0 0.0 0.0] (Γ-point).

We solve the linear system corresponding to the Poisson problem using the block-Jacobi preconditioned [42] minimal residual method (MINRES) [80]. Within the CheFSI approach, we utilize a polynomial of degree $m = 20$ for Chebyshev filtering; the Lanczos

method [66] for calculating the extremal eigenvalues of the Hamiltonian $\mathbf{H_b}$; and LAPACK's [3] implementation of the QR algorithm [106] for solving the subspace eigenproblem in Eqn. 78. We calculate the Fermi energy using Brent's method [91], and use Anderson extrapolation [2] with relaxation parameter of 0.3 and mixing history of 7 for accelerating the convergence of the SCF method. Finally, we employ the Polak-Ribiere variant of non-linear conjugate gradients with a secant line search [94] for geometry optimization.

All the results presented here are converged to within the chemical accuracy of 0.001 Ha/atom in the energy and 0.001 Ha/Bohr in the forces. Wherever applicable, the results obtained by SPARC are compared to the well-established plane-wave code ABINIT [43, 45, 44]. The error in energy is defined to be the difference in the magnitude, and the error in forces is defined to be the maximum difference in any component. All simulations are performed on a computer cluster consisting of 16 nodes with the following configuration: Altus 1804i Server - 4P Interlagos Node, Quad AMD Opteron 6276, 16C, 2.3 GHz, 128GB, DDR3-1333 ECC, 80GB SSD, MLC, 2.5" HCA, Mellanox ConnectX 2, 1-port QSFP, QDR, memfree, CentOS, Version 5, and connected through InfiniBand cable.

3.4.1 Convergence with discretization

First, we verify convergence of the energy and atomic forces computed by SPARC with respect to spatial discretization. For this study, we choose three examples: $2 \times 2 \times 2$ unit cells of lithium hydride with lattice constant of 7.37 Bohr and corner lithium atom perturbed by $[0.57\ 0.43\ 0.37]$ Bohr; $2 \times 2 \times 2$ unit cells of silicon with lattice constant of 10.68 Bohr and corner atom perturbed by $[0.93\ 0.50\ 0.20]$ Bohr; and $2 \times 2 \times 2$ unit cells of gold with lattice constant of 8.0 Bohr, one of the domain face-centered atoms perturbed by $[0.85\ 0.50\ 0.30]$ Bohr, and $1 \times 1 \times 2$ Brillouin zone integration. All errors are defined with respect to ABINIT, wherein we employ plane-wave cutoffs of 46, 40, and 46 Ha for lithium hydride, silicon, and gold, respectively, which results in energy and forces that are

converged to within 5×10^{-6} Ha/atom and 5×10^{-6} Ha/Bohr, respectively.

It is clear from Fig. 22—plots of the error in energy and atomic forces with respect to mesh-size—that there is systematic convergence to the reference plane-wave result. On performing a fit to the data, we obtain average convergence rates of approximately $\mathcal{O}(h^{10})$ in the energy and $\mathcal{O}(h^9)$ in the forces. In doing so, the chemical accuracy desired in electronic structure calculations is readily attained. These results demonstrate that SPARC is able to obtain high convergence rates in both the energy and forces, which contributes to its accuracy and efficiency. Moreover, they converge at comparable rates, without need of additional measures such as double-grid [79] or high-order integration [13] techniques.

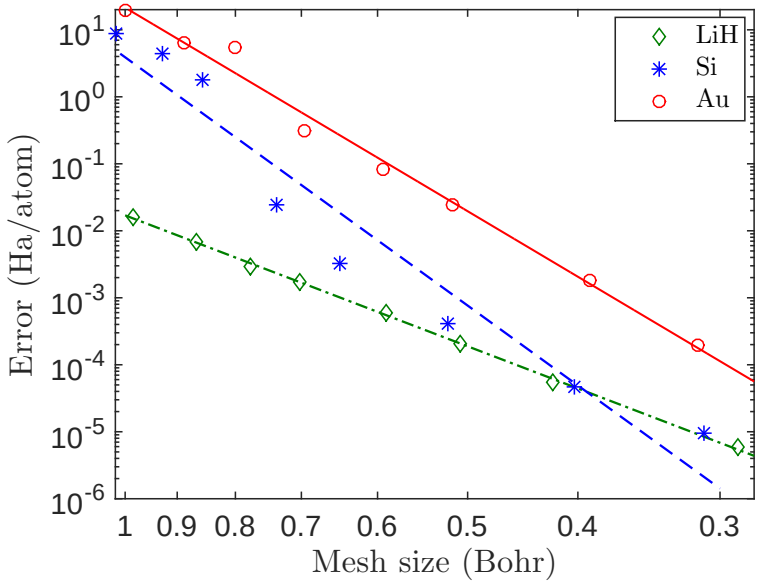

(a) Energy

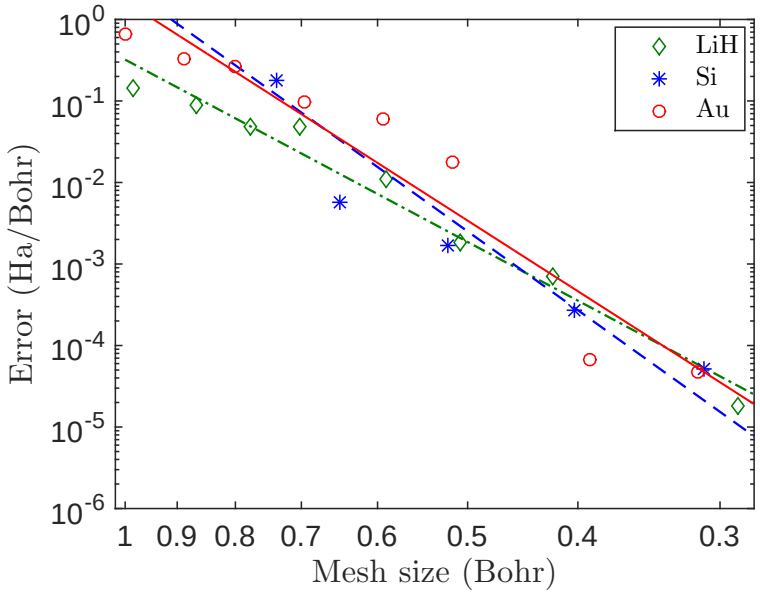

(b) Forces

Figure 9: Convergence of the energy and atomic forces with respect to mesh size to reference planewave result for the lithium hydride, silicon, and gold systems.

3.4.2 Bulk properties

We now verify the ability of SPARC to accurately calculate material bulk properties. We select silicon—8-atom unit cell with $4 \times 4 \times 4$ Brillouin zone integration—as the representative example. In SPARC, we use a mesh-size of $h = 0.407$ Bohr. We compare the results with ABINIT, wherein we choose a plane-wave energy cutoff of 40 Ha, which results in energies that are converged to within 5×10^{-6} Ha/atom. In Fig. 10, we plot the energy so computed by SPARC and ABINIT as a function of the lattice constant. We observe that there is very good agreement between SPARC and ABINIT, with the curves being practically indistinguishable. From a cubic fit to the data, we find that the predicted equilibrium lattice constant, energy, and bulk modulus are in agreement to within 0.003 Bohr, 1×10^{-5} Ha/atom, and 0.18 GPa, respectively.

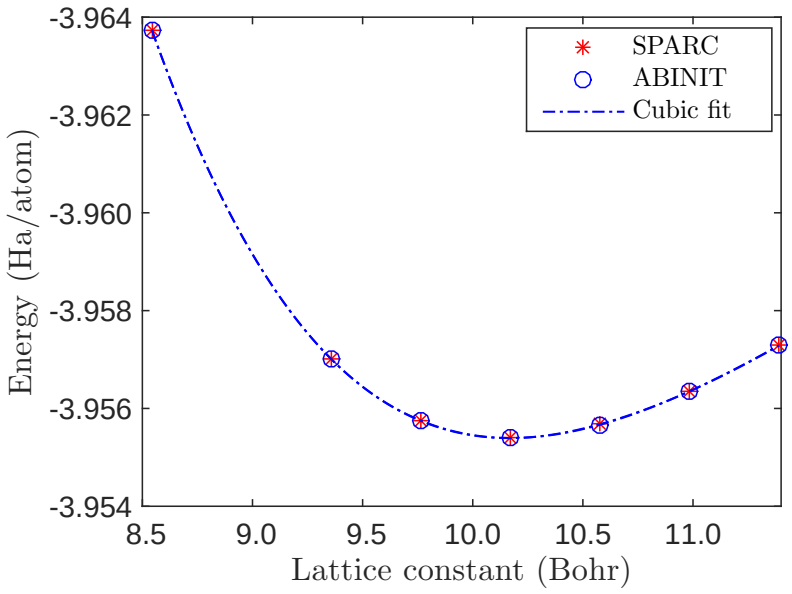

Figure 10: Variation of energy with lattice constant for silicon.

Next, we compare the band structure plot at the equilibrium lattice constants determined above, i.e., 10.157 Bohr for SPARC and 10.160 Bohr for ABINIT. Specifically, we choose the $L - \Gamma - X - \Gamma$ circuit, whose coordinates in terms of the reciprocal lattice vectors are

$[-0.5\ 0.5\ 0.5]$, $[0.0\ 0.0\ 0.0]$, $[1.0\ 0.0\ 0.0]$, and $[1.0\ 1.0\ 1.0]$, respectively. We discretize the $L-\Gamma$, $\Gamma-X$, and $X-\Gamma$ line segments into 10, 12, and 17 divisions, respectively. At each resulting **k**-point, we determine the band structure (at the electronic ground-state) in SPARC by repeating the CheFSI steps until convergence. In Fig. 11, we present the band structure plot so computed by SPARC and compare it with that calculated by ABINIT. It is clear that there is very good agreement, with the curves being nearly identical. In particular, the HOMO eigenvalue, LUMO eigenvalue, and bandgap are in agreement to within 7×10^{-5} Ha, 1×10^{-5} Ha, and 6×10^{-5} Ha, respectively.

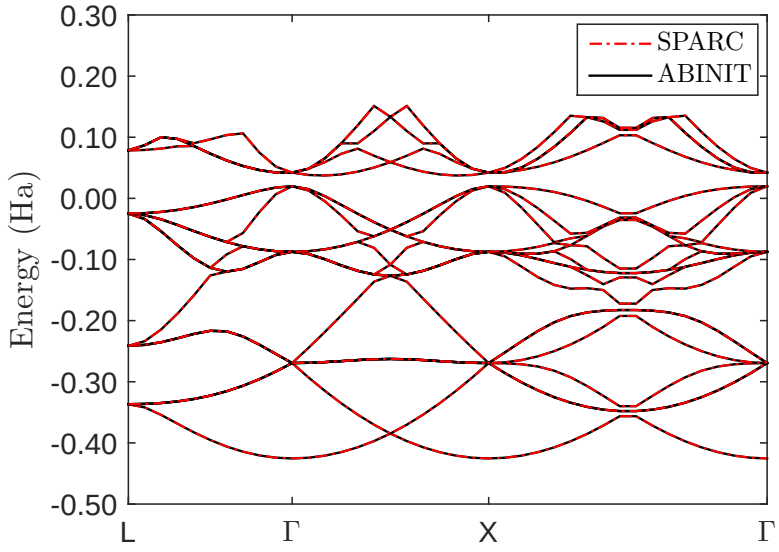

Figure 11: Band structure plot for silicon.

3.4.3 Geometry optimization

We now verify the capacity of SPARC to perform accurate geometry optimizations. To do so, we first check the consistency of the atomic forces with the energy. As representative examples, we select single unit cells of lithium and silicon with lattice constants of 6.59 Bohr and 10.16 Bohr, respectively, and discretize them using mesh sizes of $h = 0.287$ Bohr and 0.248 Bohr, respectively. In Fig. 12, we plot the variation in energy and force when the

body centered lithium atom is displaced along the body diagonal, and one of the face centered silicon atoms is displaced along the face diagonal. Specifically, in Fig. 12a, we plot the computed energy and its curve fit using cubic splines. In Fig. 12b, we plot the computed atomic force and the derivative of the cubic spline fit to the energy. The evident agreement demonstrates that the computed energy and atomic forces are indeed consistent. Moreover, there is no noticeable 'egg-box' effect [17]—a phenomenon arising due to the breaking of the translational symmetry—at meshes required for obtaining chemical accuracies.

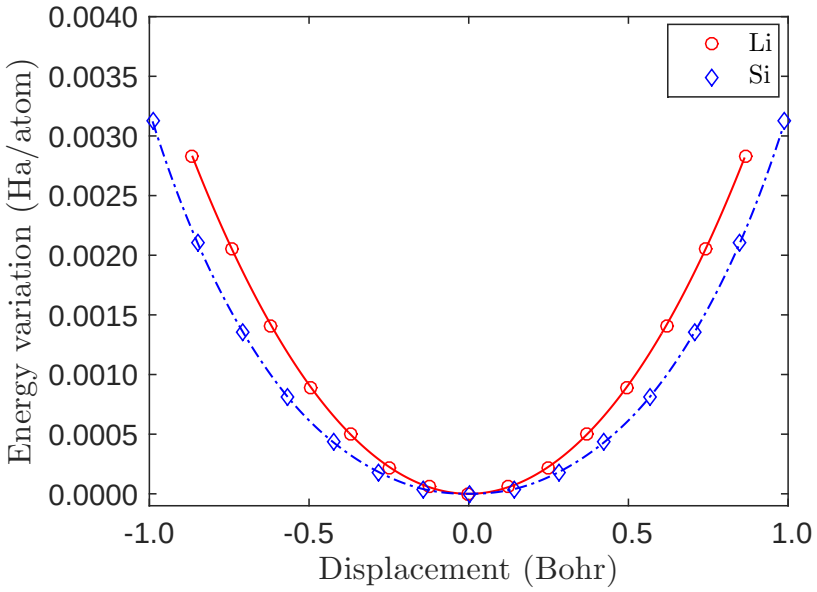

(a) Computed energy and its cubic spline fit

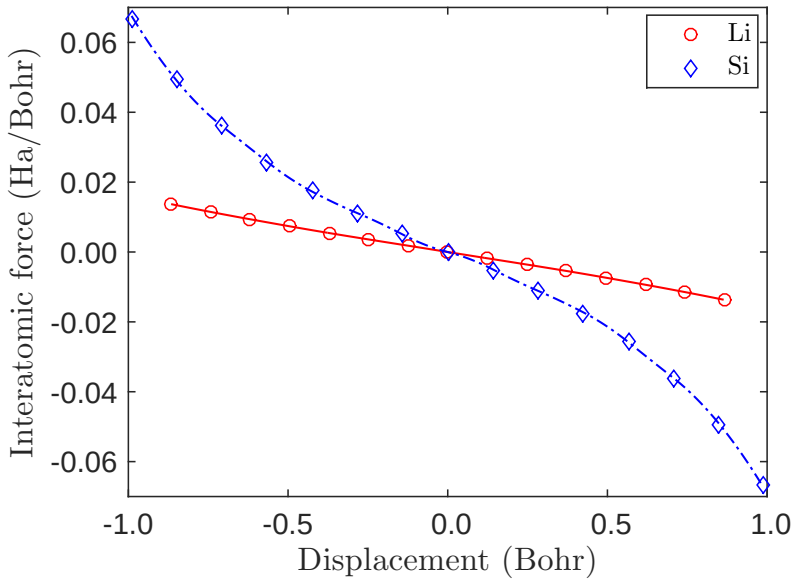

(b) Computed force and the derivative of the cubic spline fit to the energy

Figure 12: Variation in the energy and atomic force as a function of atomic displacement. In lithium, the body centered lithium atom is displaced along the body diagonal. In silicon, one of the face centered silicon atoms is displaced along the face diagonal.

Next, we determine the overall ground-state using SPARC for two systems: $3 \times 3 \times 3$ unit cells of lithium and $2 \times 2 \times 2$ unit cells of silicon, both with a vacancy. We compare the results with ABINIT, wherein we use plane wave cutoffs of 30 Ha and 40 Ha for lithium and silicon, respectively, which results in energy and forces that are converged to within 5×10^{-6} Ha/atom and 5×10^{-6} Ha/Bohr, respectively. We calculate the vacancy formation energy $\mathcal{E}_{vf}$ using the relation [40]

$$\mathcal{E}_{vf} = \mathcal{F}_0 \left(N-1, 1, \frac{N-1}{N}\Omega \right) - \left(\frac{N-1}{N} \right) \mathcal{F}_0(N, 0, \Omega) \,, \tag{89}$$

where $\mathcal{F}_0(N, n_v, \Omega)$ denotes the energy of the system in Ω with N occupied lattice sites and n_v vacancies. The vacancy formation energies so computed by SPARC and ABINIT are in agreement to within 8×10^{-5} Ha. In addition, the fully relaxed atomic positions differ by no more than 0.01 Bohr. The contours of electron density on the mid-plane of these systems are plotted in Fig. 13. Overall we conclude that SPARC is able to accurately perform geometry optimization. Furthermore, the quality of atomic forces makes it suitable for performing ab-initio molecular dynamics [71].

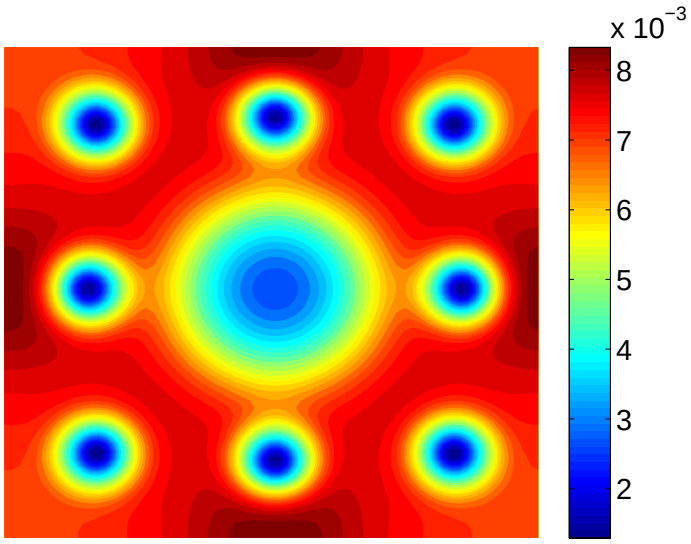

(a) $3 \times 3 \times 3$ unit cells of lithium with a vacancy

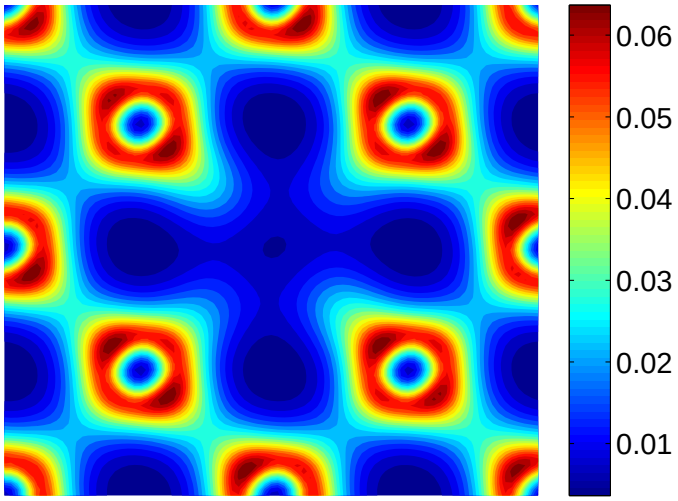

(b) $2 \times 2 \times 2$ unit cells of silicon with a vacancy

Figure 13: Mid-plane electron density contours.

3.4.4 Scaling and Performance

Having verified the accuracy of SPARC relative to ABINIT in previous subsections, we now compare their efficiency. As representative systems, we choose $n \times n \times n$ ($n \in \mathbb{N}$) unit cells of aluminum with a vacancy. In SPARC, we employ a mesh-size of $h = 0.778$ Bohr and Chebyshev polynomial filter of degree 15. In ABINIT, we use a plane-wave energy cutoff of 9 Ha. We choose all the other parameters in both codes so as to achieve an overall accuracy of 5×10^{-4} Ha/atom and 5×10^{-4} Ha/Bohr in the energy and forces, respectively. The times reported here include the calculation of the electronic ground-state as well as the atomic forces.

First, we compare the strong scaling of SPARC with ABINIT for $6 \times 6 \times 6$ FCC unit cells of aluminum with a vacancy. We utilize 4, 8, 64, 144, 480, and 576 cores for performing the simulation with ABINIT, which it suggests is optimal in the range of 1 to 1000 cores. For SPARC, we select 4, 8, 27, 384, 512 and 640 cores. In Fig. 14a, we plot the wall time taken by SPARC and ABINIT as a function of the number of processors. We observe that both SPARC and ABINIT display similar trends with respect to strong scaling, with curves being close to parallel and no further reduction in wall time observed after approximately 640 cores. However, the prefactors of SPARC are up to a factor of 5 smaller than ABINIT.

Next, we compare the weak scaling of SPARC with ABINIT for $3 \times 3 \times 3$, $4 \times 4 \times 4$, $5 \times 5 \times 5$, $6 \times 6 \times 6$, and $7 \times 7 \times 7$ unit cells of aluminum, each with a vacancy. The number of electrons in these systems range from 321 to 4116. For both SPARC and ABINIT, we fix the number of electrons per core to be approximately 96, and choose at most 4 cores from every compute node. In Figure 14b, we present the results so obtained for the variation in total CPU time versus the number of electrons. We again observe similar scaling for both SPARC ($\mathcal{O}(N_e^{3.48})$) and ABINIT ($\mathcal{O}(N_e^{3.67})$). However, the prefactor for SPARC is again noticeably smaller, with speedups over ABINIT ranging from factors of 2.5 to 10. We note that the worse than $\mathcal{O}(N_e^3)$ scaling of both SPARC and ABINIT is a consequence of the increase in the number of SCF iterations with system size. In fact, the average time per

SCF iteration in SPARC and ABINIT scales as $\mathcal{O}(N_e^{2.56})$ and $\mathcal{O}(N_e^{2.8})$, respectively.

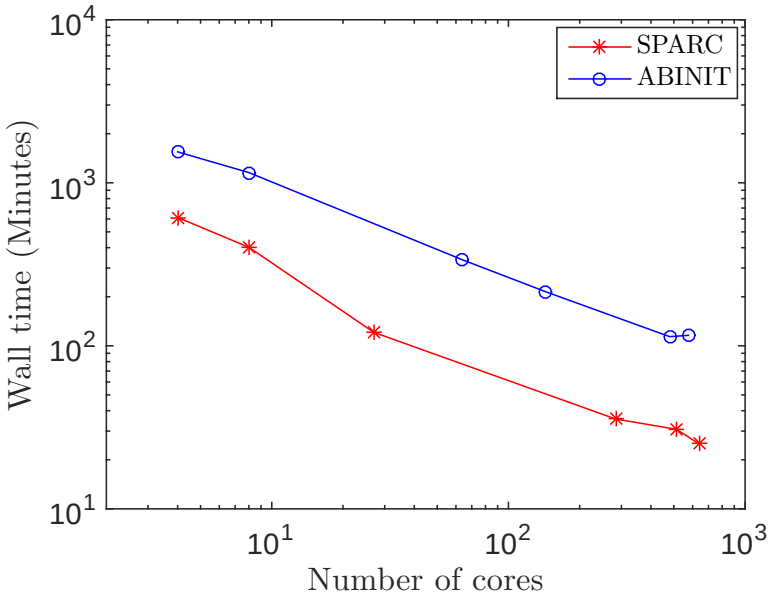

(a) Strong scaling

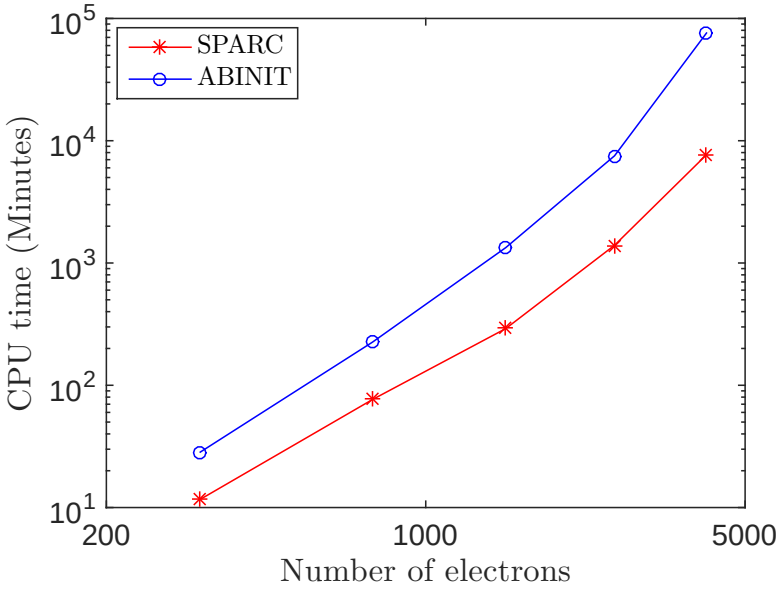

(b) Weak scaling

Figure 14: Strong and weak scaling for SPARC and ABINIT. The system utilized for strong scaling is $6 \times 6 \times 6$ FCC unit cells of aluminum with a vacancy. The systems employed for weak scaling are $3 \times 3 \times 3$, $4 \times 4 \times 4$, $5 \times 5 \times 5$, $6 \times 6 \times 6$, and $7 \times 7 \times 7$ unit cells of aluminum, each with a vacancy.

Finally, we compare the minimum wall time achievable by SPARC and ABINIT for the aforementioned aluminum systems. We restrict the maximum number of electrons per core to 96. In SPARC, we choose the number of cores as multiples of 32, whereas we select the number of cores and parallelization scheme in ABINIT that it suggests are optimal. In Table 4, we present the results for the minimum wall time so achieved. We observe that SPARC outperforms ABINIT by factors larger than 2.5 for all the systems considered. In particular, SPARC requires a factor of approximately 5 less wall time for the largest system. Overall, we conclude that SPARC is a highly efficient DFT formulation and implementation that is very competitive with currently existing highly optimized plane-wave codes.

Table 4: Minimum wall time in minutes for $n \times n \times n$ FCC unit cells of aluminum with a vacancy. The number in brackets denotes the number of cores on which the minimum wall time is achieved.

System	SPARC	ABINIT
$3 \times 3 \times 3$	$0.43\ (64)$	$1.77\ (188)$
$4 \times 4 \times 4$	$1.69\ (96)$	$5.67\ (320)$
$5 \times 5 \times 5$	$6.99\ (256)$	$17.42\ (396)$
$6 \times 6 \times 6$	$20.98\ (640)$	$113.87\ (480)$
$7 \times 7 \times 7$	$79.15\ (704)$	$398.77\ (795)$

CHAPTER IV

PARTIALLY PERIODIC SYSTEMS: SLABS AND WIRES

4.1 Formulation and implementation

In this chapter we extend the formulation developed in chapters 2 and 3 for partially periodic systems. The two cases of partial periodic systems include 1) Periodic boundary conditions in two directions and nonperiodic boundary condition in the third direction. 2) Periodic boundary condition in one direction and nonperiodic boundary condition in the second and third directions.

The formulation and implementation for periodic systems can be extended to partially periodic systems by considering the periodic images of atoms only in the direction(s) of periodicity. We restrict the component to the Block wavevector ($\mathbf{k}$) in the nonperiodic direction to be zero. We enforce zero Dirichlet boundary conditions in the nonperiodic direction(s) on the periodic part of the orbitals ($u_n(\mathbf{x}, \mathbf{k})$) and the electrostatic potential ($\phi(\mathbf{x})$). Within the finite-difference implementation, we enforce zero Dirichlet boundary conditions in the nonperiodic direction(s) by setting $f^{(i,j,k)} = 0$ for any index that does not correspond to a node in the finite difference grid. In the periodic direction(s), we map any index not corresponding to a node in the finite-difference grid to its periodic image with Ω.

4.2 Examples and results

In this section, we verify SPARC for partially periodic systems through selected examples. In all the simulations, we utilize a twelfth-order accurate finite-difference discretization ($n_o = 6$), the Perdew-Wang parametrization [86] of the correlation energy calculated by

Ceperley-Alder [24], a smearing of $k_BT = 1 \times 10^{-2}$ Ha, and norm-conserving Troullier-Martins pseudopotentials [103]. The Monkhorst-Pack [77] grid is used for performing integrations over the Brillouin zone. We solve the linear system corresponding to the Poisson problem using the block-Jacobi preconditioned [42] minimal residual method (MINRES) [80]. Within the CheFSI approach, we utilize a polynomial of degree $m = 20$ for Chebyshev filtering; the Lanczos method [66] for calculating the extremal eigenvalues of the Hamiltonian $\mathbf{H_b}$; and LAPACK's [3] implementation of the QR algorithm [106] for solving the subspace eigenproblem in Eqn. 78. We calculate the Fermi energy using Brent's method [91], and use Anderson extrapolation [2] with relaxation parameter of 0.2 and mixing history of 12 for accelerating the convergence of the SCF method.

4.2.1 Convergence with domain size

We first verify the convergence of the computed energy and atomic forces with respect to the size of the domain Ω. We choose $1 \times 1 \times 5$ aluminum slab (Al_{22}) and (100) silicon nanowire of radius (R=15 Bohr) and length (L = 10.16 Bohr) (Si_{57}) as representative examples of a slab and a wire respectively. For Al_{22}, we use a lattice constant of 7.78 Bohr, utilize a mesh spacing of 0.6 Bohr and consider x and y as periodic directions and z as the nonperiodic direction. For Si_{57}, we use a lattice constant of 10.16 Bohr, utilize a mesh spacing of 0.407 Bohr and consider x to be the periodic direction and y and z as the nonperiodic directions. In Fig. 15b, we present convergence of the energy and atomic forces as the vacuum length in the nonperiodic directions is increased from 4.55 Bohr to 9.35 Bohr for Al_{22} and from 4.10 Bohr to 8.90 Bohr for Si_{57}, with the results obtained for 18 Bohr vacuum length used as reference. We observe exponential convergence of both the energy and the forces to well below accuracies desired in DFT calculations. In fact, even a vacuum length of 6.5 Bohr is sufficient to obtain chemical accuracy in both energy and forces. Overall, these results demonstrate the efficacy of SPARC's capability to efficiently model slabs and wires without issues of interacting periodic images that typically arise

when periodic boundary conditions are used to model partially periodic systems.

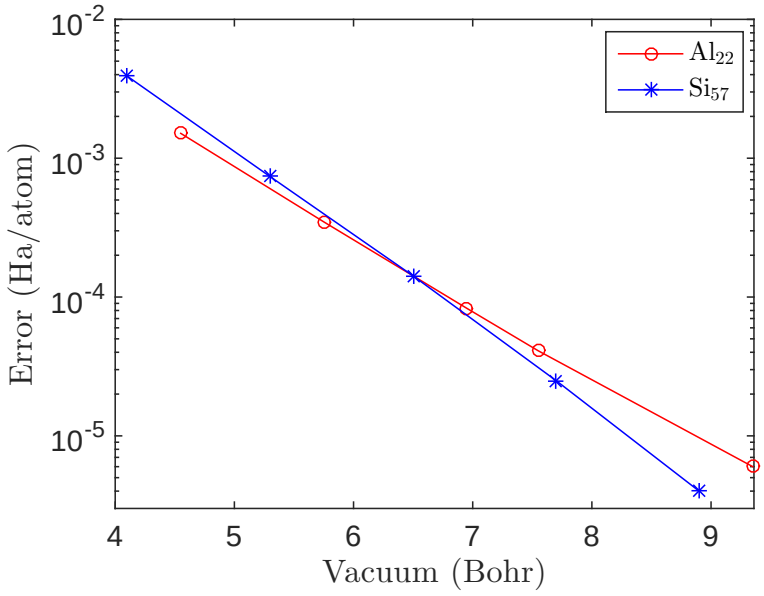

(a) Energy

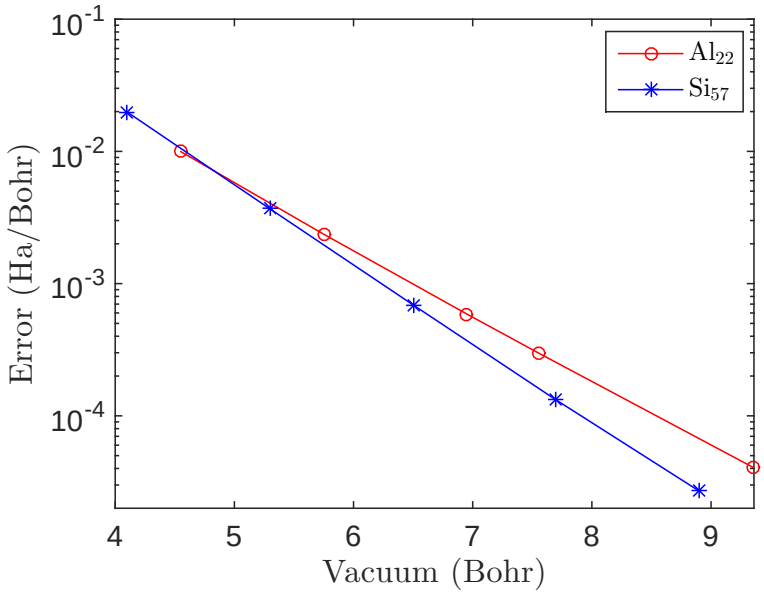

(b) Forces

Figure 15: Convergence of energy and atomic forces with respect to domain size for Al_{22} slab and Si_{57} nanowire.

4.2.2 Aluminum slab: Two dimensional periodic calculation

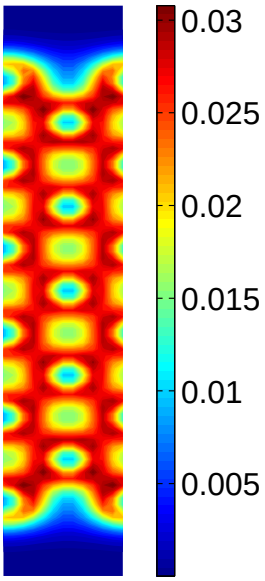

(a) Edge plane

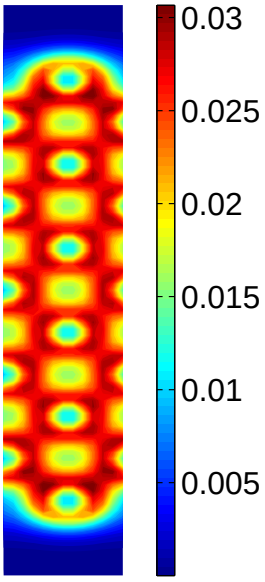

(b) Mid plane

Figure 16: Electron density contours on slices through a (001) slab of FCC Aluminum.

We now verify the accuracy of a two dimensional periodic calculation. For this purpose, we choose $1 \times 1 \times 5$ unit cells of aluminum, a domain size of $\{L_1, L_2, L_3\} = \{7.78, 7.78, 52.8\}$ Bohr and mesh-size of $h = 0.6$ Bohr. We determine the electronic ground-state using SPARC with periodic boundary conditions in the x and y directions and nonperiodic boundary condition in the z direction. We compare the results with ABINIT, wherein we use a domain size of $\{L_1, L_2, L_3\} = \{7.78, 7.78, 64.0\}$ Bohr and plane wave cutoff of 30 Ha. We calculate the surface energy γ of the (001) surface using the relation [88]

$$\gamma = \frac{\mathcal{F}_{0,slab} - N\mathcal{F}_{0,bulk}}{2A}\,, \tag{90}$$

where $\mathcal{F}_{0,slab}$ denotes the energy of the slab with N atoms and $\mathcal{F}_{0,bulk}$ is the energy of an atom in the bulk. The (001) surface energies so computed by SPARC and ABINIT are in agreement to within 7×10^{-7} Ha/Bohr^2. Furthermore, the computed atomic forces are accurate to within 3×10^{-4} Ha/Bohr. In Fig. 16 we plot the electron density contour on slices through a (001) slab of FCC Aluminum.

4.2.3 Silicon nanowire: One dimensional periodic calculation

Here we verify the accuracy of a one dimensional periodic calculation. For this purpose, we choose a (100) silicon nanowire of radius (R = 15 Bohr) and length (L = 10.16 Bohr) (Si_{57}), a domain size of $\{L_1, L_2, L_3\} = \{10.16, 40.8, 40.8\}$ Bohr, mesh-size of $h = 0.407$ Bohr. We determine the electronic ground-state using SPARC with periodic boundary conditions in the x direction and nonperiodic boundary condition in the y and z directions. We compare the results with ABINIT, wherein we use a domain size of $\{L_1, L_2, L_3\} = \{10.16, 64.0, 64.0\}$ Bohr and plane wave cutoff of 40 Ha. The computed energies and atomic forces are accurate to within 3×10^{-5} Ha/atom and 2×10^{-4} Ha/Bohr. In Fig. 17, we plot the electron density contours on slices through a (100) wire of Silicon.

We obtain the density of states (D) using the expression [70]

$$D(\mathcal{E}) = 2\sum_{n=1}^{N_s} \fint_{BZ} \delta(\lambda_n(\mathbf{k}) - \mathcal{E})\, \mathrm{d}\mathbf{k}\,, \tag{91}$$

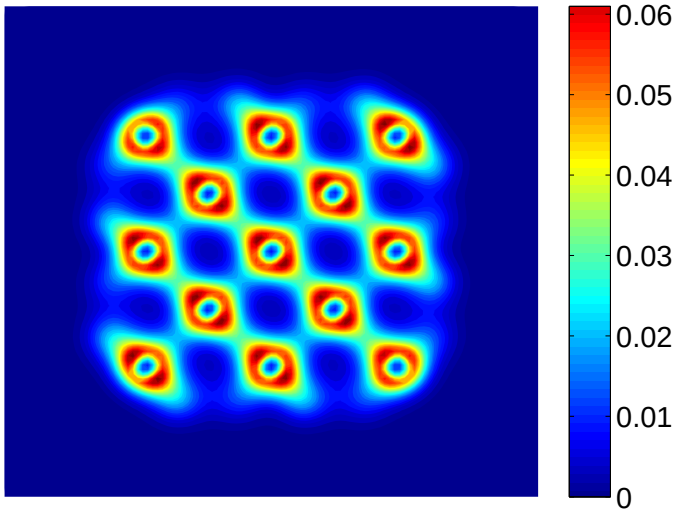

(a) transverse

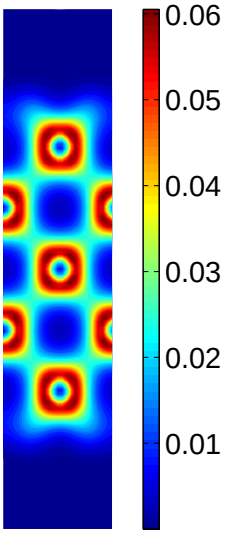

(b) longitudinal

Figure 17: Electron density contours on slices through a (100) wire of silicon.

where δ is the dirac delta distribution. In Fig. 18, we present the density of states plot for the nanowire so computed by SPARC and compare it with ABINIT. It is clear that there is very good agreement between the SPARC and ABINIT.

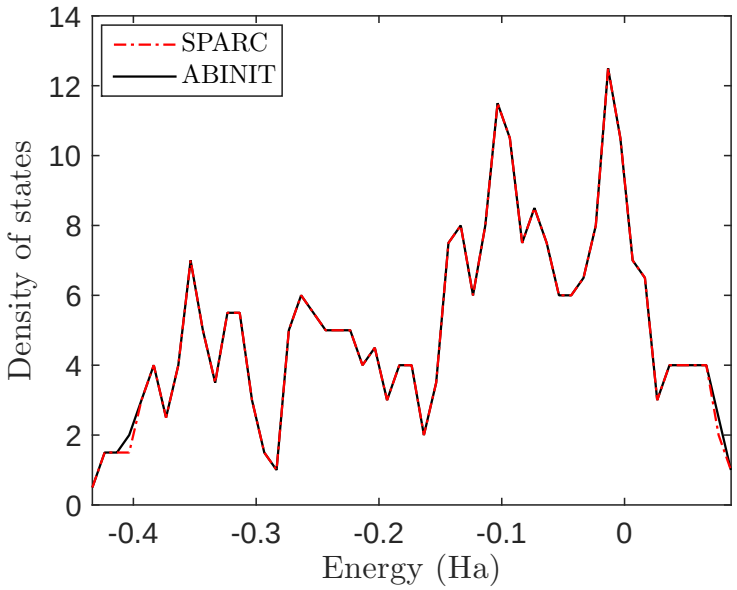

Figure 18: Density of states for a (100) wire of silicon.

CHAPTER V

CONCLUDING REMARKS AND FUTURE DIRECTIONS

This thesis presents an accurate and efficient finite-difference formulation and parallel implementation of Density Functional Theory (DFT) for isolated clusters, periodic and partially periodic systems. By employing the Chebyshev polynomial filtered self-consistent field iteration in conjunction with the reformulation of the electrostatics and the non-local component of the atomic force, we have developed a framework using the finite-difference representation wherein energies and forces can be efficiently evaluated to within the chemical accuracies desired in electronic structure calculations. We name this developed framework as SPARC (Simulation Package for Ab-initio Real-space Calculations). Through a variety of examples consisting of both light and heavy elements, we have demonstrated that SPARC obtains exponential convergence in energies and forces with domain size; systematic convergence in the energy and forces with respect to spatial discretization at comparably high rates to reference plane-wave results; forces that are consistent with the energy, both being free from any noticeable 'egg-box' effect; and accurate ground-state properties like equilibrium energies, geometries and vibrational spectra. Moreover, we have shown that the weak and strong parallel scaling of SPARC is very similar to well-established and optimized plane-wave codes for systems consisting of up to thousands of electrons, but with a significantly smaller prefactor. The potential for significant improvement of SPARC include the incorporation of efficient and parallel scalable eigendecomposition techniques for the solution of the subspace eigenvalue problem, which is expected to become the dominant cost for systems consisting of tens of thousands of electrons.

5.1 Future directions

The developed computational framework provides a foundation for pursuing large-scale ab-initio simulations efficiently. Here we shortly discuss a few future directions.

Design and discovery of new materials The developed framework is capable of efficiently simulating nanostructures of different elements across the periodic table. Therefore, first principles based design and discovery of novel nanostructures by performing a systematic search for new materials among clusters of different kinds of atoms is an important avenue of research. Incorporating ideas of symmetry reduction within the current framework is likely to be useful and will further accelerate the search.

Nanomechanics Ab-initio simulations provide further insights into the behavior of nanostructures. Some of the potential applications include strain engineering of nanomaterials, stability of nano structures, flexoelectricity. In particular, the capability of the developed framework to accurately model partially periodic systems makes it an effective tool for ab-initio simulations of 2D and 1D materials. Incorporating recently developed idea of ab-initio simulation of bending [8] into the developed framework opens up a completely new avenue of research and a plethora of applications.

Ab-initio molecular dynamics Integrating Molecular Dynamics (MD) algorithms into the developed framework will enable the study of propagating a system through time. The current framework is expected to be competitive in simulating longer time scales for ab-initio MD.

Crystal defects Defects play a vital role in rendering interesting and important properties to solids. For example dislocations give rise to plasticity, vacancies give rise to creep, spall and radiation aging, dopants affect semiconducting properties. The electronic structure of the core, discrete effects of the lattice and the long range elastic fields play important part

in influencing the properties exhibited by defects [99]. The capability to model different boundary conditions within the developed real-space framework promotes the development of methods to study materials defects from an ab-initio perspective.

APPENDIX A

ELECTROSTATIC CORRECTION FOR OVERLAPPING PSEUDOCHARGE DENSITIES

A.1 Norperiodic formulation

In ab-initio calculations, even if the pseudopotential approximation is employed, the repulsive energy is still calculated with the nuclei treated as point charges. The electrostatic formulation employed in this work does not make this distinction, resulting in disagreement with convention for overlapping pseudocharge densities. The correction to the repulsive energy which reestablishes agreement can be written as [101]

$$\begin{aligned} E_c(\mathbf{R}) &= \frac{1}{2}\int_{\mathbb{R}^3}\Big(\tilde{b}(\mathbf{x},\mathbf{R})+b(\mathbf{x},\mathbf{R})\Big)\,V_c(\mathbf{x},\mathbf{R})\,\mathrm{d}\mathbf{x}+\frac{1}{2}\sum_{J=1}^{N}\int_{\mathbb{R}^3} b_J(\mathbf{x},\mathbf{R}_J)V_J(\mathbf{x},\mathbf{R}_J)\,\mathrm{d}\mathbf{x} \\ &\quad -\frac{1}{2}\sum_{J=1}^{N}\int_{\mathbb{R}^3}\tilde{b}_J(\mathbf{x},\mathbf{R}_J)\tilde{V}_J(\mathbf{x},\mathbf{R}_J)\,\mathrm{d}\mathbf{x}\,, \end{aligned} \tag{92}$$

where

$$V_c(\mathbf{x},\mathbf{R})=\sum_{J=1}^{N}\Big(\tilde{V}_J(\mathbf{x},\mathbf{R}_J)-V_J(\mathbf{x},\mathbf{R}_J)\Big)\,. \tag{93}$$

Additionally, $\tilde{b}$ denotes the reference pseudocharge density, and $\tilde{b}_J$ represents the spherically symmetric and compactly supported reference charge density of the J^{th} nucleus that generates the potential $\tilde{V}_J$, i.e.,

$$\tilde{b}(\mathbf{x},\mathbf{R})=\sum_{J=1}^{N}\tilde{b}_J(\mathbf{x},\mathbf{R}_J)\,,\quad \tilde{b}_J(\mathbf{x},\mathbf{R}_J)=-\frac{1}{4\pi}\nabla^2\tilde{V}_J(\mathbf{x},\mathbf{R}_J)\,,\quad \int_{\mathbb{R}^3}\tilde{b}_J(\mathbf{x},\mathbf{R}_J)\,\mathrm{d}\mathbf{x}=Z_J\,. \tag{94}$$

The discrete form of the repulsive energy correction is obtained by approximating the integrals in Eqn. 92 using the integration rule in Eqn. 23:

$$E_c^h = \frac{1}{2}h^3 \sum_{i=1}^{n_1}\sum_{j=1}^{n_2}\sum_{k=1}^{n_3}\left((\tilde{b}^{(i,j,k)} + b^{(i,j,k)})V_c^{(i,j,k)} + \sum_{J=1}^{N} b_J^{(i,j,k)} V_J^{(i,j,k)} - \sum_{J=1}^{N} \tilde{b}_J^{(i,j,k)} \tilde{V}_J^{(i,j,k)}\right), \tag{95}$$

where $V_c^{(i,j,k)}$ is obtained by using Eqn. 93.

The correction in the atomic forces arising from the overlapping pseudocharges can be written as [101]

$$\begin{aligned}
& \mathbf{f}_{J,c}(\mathbf{R}) \\
= \; & \frac{1}{2}\int_{\mathbb{R}^3} \Big[\nabla\tilde{b}_J(\mathbf{x},\mathbf{R}_J)\left(V_c(\mathbf{x},\mathbf{R}) - \tilde{V}_J(\mathbf{x},\mathbf{R}_J)\right) + \nabla b_J(\mathbf{x},\mathbf{R}_J)\left(V_c(\mathbf{x},\mathbf{R}) + V_J(\mathbf{x},\mathbf{R}_J)\right) \\
+ \; & \left(\nabla\tilde{V}_J(\mathbf{x},\mathbf{R}_J) - \nabla V_J(\mathbf{x},\mathbf{R}_J)\right)\left(\tilde{b}(\mathbf{x},\mathbf{R}) + b(\mathbf{x},\mathbf{R})\right) \\
+ \; & b_J(\mathbf{x},\mathbf{R}_J)\nabla V_J(\mathbf{x},\mathbf{R}_J) - \tilde{b}_J(\mathbf{x},\mathbf{R}_J)\nabla\tilde{V}_J(\mathbf{x},\mathbf{R}_J)\Big]\,\mathrm{d}\mathbf{x}\,,
\end{aligned}$$

whose discrete form is

$$\begin{aligned}
\mathbf{f}_{J,c}^h \; = \; & \frac{1}{2}h^3 \sum_{i=1}^{n_1}\sum_{j=1}^{n_2}\sum_{k=1}^{n_3}\Big(\nabla_h\tilde{b}\big|^{(i,j,k)}\left(V_c^{(i,j,k)} - \tilde{V}_J^{(i,j,k)}\right) + \nabla_h b_J\big|^{(i,j,k)}\left(V_c^{(i,j,k)} + V_J^{(i,j,k)}\right) \\
& + \nabla_h(\tilde{V}_J - V_J)\big|^{(i,j,k)}\left(\tilde{b}^{(i,j,k)} + b^{(i,j,k)}\right) + b_J^{(i,j,k)}\nabla_h V_J\big|^{(i,j,k)} - \tilde{b}_J^{(i,j,k)}\nabla_h\tilde{V}_J\big|^{(i,j,k)}\Big)
\end{aligned}$$

. (96)

We choose $\tilde{V}$ to be the potential that has previously been employed for generating neutralizing densities in all-electron calculations [84].

It is worth noting that it is indeed possible to correct for the error in repulsive energy and the corresponding force by only considering the pseudocharges that overlap. However, this requires the creation of neighbor lists, which need to be updated at every relaxation step. In SPARC, we employ the corrections in Eqns. 95 and 96 because of their simplicity and accuracy in the context of our electrostatic formulation, and their efficiency in the setting of scalable high performance computing.

In Fig. 19, we present the magnitude of the repulsive energy correction and the correction in the atomic force as a function of the interatomic distance for the N_2, and O_2

molecules for mesh-size of $h = 0.2$ Bohr. The values of the repulsive energy correction and the correction in the atomic force at the equilibrium bond length is 4.5731×10^{-4} Ha/atom and 3.2852×10^{-1} Ha/Bohr for O_2, and -9.3455×10^{-2} Ha/atom and 7.3189×10^{-1} Ha/Bohr for N_2.

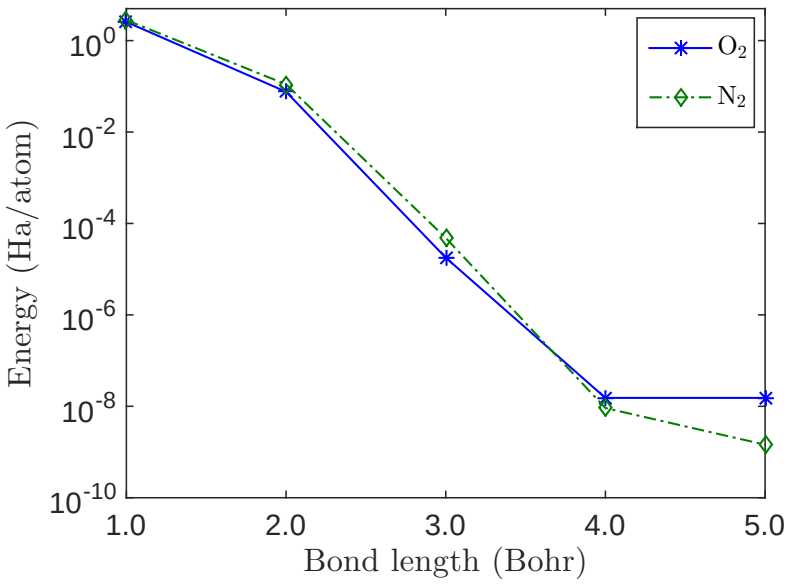

(a) Energy

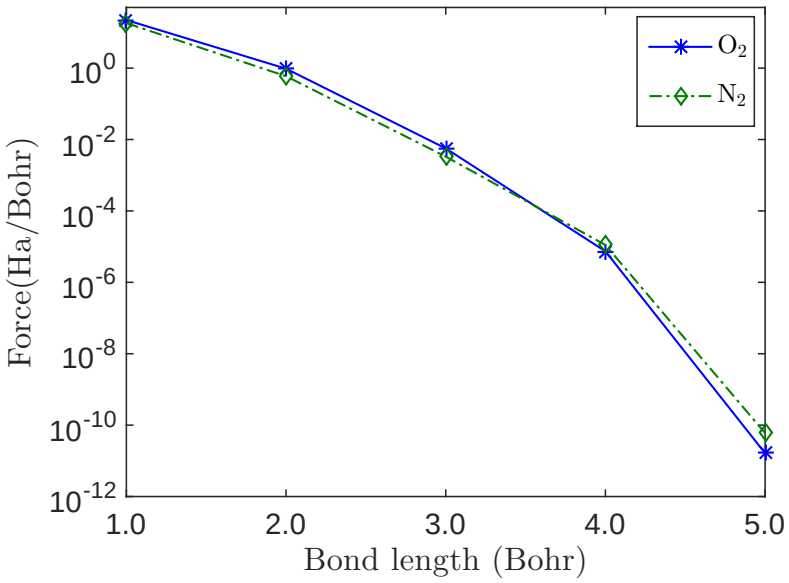

(b) Atomic force

Figure 19: Variation in the magnitude of repulsive energy correction and the correction in the atomic force as a function of interatomic distance for the N_2, and O_2 molecules.

A.2 Periodic formulation

In the periodic setting, we can write

$$\begin{aligned} E_c(\mathbf{R}) &= \frac{1}{2}\int_\Omega \left(\tilde{b}(\mathbf{x},\mathbf{R}) + b(\mathbf{x},\mathbf{R})\right) V_c(\mathbf{x},\mathbf{R})\,\mathrm{d}\mathbf{x} + \frac{1}{2}\sum_I \int_\Omega b_I(\mathbf{x},\mathbf{R}_I) V_I(\mathbf{x},\mathbf{R}_I)\,\mathrm{d}\mathbf{x} \\ &\quad -\frac{1}{2}\sum_I \int_\Omega \tilde{b}_I(\mathbf{x},\mathbf{R}_I)\tilde{V}_I(\mathbf{x},\mathbf{R}_I)\,\mathrm{d}\mathbf{x}\,, \end{aligned} \tag{97}$$

where the summation index I runs over all atoms in $\mathbb{R}^3$, and

$$V_c(\mathbf{x},\mathbf{R}) = \sum_I \left(\tilde{V}_I(\mathbf{x},\mathbf{R}_I) - V_I(\mathbf{x},\mathbf{R}_I)\right)\,. \tag{98}$$

In addition, $\tilde{b}$ denotes the reference pseudocharge density, and $\tilde{b}_I$ represents the spherically symmetric and compactly supported reference charge density of the I^{th} nucleus that generates the potential $\tilde{V}_I$, i.e.,

$$\tilde{b}(\mathbf{x},\mathbf{R}) = \sum_I \tilde{b}_I(\mathbf{x},\mathbf{R}_J)\,, \qquad \tilde{b}_I(\mathbf{x},\mathbf{R}_I) = -\frac{1}{4\pi}\nabla^2\tilde{V}_I(\mathbf{x},\mathbf{R}_I)\,, \tag{99}$$

$$\int_\Omega \tilde{b}(\mathbf{x},\mathbf{R})\,\mathrm{d}\mathbf{x} = -N_e\,, \qquad \int_{\mathbb{R}^3} \tilde{b}_I(\mathbf{x},\mathbf{R}_I)\,\mathrm{d}\mathbf{x} = Z_I\,. \tag{100}$$

The discrete form of the repulsive energy correction in Eqn. 97 takes the form

$$E_c^h = \frac{1}{2}h_1h_2h_3\sum_{i=1}^{n_1}\sum_{j=1}^{n_2}\sum_{k=1}^{n_3}\left((\tilde{b}^{(i,j,k)} + b^{(i,j,k)})V_c^{(i,j,k)} + \sum_I b_I^{(i,j,k)}V_I^{(i,j,k)} - \sum_I \tilde{b}_I^{(i,j,k)}\tilde{V}_I^{(i,j,k)}\right) \tag{101}$$

where the integrals have been approximated using the trapezoidal rule in Eqn. 70. The solution of Eqn. 98 is accurate to within a constant, which is determined by evaluating $\sum_I (V_I(\mathbf{x},\mathbf{R}_I) - \tilde{V}_I(\mathbf{x},\mathbf{R}_I))$ at any point in space.

The correction to the atomic forces can be written as [101]

$$\begin{aligned} &\mathbf{f}_{J,c}(\mathbf{R}) = \\ &\frac{1}{2}\sum_{J'}\int_\Omega \left[\nabla\tilde{b}_{J'}(\mathbf{x},\mathbf{R}_{J'})\left(V_c(\mathbf{x},\mathbf{R}) - \tilde{V}_{J'}(\mathbf{x},\mathbf{R}_{J'})\right) + \nabla b_{J'}(\mathbf{x},\mathbf{R}_{J'})\left(V_c(\mathbf{x},\mathbf{R}) + V_{J'}(\mathbf{x},\mathbf{R}_{J'})\right)\right. \\ &+ \left(\nabla\tilde{V}_{J'}(\mathbf{x},\mathbf{R}_{J'}) - \nabla V_{J'}(\mathbf{x},\mathbf{R}_{J'})\right)\left(\tilde{b}(\mathbf{x},\mathbf{R}) + b(\mathbf{x},\mathbf{R})\right) + b_{J'}(\mathbf{x},\mathbf{R}_{J'})\nabla V_{J'}(\mathbf{x},\mathbf{R}_{J'}) \\ &- \left.\tilde{b}_{J'}(\mathbf{x},\mathbf{R}_{J'})\nabla\tilde{V}_{J'}(\mathbf{x},\mathbf{R}_{J'})\right]\mathrm{d}\mathbf{x}\,, \end{aligned} \tag{102}$$

whose discrete form:

$$\begin{aligned}
&\mathbf{f}^h_{J,c} = \\
&\frac{1}{2}h_1h_2h_3\sum_{J'}\sum_{i=1}^{n_1}\sum_{j=1}^{n_2}\sum_{k=1}^{n_3}\Bigg(\nabla_h\tilde{b}_{J'}\Big|^{(i,j,k)}\left(V_c^{(i,j,k)}-\tilde{V}_{J'}^{(i,j,k)}\right)+\nabla_h b_{J'}\Big|^{(i,j,k)}\left(V_c^{(i,j,k)}+V_{J'}^{(i,j,k)}\right)\\
+\quad&\nabla_h(\tilde{V}_{J'}^{(i,j,k)}-V_{J'}^{(i,j,k)})\Big|^{(i,j,k)}\left(\tilde{b}^{(i,j,k)}+b^{(i,j,k)}\right)+b_{J'}^{(i,j,k)}\nabla_h V_{J'}\Big|^{(i,j,k)}-\tilde{b}_{J'}^{(i,j,k)}\nabla_h\tilde{V}_{J'}\Big|^{(i,j,k)}\Bigg).
\end{aligned} \tag{103}$$

As before, the summation J' runs over the J^{th} atom and its periodic images.

APPENDIX B

PSEUDOPOTENTIAL PARAMETERS

In Table 5, we list the cutoff radii (r_j^c) used for generating the different angular momentum components within the Troullier-Martins pseudopotential. We choose the $l = 0$ pseudopotential component as local in all the simulations.

Table 5: Cutoff radii for non-local projectors within the Troullier-Martins pseudopotential.

Atom type	Radial cutoff (Bohr)		
	$l = 0$	$l = 1$	$l = 2$
H	1.25	–	–
Li	2.40	2.40	–
C	1.50	1.54	–
N	1.50	1.50	–
O	1.45	1.45	–
Al	2.60	2.60	–
Si	1.80	1.80	1.80
Pt	2.45	2.45	2.45
Au	2.60	2.60	2.60

APPENDIX C

PROPERTIES OF THE DISCRETE PSEUDOCHARGE DENSITY

The continuous pseudocharge density for the atom positioned at $\mathbf{R}_J$ has compact support in a sphere of radius r_J^c centered at $\mathbf{R}_J$, where r_J^c is the cutoff radius for the local component of the pseudopotential. Though the corresponding discrete pseudocharge density has infinite extent, it still possesses exponential decay. This is evident from Fig. 20, where we plot the normalized error in the net enclosed charge as a function of the pseudocharge radius r_J^b for a mesh-size of $h = 0.5$ Bohr. It is clear that a suitable finite truncation radius can indeed be chosen such that there is no significant loss of accuracy.

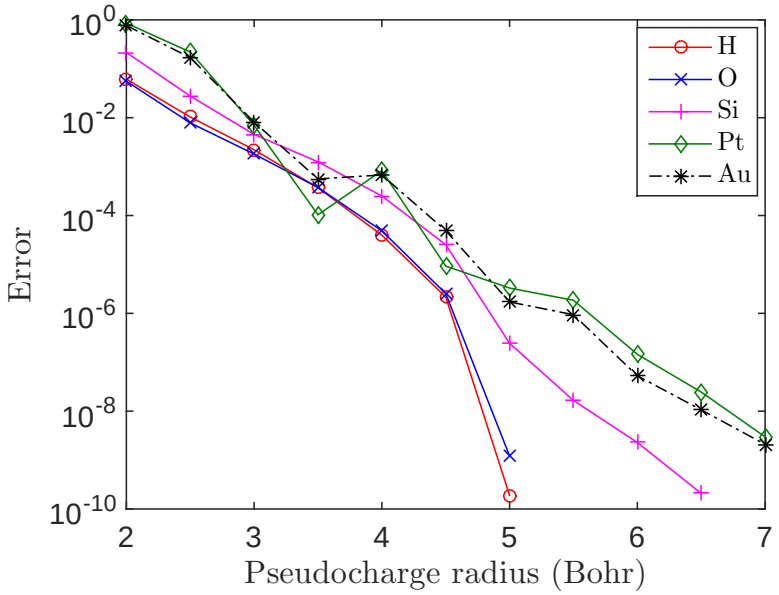

Figure 20: Normalized error in the net enclosed charge as a function of pseudocharge radius. The results for carbon and nitrogen are identical to oxygen.

In this work, we choose the truncation radius r_J^b for each pseudocharge density such that

Eqn. 74 is satisfied to within a tolerance of $\varepsilon_b = 10^{-8}$. In Fig. 21, we plot the r_J^b required to achieve this desired accuracy as a function of mesh-size. It is clear that as the mesh becomes finer, r_J^b becomes smaller, with $r_J^b \to r_J^c$ as $h \to 0$. The slight non-monotonicity of the curves plotted in Fig. 21 is due to the fact that r_J^b is chosen to be a multiple of the mesh size h in SPARC.

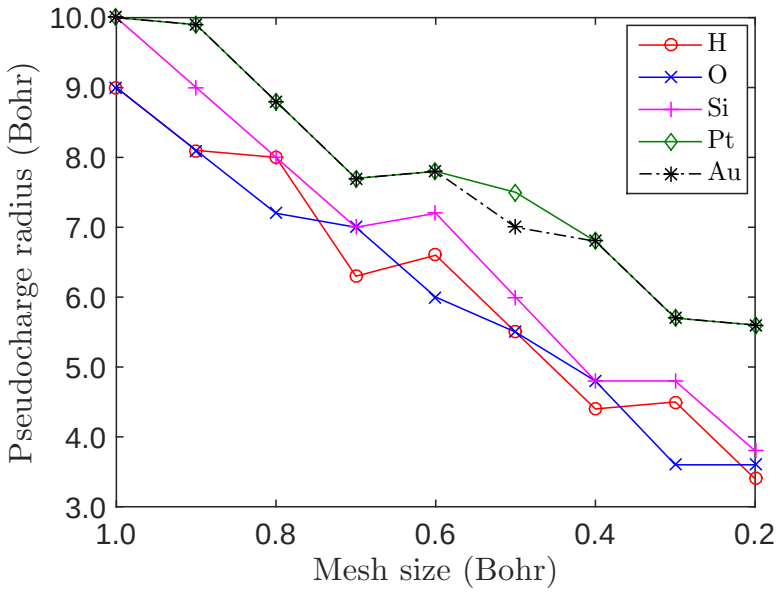

Figure 21: Variation of pseudocharge radius as a function of mesh spacing. The results for carbon and nitrogen are identical to oxygen.

APPENDIX D

COMPARISON WITH EXISTING REAL-SPACE CODES

We compare the convergence of energies and atomic forces with respect to the finite difference mesh-size for SPARC, PARSEC and OCTOPUS. For the comparisons, we use the latest released versions of PARSEC (version 1.3.6) and OCTOPUS (version 5.0.1). As a representative example we choose the $Si_{29}H_{36}$ cluster and the central Silicon atom perturbed by $[0.4\ 0.3\ 0.6]$ Bohr. All errors are defined with respect to ABINIT, wherein we employ plane-wave cutoffs of 30 Ha along with domain sizes of $\{L_1, L_2, L_3\} = \{42, 42, 42\}$ Bohr. The resulting reference energies and forces are converged to within 5.0×10^{-6} Ha/atom and 5.0×10^{-6} Ha/Bohr respectively. In Fig 22 we plot error in energy and forces calculated using SPARC, PARSEC and OCTOPUS, with respect to mesh size. We observe that there is a systematic convergence of both energies and forces for SPARC and OCTOPUS. For PARSEC, the rate of decrease in error reduces from 0.5 mesh onwards. On performing a fit to the data, we obtain average convergence rates of $\mathcal{O}(h^{8.85})$ for SPARC, $\mathcal{O}(h^{7.15})$ for PARSEC and $\mathcal{O}(h^{8.64})$ for OCTOPUS in energy and $\mathcal{O}(h^{9.62})$ for SPARC, $\mathcal{O}(h^{10.05})$ for PARSEC and $\mathcal{O}(h^{10.09})$ for OCTOPUS in the forces.

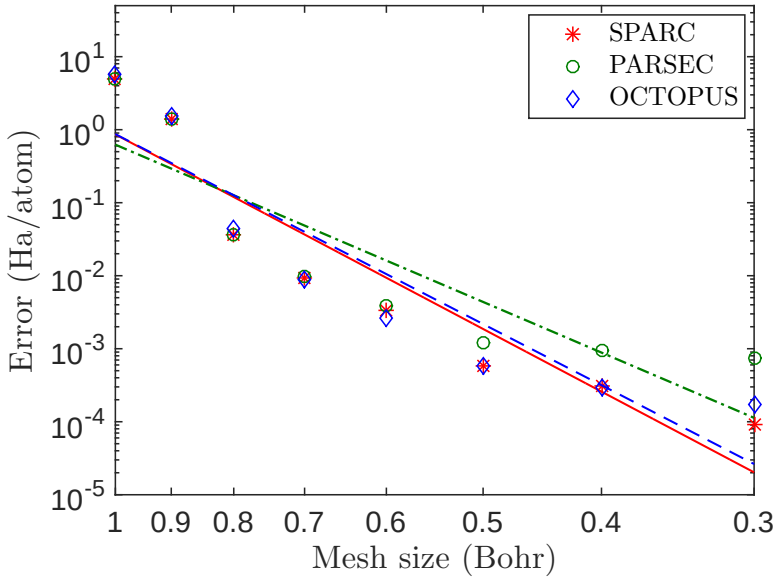

(a) Energy

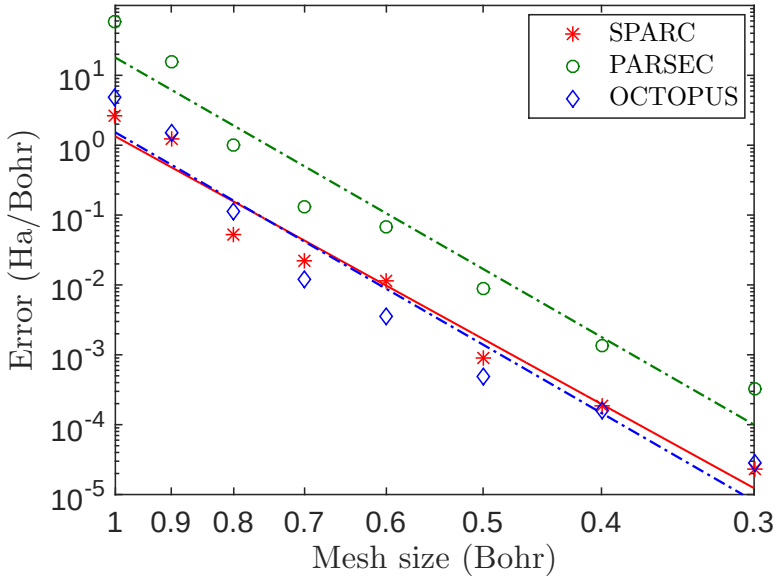

(b) Forces

Figure 22: Convergence of the energy and atomic forces with respect to mesh size to reference planewave result for the $Si_{29}H_{36}$ cluster.

Next, we compare the scaling and performance of SPARC, PARSEC, OCTOPUS and

ABINIT. For this study, we use mesh spacing of 0.5 Bohr for SPARC, 0.5 Bohr for OCTOPUS and 0.5 and 0.3 Bohr (mesh giving chemical accuracy in forces) for PARSEC. We use the planewave energy cutoff of 16 Ha in ABINIT. We choose all other parameters so as to obtain the chemical accuracy of 0.001 Ha/atom in energy and 0.001 Ha/Bohr in the atomic force. For all our comparisons, we exclude the time for the first SCF iteration.

We first compare the strong scaling of the different codes for the $Si_{275}H_{172}$ cluster. For SPARC and ABINIT, We utilize the same number cores as used in the strong scaling study discussed in Section 2.4.4 and we use a maximum of 640 cores for PARSEC and 704 cores for OCTOPUS. In Fig. 23a, we present the wall time for an electronic ground-state calculation taken by SPARC, PARSEC, OCTOPUS and ABINIT as the number of processors is increased. We observe that SPARC outperforms PARSEC by upto factors of 21 for 0.5 Bohr mesh size and 221 for 0.3 Bohr mesh size, OCTOPUS by up to factors of 14 and ABINIT by up to factors of 6.8.

Next, we compare the weak scaling of SPARC, PARSEC, OCTOPUS and ABINIT. We choose the $Si_{29}H_{36}$, $Si_{71}H_{84}$, $Si_{275}H_{172}$, $Si_{525}H_{276}$ and $Si_{849}H_{372}$ nanoclusters for this study. For all the codes, we fix the number of electrons per core to be approximately 160, and select at most 4 cores from every compute node. In Fig. 23b, we present the results so obtained for the variation in total CPU time versus the number of electrons. We observe scaling of $\mathcal{O}(N_e^{2.54})$ for SPARC, $\mathcal{O}(N_e^{3})$ for PARSEC, $\mathcal{O}(N_e^{3.19})$ for OCTOPUS and $\mathcal{O}(N_e^{2.75})$ for ABINIT. Finally, we compare the minimum wall time achievable by SPARC, PARSEC, OCTOPUS and ABINIT for the aforementioned nanoclusters with the exception of $Si_{849}H_{372}$, for which the resources currently available to us are insufficient. We present the results so obtained in Table 6. We observe that SPARC is able to achieve smaller wall times by factors larger than 5.8 compared PARSEC (0.5 Bohr mesh size), 34 compared to PARSEC (0.3 Bohr mesh size), 5.1 compared to OCTOPUS and 6.8 compared to ABINIT for all the systems considered. In particular, SPARC requires a factor of approximately 21.4 less wall time than PARSEC (0.5 Bohr mesh size), 12.6 less wall time than OCTOPUS and

7.0 less wall time than ABINIT for the $Si_{525}H_{276}$ nanocluster. Overall, these results indicate that SPARC is a highly efficient DFT formulation and implementation that is highly competitive with both well-optimized real-space and plane-wave codes.

Table 6: Minimum wall time in minutes achieved by SPARC, PARSEC, OCTOPUS and ABINIT for hydrogen passivated silicon nanoclusters. The number in brackets represents the number of cores on which the minimum wall time is achieved.

System	SPARC 0.5 Bohr	PARSEC 0.5 Bohr	PARSEC 0.3 Bohr	OCTOPUS 0.5 Bohr	ABINIT
$Si_{29}H_{36}$	0.55 (128)	3.22 (8)	18.92 (16)	2.8 (256)	6.25 (106)
$Si_{71}H_{84}$	0.96 (320)	10.32 (64)	50.53 (64)	10.15 (512)	6.70 (321)
$Si_{275}H_{172}$	6.39 (704)	121.96 (512)	1046.00 (128)	92.78 (1024)	43.76 (666)
$Si_{525}H_{276}$	29.00 (960)	619.72 (512)	–	366.12 (1024)	203.30 (1008)

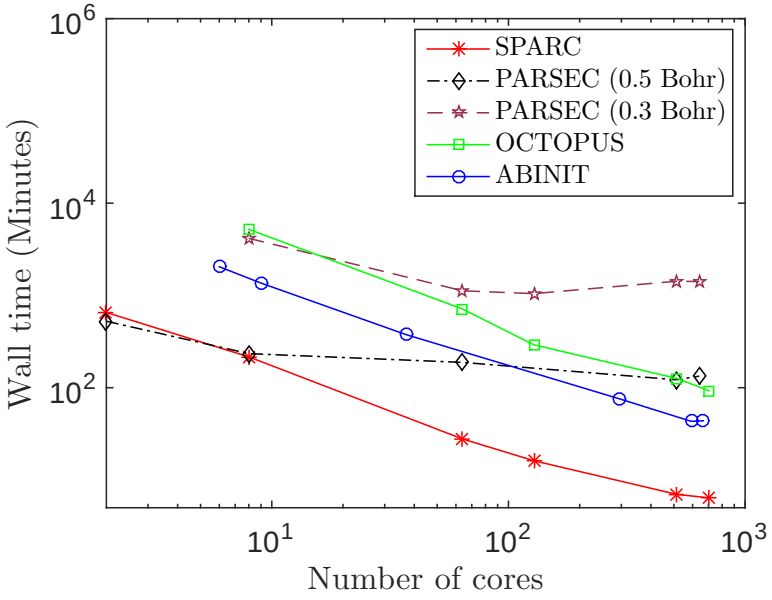

(a) Strong scaling

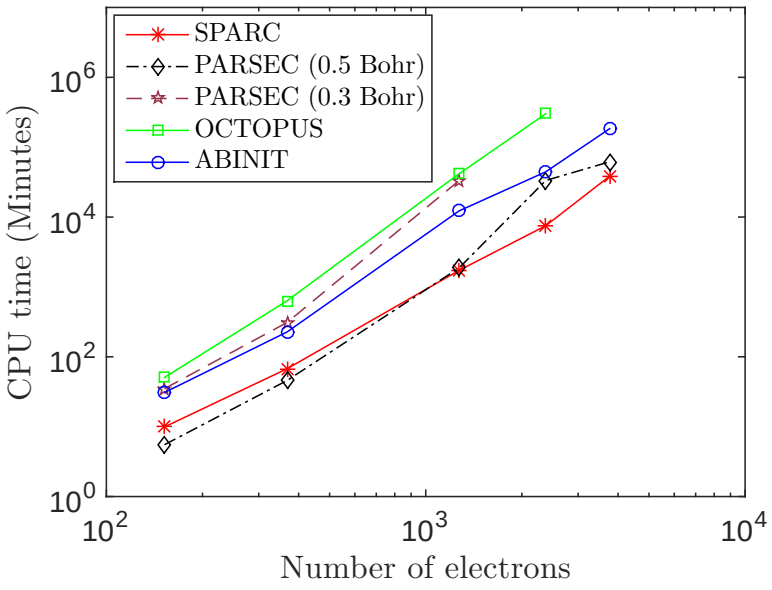

(b) Weak scaling

Figure 23: Comparison of strong and weak scaling behavior among different Density Functional Theory codes for hydrogen passivated silicon nanoclusters. The system utilized for strong scaling is $Si_{275}H_{172}$. The systems employed for weak scaling are $Si_{29}H_{36}$, $Si_{71}H_{84}$, $Si_{275}H_{172}$, $Si_{525}H_{276}$ and $Si_{849}H_{372}$.

REFERENCES

[1] AHLBERG, J. H., NILSON, E., and WALSH, J., *Mathematics in Science and Engineering*. New York: Academic Press, 1967.

[2] ANDERSON, D. G., "Iterative procedures for nonlinear integral equations," *Journal of the ACM (JACM)*, vol. 12, no. 4, pp. 547–560, 1965.

[3] ANDERSON, E., BAI, Z., BISCHOF, C., BLACKFORD, S., DEMMEL, J., DONGARRA, J., DU CROZ, J., GREENBAUM, A., HAMMARLING, S., MCKENNEY, A., and SORENSEN, D., *LAPACK Users' Guide*. Philadelphia, PA: Society for Industrial and Applied Mathematics, third ed., 1999.

[4] ARIAS, T. A., "Multiresolution analysis of electronic structure: semicardinal and wavelet bases," *Reviews of Modern Physics*, vol. 71, no. 1, p. 267, 1999.

[5] BALAY, S., BROWN, J., , BUSCHELMAN, K., EIJKHOUT, V., GROPP, W. D., KAUSHIK, D., KNEPLEY, M. G., MCINNES, L. C., SMITH, B. F., and ZHANG, H., "PETSc users manual," Tech. Rep. ANL-95/11 - Revision 3.4, Argonne National Laboratory, 2013.

[6] BALAY, S., GROPP, W. D., MCINNES, L. C., and SMITH, B. F., "Efficient management of parallelism in object oriented numerical software libraries," in *Modern Software Tools in Scientific Computing* (ARGE, E., BRUASET, A. M., and LANGTANGEN, H. P., eds.), pp. 163–202, Birkhäuser Press, 1997.

[7] BANERJEE, A. S., ELLIOTT, R. S., and JAMES, R. D., "A spectral scheme for Kohn–Sham density functional theory of clusters," *Journal of Computational Physics*, vol. 287, pp. 226–253, 2015.

[8] BANERJEE, A. S. and SURYANARAYANA, P., "Cyclic Density Functional Theory: A route to the first principles simulation of bending in nanostructures," *arXiv preprint arXiv:1605.08924*, 2016.

[9] BANERJEE, A. S., SURYANARAYANA, P., and PASK, J. E., "Periodic Pulay method for robust and efficient convergence acceleration of self-consistent field iterations," *Chemical Physics Letters*, vol. 647, pp. 31–35, 2016.

[10] BATCHO, P. F., "Spectrally accurate numerical solution of the single-particle schrödinger equation," *Phys. Rev. A*, vol. 57, pp. 4246–4252, Jun 1998.

[11] BECKE, A. D., "Density functional thermochemistry. II. The effect of the Perdew–Wang generalized–gradient correlation correction," *The Journal of Chemical Physics*, vol. 97, no. 12, 1992.

[12] BLOCH, F., "Über die quantenmechanik der elektronen in kristallgittern," *Zeitschrift für physik*, vol. 52, no. 7-8, pp. 555–600, 1929.

[13] BOBBITT, N. S., SCHOFIELD, G., LENA, C., and CHELIKOWSKY, J. R., "High order forces and nonlocal operators in a Kohn–Sham Hamiltonian," *Physical Chemistry Chemical Physics*, vol. 17, no. 47, pp. 31542–31549, 2015.

[14] BOTTIN, F., LEROUX, S., KNYAZEV, A., and ZÉRAH, G., "Large-scale ab initio calculations based on three levels of parallelization," *Computational Materials Science*, vol. 42, no. 2, pp. 329–336, 2008.

[15] BOWLER, D. R., CHOUDHURY, R., GILLAN, M. J., and MIYAZAKI, T., "Recent progress with large-scale ab initio calculations: the conquest code," *physica status solidi (b)*, vol. 243, no. 5, pp. 989–1000, 2006.

[16] BOWLER, D. R. and MIYAZAKI, T., "$\mathcal{O}(N)$ methods in electronic structure calculations," *Reports on Progress in Physics*, vol. 75, no. 3, p. 036503, 2012.

[17] BRÁZDOVÁ, V. and BOWLER, D. R., *Atomistic computer simulations: a practical guide*. John Wiley & Sons, 2013.

[18] BRIGGS, E. L., SULLIVAN, D. J., and BERNHOLC, J., "Real-space multigrid-based approach to large-scale electronic structure calculations," *Phys. Rev. B*, vol. 54, pp. 14362–14375, Nov 1996.

[19] BURDICK, W. R., SAAD, Y., KRONIK, L., VASILIEV, I., JAIN, M., and CHELIKOWSKY, J. R., "Parallel implementation of time-dependent density functional theory," *Computer Physics Communications*, vol. 156, no. 1, pp. 22–42, 2003.

[20] BYLASKA, E. J., HOLST, M., and WEARE, J. H., "Adaptive finite element method for solving the exact kohn–sham equation of density functional theory," *Journal of Chemical Theory and Computation*, vol. 5, no. 4, pp. 937–948, 2009.

[21] BYLASKA, E. J., TAYLOR, P. R., KAWAI, R., and WEARE, J. H., "LDA predictions of c20 isomerizations: neutral and charged species," *The Journal of Physical Chemistry*, vol. 100, no. 17, pp. 6966–6972, 1996.

[22] CARTER, E. A., "Challenges in modeling materials properties without experimental input," *Science*, vol. 321, no. 5890, pp. 800–803, 2008.

[23] CASTRO, A., APPEL, H., OLIVEIRA, M., ROZZI, C. A., ANDRADE, X., LORENZEN, F., MARQUES, M. A. L., GROSS, E. K. U., and RUBIO, A., "Octopus: a tool for the application of time-dependent density functional theory," *Physica Status Solidi B-Basic Solid State Physics*, vol. 243, no. 11, pp. 2465–2488, 2006.

[24] CEPERLEY, D. M. and ALDER, B. J., "Ground state of the electron gas by a stochastic method," *Physical Review Letters*, vol. 45, pp. 566–569, 1980.

[25] CHELIKOWSKY, J. R., TROULLIER, N., and SAAD, Y., "Finite-difference-pseudopotential method: electronic structure calculations without a basis," *Physical Review letters*, vol. 72, no. 8, p. 1240, 1994.

[26] CHO, K., ARIAS, T., JOANNOPOULOS, J., and LAM, P. K., "Wavelets in electronic structure calculations," *Physical Review Letters*, vol. 71, no. 12, p. 1808, 1993.

[27] COOLEY, J. and TUKEY, J., "An algorithm for the machine calculation of complex fourier series.," *Mathematics of Computation*, vol. 19, no. 90, p. 297, 1965.

[28] FANG, H.-R. and SAAD, Y., "Two classes of multisecant methods for nonlinear acceleration," *Numerical Linear Algebra with Applications*, vol. 16, no. 3, pp. 197–221, 2009.

[29] FANG, J., GAO, X., and ZHOU, A., "A Kohn–Sham equation solver based on hexahedral finite elements," *Journal of Computational Physics*, vol. 231, no. 8, pp. 3166 – 3180, 2012.

[30] FANN, G. I., HARRISON, R. J., BEYLKIN, G., JIA, J., HARTMAN-BAKER, R., SHELTON, W. A., and SUGIKI, S., "MADNESS applied to density functional theory in chemistry and nuclear physics," *Journal of Physics: Conference Series*, vol. 78, no. 1, p. 012018, 2007.

[31] FATTEBERT, J.-L., "Finite difference schemes and block Rayleigh Quotient Iteration for electronic structure calculations on composite grids," *Journal of Computational Physics*, vol. 149, no. 1, pp. 75 – 94, 1999.

[32] FINNIS, M., *Interatomic forces in condensed matter*. Oxford University Press, 2003.

[33] FOULKES, W. M. C. and HAYDOCK, R., "Tight-binding models and density-functional theory," *Physical Review B*, vol. 39, no. 17, p. 12520, 1989.

[34] FREYSOLDT, C., NEUGEBAUER, J., and VAN DE WALLE, C. G., "Fully ab initio finite-size corrections for charged-defect supercell calculations," *Physical Review Letters*, vol. 102, no. 1, p. 016402, 2009.

[35] GENOVESE, L., NEELOV, A., GOEDECKER, S., DEUTSCH, T., GHASEMI, S. A., WILLAND, A., CALISTE, D., ZILBERBERG, O., RAYSON, M., BERGMAN, A., and OTHERS, "Daubechies wavelets as a basis set for density functional pseudopotential calculations," *The Journal of chemical physics*, vol. 129, no. 1, p. 014109, 2008.

[36] GHOSH, S. and SURYANARAYANA, P., "Higher-order finite-difference formulation of periodic Orbital-free Density Functional Theory," *Journal of Computational Physics*, vol. 307, pp. 634–652, 2016.

[37] GHOSH, S. and SURYANARAYANA, P., "SPARC: Accurate and efficient finite-difference formulation and parallel implementation of Density Functional Theory. Part I: Isolated clusters," *arXiv preprint arXiv:1603.04334*, 2016.

[38] GHOSH, S. and SURYANARAYANA, P., "SPARC: Accurate and efficient finite-difference formulation and parallel implementation of Density Functional Theory. Part II: Periodic systems," *arXiv preprint arXiv:1603.04339*, 2016.

[39] GIANNOZZI, P., BARONI, S., BONINI, N., CALANDRA, M., CAR, R., CAVAZZONI, C., CERESOLI, D., CHIAROTTI, G. L., COCOCCIONI, M., DABO, I., DAL CORSO, A., DE GIRONCOLI, S., FABRIS, S., FRATESI, G., GEBAUER, R., GERSTMANN, U., GOUGOUSSIS, C., KOKALJ, A., LAZZERI, M., MARTIN-SAMOS, L., MARZARI, N., MAURI, F., MAZZARELLO, R., PAOLINI, S., PASQUARELLO, A., PAULATTO, L., SBRACCIA, C., SCANDOLO, S., SCLAUZERO, G., SEITSONEN, A. P., SMOGUNOV, A., UMARI, P., and WENTZCOVITCH, R. M., "QUANTUM ESPRESSO: a modular and open-source software project for quantum simulations of materials," *Journal of Physics: Condensed Matter*, vol. 21, no. 39, p. 395502 (19pp), 2009.

[40] GILLAN, M., "Calculation of the vacancy formation energy in aluminium," *Journal of Physics: Condensed Matter*, vol. 1, no. 4, p. 689, 1989.

[41] GOEDECKER, S., "Linear scaling electronic structure methods," *Rev. Mod. Phys.*, vol. 71, pp. 1085–1123, Jul 1999.

[42] GOLUB, G. H. and VAN LOAN, C. F., *Matrix computations*, vol. 3. JHU Press, 2012.

[43] GONZE, X., BEUKEN, J. M., CARACAS, R., DETRAUX, F., FUCHS, M., RIGNANESE, G. M., SINDIC, L., VERSTRAETE, M., ZERAH, G., JOLLET, F., TORRENT, M., ROY, A., MIKAMI, M., GHOSEZ, P., RATY, J. Y., and ALLAN, D. C., "First-principles computation of material properties: the abinit software project," *Computational Materials Science*, vol. 25, pp. 478–492(15), 2002.

[44] GONZE, X., "A brief introduction to the ABINIT software package," *Zeitschrift für Kristallographie*, vol. 220, no. 5/6/2005, pp. 558–562, 2005.

[45] GONZE, X., AMADON, B., ANGLADE, P.-M., BEUKEN, J.-M., BOTTIN, F., BOULANGER, P., BRUNEVAL, F., CALISTE, D., CARACAS, R., COTE, M., and OTHERS, "ABINIT: First-principles approach to material and nanosystem properties," *Computer Physics Communications*, vol. 180, no. 12, pp. 2582–2615, 2009.

[46] GYGI, F., "Architecture of Qbox: A scalable first-principles molecular dynamics code," *IBM Journal of Research and Development*, vol. 52, no. 1.2, pp. 137–144, 2008.

[47] HACKBUSCH, W., *Multi-grid methods and applications*, vol. 4. Springer Science & Business Media, 2013.

[48] HARRIS, J., "Simplified method for calculating the energy of weakly interacting fragments," *Physical Review B*, vol. 31, no. 4, p. 1770, 1985.

[49] HESTENES, M. R. and STIEFEL, E., "Methods of conjugate gradients for solving linear systems," *Journal of Research of the National Bureau of Standards*, vol. 49, no. 6, pp. 409–436, 1952.

[50] HIROSE, K., ONO, T., FUJIMOTO, Y., and TSUKAMOTO, S., "First-principles clacculations in real-space formalism," 2005.

[51] HOCKNEY, R. W. and EASTWOOD, J. W., *Computer Simulation Using Particles*. 1981.

[52] HOHENBERG, P. and KOHN, W., "Inhomogeneous electron gas," *Physical Review*, vol. 136, no. 3B, pp. B864–B871, 1964.

[53] HUBER, K.-P., *Molecular spectra and molecular structure: IV. Constants of diatomic molecules*. Springer Science & Business Media, 2013.

[54] HUTTER, J., LÜTHI, H. P., and PARRINELLO, M., "Electronic structure optimization in plane-wave-based density functional calculations by direct inversion in the iterative subspace," *Computational Materials Science*, vol. 2, no. 2, pp. 244–248, 1994.

[55] ISMAIL-BEIGI, S. and ARIAS, T. A., "New algebraic formulation of density functional calculation," *Computer Physics Communications*, vol. 128, no. 1-2, pp. 1 – 45, 2000.

[56] JONES, R. O., "Density functional theory: Its origins, rise to prominence, and future," *Rev. Mod. Phys.*, vol. 87, pp. 897–923, Aug 2015.

[57] JONES, R. O. and GUNNARSSON, O., "The density functional formalism, its applications and prospects," *Rev. Mod. Phys.*, vol. 61, pp. 689–746, Jul 1989.

[58] KADUK, B., KOWALCZYK, T., and VAN VOORHIS, T., "Constrained density functional theory," *Chemical Reviews*, vol. 112, no. 1, pp. 321–370, 2011.

[59] KLEINMAN, L. and BYLANDER, D., "Efficacious form for model pseudopotentials," *Physical Review Letters*, vol. 48, no. 20, p. 1425, 1982.

[60] KNYAZEV, A. V., "Toward the optimal preconditioned eigensolver: Locally optimal block preconditioned conjugate gradient method," *SIAM journal on scientific computing*, vol. 23, no. 2, pp. 517–541, 2001.

[61] KOHN, W., "Density functional and density matrix method scaling linearly with the number of atoms," *Phys. Rev. Lett.*, vol. 76, pp. 3168–3171, Apr 1996.

[62] KOHN, W. and SHAM, L. J., "Self-consistent equations including exchange and correlation effects," *Physical Review*, vol. 140, no. 4A, pp. A1133–A1138, 1965.

[63] KOHN, W., BECKE, A. D., and PARR, R. G., "Density functional theory of electronic structure," *The Journal of Physical Chemistry*, vol. 100, no. 31, pp. 12974–12980, 1996.

[64] KRESSE, G. and FURTHMÜLLER, J., "Efficient iterative schemes for ab initio total-energy calculations using a plane-wave basis set," *Physical Review B*, vol. 54, no. 16, pp. 11169–11186, 1996.

[65] KRESSE, G. and HAFNER, J., "Ab initio molecular dynamics for liquid metals," *Physical Review B*, vol. 47, no. 1, p. 558, 1993.

[66] LANCZOS, C., *An iteration method for the solution of the eigenvalue problem of linear differential and integral operators*. United States Government Press Office, 1950.

[67] LESZCZYNSKI, J., *Handbook of computational chemistry*, vol. 2. Springer Science & Business Media, 2012.

[68] LEVITT, A. and TORRENT, M., "Parallel eigensolvers in plane-wave density functional theory," *Computer Physics Communications*, vol. 187, pp. 98 – 105, 2015.

[69] LIN, L. and YANG, C., "Elliptic preconditioner for accelerating the self-consistent field iteration in kohn–sham density functional theory," *SIAM Journal on Scientific Computing*, vol. 35, no. 5, pp. S277–S298, 2013.

[70] MARTIN, R., *Electronic Structure: Basic theory and practical methods*. Cambridge University Press, 2004.

[71] MARX, D. and HUTTER, J., "Ab initio molecular dynamics: Theory and implementation," *Modern methods and algorithms of quantum chemistry*, vol. 1, pp. 301–449, 2000.

[72] MARX, D. and HUTTER, J., *Ab initio molecular dynamics: basic theory and advanced methods*. Cambridge University Press, 2009.

[73] MASUD, A. and KANNAN, R., "B-splines and nurbs based finite element methods for kohn–sham equations," *Computer Methods in Applied Mechanics and Engineering*, vol. 241, pp. 112–127, 2012.

[74] MAZZIOTTI, D. A., "Spectral difference methods for solving differential equations," *Chemical physics letters*, vol. 299, no. 5, pp. 473–480, 1999.

[75] MERMIN, N. D., "Thermal properties of the inhomogeneous electron gas," *Phys. Rev.*, vol. 137, pp. A1441–A1443, Mar 1965.

[76] MOHAN, J., *Organic spectroscopy: principles and aapplications*. CRC Press, 2004.

[77] MONKHORST, H. J. and PACK, J. D., "Special points for Brillouin-zone integrations," *Physical Review B*, vol. 13, no. 12, p. 5188, 1976.

[78] MOTAMARRI, P., IYER, M., KNAP, J., and GAVINI, V., "Higher-order adaptive finite-element methods for orbital-free density functional theory," *Journal of Computational Physics*, vol. 231, no. 20, pp. 6596–6621, 2012.

[79] ONO, T. and HIROSE, K., "Timesaving double-grid method for real-space electronic-structure calculations," *Phys. Rev. Lett.*, vol. 82, no. 25, pp. 5016–5019, 1999.

[80] PAIGE, C. C. and SAUNDERS, M. A., "Solution of sparse indefinite systems of linear equations," *SIAM journal on numerical analysis*, vol. 12, no. 4, pp. 617–629, 1975.

[81] PARR, R. G. and YANG, W., "Density-functional theory of the electronic structure of molecules," *Annual Review of Physical Chemistry*, vol. 46, no. 1, pp. 701–728, 1995.

[82] PASK, J. E., KLEIN, B. M., FONG, C. Y., and STERNE, P. A., "Real-space local polynomial basis for solid-state electronic-structure calculations: A finite-element approach," *Physical Review B*, vol. 59, no. 19, pp. 12352–12358, 1999.

[83] PASK, J. E. and STERNE, P. A., "Real-space formulation of the electrostatic potential and total energy of solids," *Phys. Rev. B*, vol. 71, p. 113101, Mar 2005.

[84] PASK, J. E., SUKUMAR, N., and MOUSAVI, S. E., "Linear scaling solution of the all-electron coulomb problem in solids," *International Journal for Multiscale Computational Engineering*, vol. 10, no. 1, pp. 83–99, 2012.

[85] PAYNE, M. C., TETER, M. P., ALLAN, D. C., ARIAS, T., and JOANNOPOULOS, J., "Iterative minimization techniques for ab initio total-energy calculations: molecular dynamics and conjugate gradients," *Reviews of Modern Physics*, vol. 64, no. 4, pp. 1045–1097, 1992.

[86] PERDEW, J. P. and WANG, Y., "Accurate and simple analytic representation of the electron-gas correlation energy," *Physical Review B*, vol. 45, no. 23, pp. 13244–13249, 1992.

[87] PERDEW, J. P. and YUE, W., "Accurate and simple density functional for the electronic exchange energy: Generalized gradient approximation," *Physical Review B*, vol. 33, no. 12, p. 8800, 1986.

[88] PHILLIPS, R., *Crystals, Defects and Microstructures: Modeling Across Scales*. Cambridge University Press, 1 ed., Mar. 2001.

[89] PRATAPA, P. P. and SURYANARAYANA, P., "Restarted Pulay mixing for efficient and robust acceleration of fixed-point iterations," *Chemical Physics Letters*, vol. 635, pp. 69–74, 2015.

[90] PRATAPA, P. P., SURYANARAYANA, P., and PASK, J. E., "Spectral Quadrature method for accurate $\mathcal{O}(N)$ electronic structure calculations of metals and insulators," *Computer Physics Communications*, 2015.

[91] PRESS, W. H., *Numerical recipes 3rd edition: The art of scientific computing*. Cambridge university press, 2007.

[92] PROBERT, M. and PAYNE, M., "Improving the convergence of defect calculations in supercells: An ab initio study of the neutral silicon vacancy," *Physical Review B*, vol. 67, no. 7, p. 075204, 2003.

[93] SEGALL, M. D., LINDAN, P. J. D., PROBERT, M. J., PICKARD, C. J., HASNIP, P. J., CLARK, S. J., and PAYNE, M. C., "First-principles simulation: ideas, illustrations and the CASTEP code," *Journal of Physics: Condensed Matter*, vol. 14, no. 11, pp. 2717–2744, 2002.

[94] SHEWCHUK, J. R., "An introduction to the conjugate gradient method without the agonizing pain," 1994.

[95] SHIMOJO, F., KALIA, R. K., NAKANO, A., and VASHISHTA, P., "Linear-scaling density-functional-theory calculations of electronic structure based on real-space grids: design, analysis, and scalability test of parallel algorithms," *Computer Physics Communications*, vol. 140, no. 3, pp. 303 – 314, 2001.

[96] SKYLARIS, C.-K., HAYNES, P. D., MOSTOFI, A. A., and PAYNE, M. C., "Introducing ONETEP: Linear-scaling density functional simulations on parallel computers," *The Journal of Chemical Physics*, vol. 122, no. 8, p. 084119, 2005.

[97] SLATER, J. C., *The self-consistent field for molecules and solids*, vol. 4. McGraw-Hill New York, 1974.

[98] SURYANARAYANA, P., BHATTACHARYA, K., and ORTIZ, M., "A mesh-free convex approximation scheme for Kohn-Sham density functional theory," *Journal of Computational Physics*, vol. 230, no. 13, pp. 5226 – 5238, 2011.

[99] SURYANARAYANA, P., BHATTACHARYA, K., and ORTIZ, M., "Coarse-graining Kohn-Sham Density Functional Theory," *Journal of the Mechanics and Physics of Solids*, vol. 61, no. 1, pp. 38 – 60, 2013.

[100] SURYANARAYANA, P., GAVINI, V., BLESGEN, T., BHATTACHARYA, K., and ORTIZ, M., "Non-periodic finite-element formulation of Kohn-Sham density functional theory," *Journal of the Mechanics and Physics of Solids*, vol. 58, no. 2, pp. 256 – 280, 2010.

[101] SURYANARAYANA, P. and PHANISH, D., "Augmented Lagrangian formulation of Orbital-Free Density Functional Theory," *Journal of Computational Physics*, vol. 275, no. 15, pp. 524–538, 2014.

[102] SZABO, A. and OSTLUND, N. S., *Modern Quantum Chemistry: Introduction to Advanced Electronic Structure Theory (Dover Books on Chemistry)*. Dover Publications, new edition ed., July 1996.

[103] TROULLIER, N. and MARTINS, J. L., "Efficient pseudopotentials for plane-wave calculations," *Physical Review B*, vol. 43, no. 3, pp. 1993–2006, 1991.

[104] TSUCHIDA, E. and TSUKADA, M., "Electronic-structure calculations based on the finite-element method," *Physical Review B*, vol. 52, no. 8, p. 5573, 1995.

[105] TUCKERMAN, M. E., YARNE, D., SAMUELSON, S. O., HUGHES, A. L., and MARTYNA, G. J., "Exploiting multiple levels of parallelism in molecular dynamics based calculations via modern techniques and software paradigms on distributed memory computers," *Computer Physics Communications*, vol. 128, no. 1âĂŞ2, pp. 333 – 376, 2000.

[106] WATKINS, D. S., *Fundamentals of matrix computations*, vol. 64. John Wiley & Sons, 2004.

[107] WHITE, S. R., WILKINS, J. W., and TETER, M. P., "Finite-element method for electronic structure," *Physical Review B*, vol. 39, no. 9, p. 5819, 1989.

[108] YANG, W., "Direct calculation of electron density in density-functional theory," *Physical Review letters*, vol. 66, no. 11, p. 1438, 1991.

[109] ZHOU, Y., SAAD, Y., TIAGO, M. L., and CHELIKOWSKY, J. R., "Parallel self-consistent-field calculations via Chebyshev-filtered subspace acceleration," *Physical Review E*, vol. 74, no. 6, p. 066704, 2006.

[110] ZHOU, Y., SAAD, Y., TIAGO, M. L., and CHELIKOWSKY, J. R., "Self-consistent-field calculations using Chebyshev-filtered subspace iteration," *Journal of Computational Physics*, vol. 219, no. 1, pp. 172–184, 2006.

[111] ZHOU, Y., CHELIKOWSKY, J. R., and SAAD, Y., "Chebyshev-filtered subspace iteration method free of sparse diagonalization for solving the Kohn–Sham equation," *Journal of Computational Physics*, vol. 274, pp. 770–782, 2014.

[112] ZIEGLER, T., "Approximate density functional theory as a practical tool in molecular energetics and dynamics," *Chemical Reviews*, vol. 91, no. 5, pp. 651–667, 1991.